Comparative study of different Density Functional Theory methodologies for calculating magnetic and electronic properties of small Mn clusters.

A thesis presented by :

Paulino Ajiquichí Pecher

To obtain the Master's degree in Interdisciplinary Sciences

Line of research:

Materials Physics

Thesis Advisor:

Ph.D. Pedro Ruiz Díaz

San Luis Potosí, August 2024

Abstract

The present manuscript focus on a first-principles study regarding the electronic and magnetic properties of small manganese clusters (Mn_α, $\alpha = 2, \cdots, 7$) based on Density Functional Theory (DFT) using different methodologies. The study primarily aims to determine the magnetic ordering and the optimized ground-state structures. The calculations are performed employing two different basis sets: plane waves and localized molecular orbitals implemented in two electronic structure calculation codes, which are widely known for atomic-scale materials modeling. The advantages and disadvantages of each approach are discussed. Our work also aims on quantifying the impact of the exchange and electronic correlation (XC) effects on the magneto-electronic properties of the Mn clusters. In particular, this study focus on employing hybrid functionals which take a portion of the exact Hartree-Fock (HF) exchange to describe the non-local XC interactions contributing to the electronic energy. These functionals are advised to be used when self-interaction error potentially may be meaningful as in the case of the Mn clusters. The Mn dimer is studied with special care. Local, semi-local, and non-local functionals are used to treat the XC effects. Our calculations show that only hybrid functionals and beyond can accurately describe the magnetic ordering and equilibrium bond distance assessed experimentally. Thus, for cluster containing from 3 up to 7 atoms are studied solely with hybrid functionals. Our calculations respect to the ground-state structure shows a clear improvement over previous theoretical studies. We determine the low-lying isomers for all the considered clusters, finding a clear tendency towards antiferromagnetism, adopting low-spin magnetic configurations which are closely with the experimental measurements. To hunt the configurations having small magnetic moment non-collinear spin textures are also considered for Mn_5 clusters. Our findings indicate that non-collinear arrangements do not stabilized over the collinear antiferromagnetic configurations. Geometrical effects are explored by considering two different structures for Mn_6 and Mn_7. We found that compact structures are preferred. Our calculations show that for Mn_6 the bicapped tetrahedron is the ground-state structure while the square bipyramid is reported as the most stable structure when using semi-local XC functionals. The electronic properties of the Mn clusters are further analyzed through the density of states (DOS). We see the hybrid XC functionals favoring localized states and lower hybridization, especially the $s - d$ type. The $4s$ bonding is promoted in all the considered clusters encouraging large bond distances and stabilizing antiferromagnetism. In summary, our study shows that the usage of hybrid functionals with a substancial portion of the exact HF exchange improve the direct interactions among manganese atoms, providing a better description of the magnetic and electronic properties of Mn clusters. We also conclude that the considered implementations to the DFT (plane waves and molecular localized basis sets) yield to the same qualitative results which are consistent with the basis of the quantum mechanics and DFT theory.

Resumen

El presente manuscrito se centra en un estudio de primeros principios sobre las propiedades electrónicas y magnéticas de pequeños cúmulos de manganeso (Mn_α, $\alpha = 2, \cdots, 7$) basado en la teoría del funcional de la densidad (DFT) utilizando diferentes metodologías. El estudio tiene como objetivo principal determinar el ordenamiento magnético y las estructuras optimizadas del estado fundamental. Los cálculos se realizan empleando dos conjuntos de bases diferentes: ondas planas y orbitales moleculares localizados implementados en dos códigos de cálculo de estructura electrónica, que son ampliamente conocidos para el modelado de materiales a escala atómica. Se discuten las ventajas y desventajas de cada enfoque. Nuestro trabajo también tiene como objetivo cuantificar el impacto de los efectos de intercambio y correlación electrónica (XC) en las propiedades magneto-electrónicas de los cúmulos de Mn. En particular, este estudio se centra en el empleo de funcionales híbridas que toman una parte del intercambio exacto de Hartree-Fock (HF) para describir las interacciones XC no locales que contribuyen a la energía electrónica. Se recomienda utilizar estos funcionales cuando el error de autointeracción puede ser potencialmente significativo, como en el caso de los cúmulos de Mn. El dímero de Mn se estudia con especial cuidado. Se utilizan funcionales locales, semilocales y no locales para tratar los efectos XC. Nuestros cálculos muestran que solo los funcionales híbridos y más allá pueden describir con precisión el ordenamiento magnético y la distancia de enlace de equilibrio evaluados experimentalmente. Por lo tanto, para los cúmulos que contienen de 3 a 7 átomos se estudian únicamente con funcionales híbridas. Nuestros cálculos con respecto a la estructura del estado fundamental muestran una clara mejora con respecto a estudios teóricos previos. Determinamos los isómeros de baja altitud para todos los cúmulos considerados, encontrando una clara tendencia hacia el antiferromagnetismo, adoptando configuraciones magnéticas de bajo espín que se acercan estrechamente a las mediciones experimentales. Para buscar las configuraciones que tienen un momento magnético pequeño, también se consideran texturas de espín no colineales para los cúmulos de Mn_5. Nuestros hallazgos indican que los arreglos no colineales no se estabilizan sobre las configuraciones antiferromagnéticas colineales. Se exploran los efectos geométricos considerando dos estructuras diferentes para Mn_6 y Mn_7. Descubrimos que se prefieren las estructuras compactas. Nuestros cálculos muestran que para Mn_6 el tetraedro bicapeado es la estructura del estado fundamental, mientras que la bipirámide cuadrada se reporta como la estructura más estable cuando se utilizan funcionales XC semilocales. Las propiedades electrónicas de los cúmulos de Mn se analizan más a fondo a través de la densidad de estados (DOS). Vemos que las funcionales XC híbridas favorecen los estados localizados y una menor hibridación, especialmente el tipo $s - d$. El enlace $4s$ se promueve en todos los cúmulos considerados, lo que fomenta grandes distancias de enlace y estabiliza el antiferromagnetismo. En resumen, nuestro estudio muestra que el uso de funcionales híbridas con una porción sustancial del intercambio exacto de HF mejora las interacciones directas entre los átomos de manganeso, lo que proporciona una mejor descripción de las propiedades magnéticas y electrónicas de los cúmulos de Mn. También concluimos que las implementaciones consideradas para la DFT (ondas planas y conjuntos de bases localizadas moleculares) producen los mismos resultados cualitativos que son consistentes con la base de la mecánica cuántica y la teoría DFT.

Acknowledgments

In this page I want to express my deep gratitude to all people who have supported me during my career.

Foremost, I want to thank my advisor, Ph.D. Pedro Ruiz Díaz, for his patience and sharing with me his knowledge and time to attend to my doubts. I really appreciate the opportunity that I had to work with him these months. Thanks a lot.

Thanks a lot, to staff members at Physics Institute of UASLP, faculty members and graduate students. Special thanks to Ph.D. Jesús Dorantes Dávila for letting me know about the Master's Program in Mexico and for the classes I received with him. The same way, special thanks to Maricela Cano for her help with the paperwork and attention to solving bureaucratic problems.

I thank the Mexican people and government for the financial support received to complete my master's degree. It is an honor to have received support with CVU number: 1243680, through The Consejo Nacional de Humanidades, Ciencias y Tecnologías (CONAHCYT). I would also like to thank the team at The Laboratorio Nacional de Supercómputo (LNS) del Sureste de México for using The *Cuetlaxcoapan* Supercomputer with user 202101016n.

Immense thanks to my mentor Ph.D. Robert F. Cahalan for his advice and help in revising my writing. Without a doubt, he has always been a support in my scientific career.

Finally, my infinite gratitude to my parents for their endorsement and unconditional love. In the same thanks to my two brothers for their valuable support.

Contents

List of Figures

List of Tables

Objectives

a) General Objective

In this thesis work a systematic study of the calculation of electronic and magnetic properties in manganese (Mn) clusters is carried out. For the research, we use different implementation based on Density Functional Theory (DFT). In addition, comparisons are made with other studies based on DFT or improvements to the same theory. Emphasis is also placed on the advantages and disadvantages of each code given the system being studied as well as highlighting the differences and the impact of the functional ones for the description of the Mn clusters. The scientific codes we use are:

1. **Vienna *ab initio* Simulation Package (VASP):** is a code to perform *ab initio* quantum chemistry calculations employing pseudopotentials, projector-augmented wave method, supercell approximation, and plane waves basis set [7]. The code basically works with DFT, but due to the need to perform more complex calculations to understand better way the system it includes post-DFT corrections. Among this corrections are hybrid functionals which are a mix of standard DFT and Hartree-Fock exchange energy (e.g., PBE0[8] and B3LYP[9]).

2. **ORCA:** is a quantum chemistry program and for theoretical research in materials science and biochemistry which deals with all modern electronic structure methods (DFT, many-body perturbation and coupled cluster theories). Its main field of application is larger molecules, open-shell transition metals (e.g. Mn), spectroscopy, and magnetism [10] [11]. ORCA uses localized molecular orbitals (e.g. Gaussian basis, triple$-\zeta$) basis set and features all-electron and effective core potential (ECP) based basis sets [11].

b) Specific Objectives

1. Learn the fundamentals of DFT and its implementation with different methodologies.
2. Learn how to use supercomputing equipment to calculate the electronic structure and magnetic properties of atomic systems.
3. Calculating the magneto-electronic properties of small Mn clusters.
4. Studying the impact of exchange-correlation functionals on structural, electronic and magnetic properties.
5. Quantitatively compare two implementations of DFT.

Background

Materials science is a cross-disciplinary field that focuses on the development, characterization, and application of materials for specific purposes [12]. The materials considered in this field of physics encompass a wide range from metals, ceramics, polymers, composite materials and nanomaterials to biomaterials and semiconductors [13]. The main objective of materials science is to study the properties, structure, synthesis methods and potential uses of these materials in several industries such as electronics, energy and biomedicine [14].

From a theoretical viewpoint, materials modeling also allows us to understand and forecast the properties of materials. By providing insights about the properties and behavior of materials, modeling enables us to develop new materials with specific features, optimize existing materials for specific applications, and understand the fundamental principles that rule the behavior of these materials (materials engineering).

Materials modeling begins with the creation of mathematical or computational models that describe the behavior of materials under various conditions. It involves understanding and predicting the physical, chemical and mechanical properties of materials based on their atomic or molecular structure, as well as their interactions at different length scales. In general, different approaches are used in materials modeling, depending on the level of complexity and scale of study. These approaches include:

I) **Multiscale modeling:** many materials exhibit complex behavior spanning multiple length and time scales. Multiscale modeling involves the employment of models from the atomic to the continuum level, to understand the hierarchical nature of material properties.

II) **Atomistic modeling:** materials are modeled at the atomic or molecular scale, taking into account interactions between individual atoms or molecules. To simulate the behavior of materials at this level, classical mechanics is mainly used.

III) **Continuous modeling:** this approach presents materials as continuous media and describes their behavior using partial differential equations and classical physics equations. Continuous models are suitable for macroscopic simulations and can encompass the global behavior of materials under different conditions.

IV) **Quantum-mechanical modeling:** in this approach, atoms and molecules are studied and their interactions from a quantum mechanics point of view. For this thesis work, we use this approach to study small Mn clusters.

Generally when we deal with a great number of particles, atoms, molecules, etc, computational algorithms are used to study their properties. Nowadays with the enormous capacity of computers DFT has emerged as a very good approximation for solving the many-body problem.

DFT is a quantum mechanical modeling approach used widely in materials science, condensed matter physics, and chemistry to study the electronic structure of atoms, molecules, and solids. It provides a theoretical framework for understanding and predicting the behavior of electrons in a material. DFT is the theory to be employed in this work for computational modeling of Manganese (Mn) clusters.

Experimental studies about manganese clusters

In natural sciences experimental studies are crucial to validate (or invalidate) theoretical ideas. Although the present work is only focused on the computational study of manganese clusters, it is important to take account of the recent experimental measurements for comparison.

The group of two manganese atoms (Mn_2 is the simpest case to study. Mn_2 has been studied with rare-gas matrices experiment in combined with electron spin resonance (ESR) technique. Experiments has shown that the Mn_2 bond length is 3.4 Å [15] [16] [17]. The atomic spins couple antiferromagnetically, which means that the ground magnetic moment is 0 μ_B [15] [18]. These previous results for the bond length and for the ground magnetic state were confirmed by Cheeseman *et al.* [16]. Regarding the dissociation energy has been determined that is 0.13 $eV \pm 0.10$ eV [17] [19].

For clusters Mn_3 there is no available data about magnetic ordering (ferromagnetic or antiferromagnetic) or about the ground state. Thus comparison of our results for Mn_3 can presently only be with other computational results. For Mn_4 previous theoretical studies indicate that it has ferromagnetic ordering and its ground magnetic moment is 5 μ_B per atom [20] [21]. Unfortunately there are no experimental studies to confirm the theoretical result.

In 2004 Mark B. Knickelbein [22] published his experimental results of molecular beam deflection measurements for Mn_5 - Mn_{22}. The results obtained by Knickelbein for the magnetic moment per atom for Mn_5, Mn_6 and Mn_7 appear in Table 1 combined with magnetic moments of Mn_2 and Mn_4. It is important to highlight that for Mn_5, a previous Electron Spin Resonance (ESR) experiment gives a FM solution for the ground state with net magnetic moment 5 μ_B per atom [15]. As we note, there is disagreement between the results reported by Knickelbein [22] and Baumann *et al.* [15]. So, it is not unlikely that future experiments may provide different results (or maybe not) than we use in this work to compare with our computational results.

α	**Magnetic moment** (μ_B)	**Error** (μ_B)
2	0	–
3	–	–
4	–	–
5	0.79	$\pm$ 0.25
6	0.55	$\pm$ 0.10
7	0.72	$\pm$ 0.42

Table 1: Experimental results for ground magnetic moment per atom for Mn_α

As we can see, the ground magnetic moment per atom of Mn clusters, in general are less than two, except for $\alpha = 4$. For instance, for Mn_5 the total magnetic moment is $5 * 0.79$ $\mu_B = 3.95$ μ_B and with a minimum magnetic moment of 5*(0.79 μ_B − 0.25 μ_B) = 2.7 μ_B and a maximum 5*(0.79 μ_B + 0.25 μ_B) = 5.2 μ_B. About each one of the clusters, there are theoretical and computational studies (geometry of cluster, bond length, bonding energy, magnetic moment, etc.) that we will mention as we proceed, and compare these with our results.

Chapter 1

Introduction

Magnetization is a phenomenon well known by human beings for thousands of years. At the beginning it was associated with magic or something similar. However, eventually new ideas arose to explain the origin of this effect presented by some materials, and also to find applications. For example, explorers took advantage of lodestones' magnetization to construct compasses which use Earth's magnetic field. Thus we can say that the compass helped to scout and navigate the Earth [23].

The modern concept of the origin of magnetization is the alignment of spins, which are intrinsic angular moment of elementary particles like electrons [24]. Also, taking advantage of the quantum theory associated with magnetization, today devices have been developed that can store a large quantity of information by magnetic recording. This has led to an industry focused on applying the ideas of magnetization to develop cutting-edge technologies [23].

To continue improving the performance of different types of devices, it is necessary to study properties of materials. For instance, for audio recording the magnetic material used is Ferric Oxide (hematite or maghemite) (Fe_2O_3), for video recording Chromium dioxide (CrO_2) is often used, and also for higher grades of audio recording [23]. Transition metals like chromium (Cr) and manganese (Mn) with their half-filled shells are interesting to develop devices to store data [25]. In case for Mn with an electronic configuration [Ar]$4s^2 3d^5$ depicts the maximum magnetic moment (5 μ_B) per atom when the spin of electrons in the d-orbital have the same orientation in accordance with Hund's Law. Thus, Mn offers good properties for storage information owing to strong magnetism and low dimension.

In this work the computational study of manganese clusters is the main focus, together with density functional theory (DFT). The DFT was born roughly in 1964 when Hohenberg and Kohn published a paper where they introduced theorems which today represent the major theoretical pillars of the DFT [26]. The theorems are a mathematical formalism for solving the many-body problem, where the set of differential equations are not linear. At the end of the 20th century, with the help of computers and supercomputers, it became possible to begin to test and apply the theory to study materials at atomic scale.

In the first part of this work, in Table 1 in the background section above, we provide experimental measurements as a result of collecting information from experiments that have been developed for Mn clusters. The dimer (Mn_2) is the one that is best studied due to its simplicity. It offers a great chance to assess the performance of functionals. Regarding the other clusters, our results will show essential information about them too.

The document is structured as follow: Chapter II provides theoretical details about the many-body problem, the Born-Oppenheimer approximation, Hartree-Fock approximation, Hohenberg and Kohn theorems, exchange-correlation functionals and other generalities of DFT. Chapter III contains information about VASP and ORCA codes, which are the codes that we use to compute the properties of Mn clusters (Mn_α, $\alpha = 2, \cdots, 7$). Chapter IV presents results in detail about each cluster, comparison between the results, comparison with other computational studies, and with experimental measurements. Analyzes are also carried out on bonding energies, most stable structures, bond lengths, density of states, local magnetic moments and other relevant details. Finally, Chapter V summarizes the results and conclusions, and suggests future lines of research.

Chapter 2

Theoretical Framework

2.1 Time-independent Schrödinger's equation for many-body problems

Quantum mechanics emerged as a revolutionary idea at the beginning of 20th century, to explain the Planck radiation distribution, the photoelectric effect, and properties of atoms which were considered to be fundamental "building blocks" of matter. As scientists began to understand the atom, its own "building blocks" were understood to be three particles, namely the electron, proton and neutron. The explanation of the proton and neutron, particles that are part of the nuclei of atoms, were eventually understood in terms of more "elementary" ones named "quarks" that were conjectured later to explain the proliferation of many more particles that were observed as increasingly powerful accelerators came online. Today, the most advanced quantum theory is a quantum field theory called "The Standard Model". It employs the symmetries SU(3), SU(2), and U(1). With these it is able to unify the strong, the weak, and the electromagnetic interactions of all the known elementary particles. That model has been applied in many situations to explain the properties and behavior of matter at smallest observed scales.

Just like Newton's Laws which are fundamental in classical physics to understand phenomena in the macroscopic world, quantum mechanical equations focus on the microscopic world. For example, the non-relativistic Schrödinger' equation is a key to understanding atoms, molecules, particles, clusters, etc. [27].

In quantum physics one of the most important problems is to compute the ground state of a system of many particles. This can be achieved by solving Equation 2.1,

$$H\Psi_k = E\Psi_k \tag{2.1}$$

Where H is the Hamiltonian of the system and Ψ_k is the wave function of each particle, labelled by k. If the system contains N electrons of mass m_e and L nuclei of mass M_A, the Hamiltonian is given as:

$$H = -\sum_{i=1}^{N} \frac{\hbar^2}{2m_e}\nabla_i^2 - \sum_{A=1}^{L} \frac{\hbar^2}{2M_A}\nabla_A^2 + \sum_{i\neq j}^{N} \frac{e^2}{4\pi\epsilon_0}\frac{1}{|\vec{r}_i - \vec{r}_j|} + \frac{1}{2}\sum_{A\neq B}^{L} \frac{e^2}{4\pi\epsilon_0}\frac{Z_A Z_B}{|\vec{R}_A - \vec{R}_B|} - \sum_{i,A} \frac{e^2}{4\pi\epsilon_0}\frac{Z_A}{|\vec{r}_i - \vec{R}_A|} \tag{2.2}$$

The terms that appear in Equation 2.2 represents the electron's kinetic energy, the kinetic energy of the nuclei, the interaction between electrons, the interaction between the nuclei and the interaction between the electrons and the nuclei, as it appears schematized in Figure 2.1.

With the previous Hamiltonian, if we are able to solve Equation 2.1 and find the eigenvalue for the ground state, then we can compute some properties of matter such as elastic and thermal properties, phase diagrams, etc. [28]. Unfortunately for us, for most problems in quantum mechanics or quantum chemistry it is not possible to get an exact solution for Equation 2.1. For the problem that we encompass in this work, the differential equations that are contained in Equation 2.1 are not linear due to the interaction terms. For solving the equations we need to employ some approximations like the Born-Oppenheimer approximation.

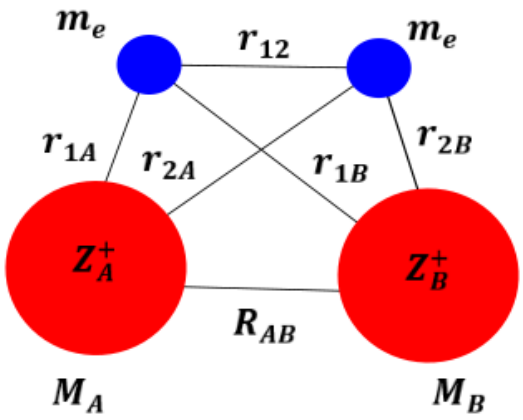

Figure 2.1: Atomic interaction in the system of many particles.

2.1.1 Born-Oppenheimer Approximation.

Equation 2.2 can be simplified by taking advantage of the huge difference between the masses of nuclei and electrons. For example the mass of a proton is roughly 1800 times greater than the electron's mass. In addition, in the nucleus of atoms there are neutrons with mass similar to the proton mass, so this give us an idea of the huge difference between nuclei and electrons. Therefore, nuclei move very slowly compared with electrons, and for that reason we assume that the nuclei are at rest. If the nuclei are at rest, it means that their kinetic energy is zero and the interaction between nuclei is constant [26].

$$H = -\sum_{i=1}^{N} \frac{\hbar^2}{2m_e}\nabla_i^2 + \sum_{i\neq j}^{N} \frac{e^2}{4\pi\epsilon_0}\frac{1}{|\vec{r}_i - \vec{r}_j|} - \sum_{i,A} \frac{e^2}{4\pi\epsilon_0}\frac{Z_A}{|\vec{r}_i - \vec{R}_A|} + E_{nuc} \tag{2.3}$$

To simplify more Equation 2.3 without the fundamental physical constants we use atomic units.

$$H = -\frac{1}{2}\sum_{i=1}^{N} \nabla_i^2 + \frac{1}{2}\sum_{i\neq j}^{N} \frac{1}{|\vec{r}_i - \vec{r}_j|} - \sum_{i,A} \frac{Z_A}{|\vec{r}_i - \vec{R}_A|} + E_{nuc} \tag{2.4}$$

$$H = -\frac{1}{2}\sum_{i=1}^{N} \nabla_i^2 + \frac{1}{2}\sum_{i=1}^{N}\sum_{j>i}^{N} \frac{1}{\vec{r}_{ij}} - \sum_{i=1}^{N}\sum_{A=1}^{L} \frac{Z_A}{\vec{r}_{iA}} + E_{nuc} \tag{2.5}$$

The Hamiltonian without the last term is called the electronic Hamiltonian, H_{ele}, because it just depends on the electron's coordinates.

$$H_{ele} = -\frac{1}{2}\sum_{i=1}^{N} \nabla_i^2 + \frac{1}{2}\sum_{i=1}^{N}\sum_{j>i}^{N} \frac{1}{\vec{r}_{ij}} - \sum_{i=1}^{N}\sum_{A=1}^{L} \frac{Z_A}{\vec{r}_{iA}} \tag{2.6}$$

Thus, the simplified version of the Hamiltonian in Equation 2.1 is given as:

$$H_{elec}\Psi_{elec} = E_{elec}\Psi_{elec} \tag{2.7}$$

And the total energy is:

$$E_{Tot} = E_{ele} + E_{nuc} \tag{2.8}$$

Equation 2.7 still presents certain obstacles to be solved, which will be presented in the next pages.

2.1.2 Hartree Product and Slater determinant

The electronic Hamiltonian H_{ele} (Equation 2.6) solely depends on the spatial coordinates of the electron $\vec{r} = (x, y, z)$. However for a complete description of the electron it is necessary to specify the spin $\alpha(\omega)$, and $\beta(\omega)$ which represent spin up and down [29]. Thus, the electron is completely described by four coordinates.

$$X = (\vec{r}, \omega) \tag{2.9}$$

Now we are ready to say that the wave functions for a system of N electrons depend on $X_1, X_2, \cdots, X_N$. In addition, antisymmetry under the exchange of the coordinates of any two electrons is the other requirement for the wave function [24] [29].

$$\Psi(X_1, \cdots, X_i, \cdots, X_j, \cdots, X_N) = -\Psi(X_1, \cdots, X_j, \cdots, X_i, \cdots, X_N) \tag{2.10}$$

Before analyzing the system's wave function where interactions occur, let's examine the case of a system with non-interacting electrons. The Hamiltonian in this case is:

$$H = \sum_{i=1}^{N} h(i) \tag{2.11}$$

where $h(i)$ is an operator that describes the kinetic and potential energy (the first and last term of Equation 2.6) of the electron i. For operator $h(i)$ there are a set of wave functions known as spin-orbital $\chi(X) = \psi(r)\alpha(\omega)$ or $\chi(X) = \psi(r)\beta(\omega)$. Equation 2.11, H is a result of sum of terms $h(i)$, where there is no interaction between electrons. Thus, the system's wave function is a product of spin-orbital functions known as Hartree Product (HP).

$$\Psi^{HP}(X_1, X_2, \cdots, X_N) = \chi_i(X_1)\chi_j(X_2)\cdots\chi_k(X_N) \tag{2.12}$$

$$H\Psi^{HP} = E\Psi^{HP} \tag{2.13}$$

The eigenvalue E of the system will be the sum of the energy of each electron for a given spin-orbital function, $E = \varepsilon_i + \varepsilon_j + \cdots + \varepsilon_k$

As we know, the wave function Ψ isn't an observable, and a physical interpretation can only be associated with the square of the wave function, which is the probability.

$$|\Psi^{HP}(X_1, \cdots, X_N)|^2 dX_1 \cdots dX_2 \tag{2.14}$$

Using Equation 2.12, the probability can be written for each electron. For instance, the probability of finding electron-one in the volume element dX_1, electron-two in dX_2 and so on, is given as:

$$|\chi_i(X_1)|^2 dX_1 |\chi_j(X_2)|^2 dX_2 \cdots |\chi_k(X_N)|^2 dX_N \tag{2.15}$$

The previous expression means that the probability of finding an electron i in the volume element dX_i is independent of the position of the other electrons in a system of many electrons. As we assumed in Equation 2.11, we neglected the interaction between electrons. In the real world, an i electron senses the presence of another electron in the space due to Coulomb interaction. So that, the i electron avoids the regions occupied by the other electrons. Thus, we have that the position of an electron is explicitly correlated with the positions of the other electrons [29]. Therefore, if we want to describe well our system we need to consider the electronic correlation.

As we already mentioned, another requirement for the wave function is antisymmetry (Equation 2.10). The Hartree product (Equation 2.12) doesn't fulfill the antisymmetry principle by itself. To explain how to get antisymmetric wave functions, consider two electrons which can occupy the following spin-orbitals χ_i and χ_j. As we know, the wave function can be written as the product of the spin-orbitals.

$$\Psi_{12}^{HP}(X_1, X_2) = \chi_i(X_1)\chi_j(X_2) \tag{2.16}$$

If we change the spin-orbital for each electron, we have:

$$\Psi_{21}^{HP}(X_1, X_2) = \chi_i(X_2)\chi_j(X_1) \tag{2.17}$$

Employing the previous expressions, we can build a wave function which fulfills the antisymmetry principle by taking the appropriate linear combination of these Hartree products [29].

$$\Psi(X_1, X_2) = \frac{1}{\sqrt{2}}[\Psi_{12}^{HP} + \Psi_{21}^{HP}] = \frac{1}{\sqrt{2}}[\chi_i(X_1)\chi_j(X_2) - \chi_j(X_1)\chi_i(X_2)] \tag{2.18}$$

As we can see, $\Psi(X_1, X_2) = -\Psi(X_2, X_1)$, so the wave function accomplish the antisymmetry principle. From Equation 2.18 it's evident that the wave function is zero when both electrons have the same spin-orbital, $i = j$. Therefore, from Equation 2.18 we conclude that two electrons cannot occupy the same spin-orbital [29]. It means that electrons with same spin are correlated.

There is a statement in quantum mechanics, called the **spin-statistics theorem**, which establishes that the wave functions of a system of identical particles with half-integer spin (fermions) must be antisymmetric with respect to the interchange of any two particles. The wave functions for particles with integer spin (bosons) must be symmetric [30].

For an N-electron system, there is a generalization of Equation 2.18.

$$\Psi(X_1, X_2, \cdots, X_N) = \frac{1}{\sqrt{N!}} \begin{bmatrix} \chi_i(X_1) & \chi_j(X_1) & \cdots & \chi_k(X_1) \\ \chi_i(X_2) & \chi_j(X_2) & \cdots & \chi_k(X_2) \\ \vdots & \vdots & \ddots & \vdots \\ \chi_i(X_N) & \chi_j(X_N) & \cdots & \chi_k(X_N) \end{bmatrix} \tag{2.19}$$

The Slater determinant in brackets has N electrons occupying N spin-orbitals $(\chi_i, \chi_j, \cdots, \chi_k)$. It's evident that the interchange of two columns changes the sign of the determinant which is agree with the antisymmetric nature of the wave functions [27] [29].

2.1.3 Hartree-Fock Approximation

In the previous section we took a look at H_{ele} (Equation 2.6) without considering the interaction term between electrons. Now, we are in a position to make a step forward for solving the expression $H_{ele}|\Psi_{ele}\rangle = \varepsilon|\Psi_{ele}\rangle$. It's very important to keep in mind that the nuclei interaction is a parameter and it means that Ψ_{ele} depends only on the electronic coordinates.

The basic idea behind the Hartree-Fock (HF) method is to approximate the interaction term of Equation 2.6 by an average potential, $v^{HF}(i)$, experienced by the i^{th} electron due to the presence of the other electrons[29].

$$f(i) = -\frac{1}{2}\nabla_i^2 - \sum_{A=1}^{L} \frac{Z_A}{\vec{r}_{iA}} + v^{HF}(i) \tag{2.20}$$

$f(i)$ is called the effective one-electron operator or Fock operator and $v^{HF}(i)$ is the HF potential . So, the eigenvalue equation is given as:

$$f(i)\chi(X_i) = \varepsilon\chi(X_i) \tag{2.21}$$

Thus Equation 2.21 is nonlinear and must be solved iteratively and this method is called self-consistent-field (SCF).

For SCF method, you start with an initial guess for spin-orbitals, $\chi(X_i)$, which is used to compute the HF potential, $v^{HF}(i)$ experienced by each electron. Then solve Fock's equation (Equation 2.21) to get a new set of spin-orbitals. Using these new spin-orbitals, one can compute new HF potential and repeat the procedure until self-consistency is achieved (until the $v^{HF}(i)$ no longer change)[29].

Now let's see the explicit form of Equation 2.20. We begin splitting in two parts Equation 2.6 for a better analysis.

$$G_1 = \sum_{i}^{N} h(\vec{r}_i) \quad with \quad h(\vec{r}_i) = -\frac{1}{2}\nabla_i^2 - \sum_{A=1}^{L} \frac{Z_A}{\vec{r}_{iA}} \tag{2.22}$$

$$G_2 = \frac{1}{2}\sum_{i=1}^{N}\sum_{j>i}^{N} \frac{1}{\vec{r}_{ij}} \tag{2.23}$$

Now we proceed to calculate the expectation value for G_1 on a given state Ψ_0, where this state is defined as: $|\Psi_0\rangle = |\chi_1, \chi_2, \cdots, \chi_i, \chi_j, \cdots, \chi_N\rangle$ according to Equation 2.19

$$\langle\Psi_0|G_1|\Psi_0\rangle = \frac{1}{N!}\sum_i \langle det\{\chi_1,\chi_2,\cdots,\chi_i,\chi_j,\cdots,\chi_N\}|h|det\{\chi_1,\chi_2,\cdots,\chi_i,\chi_j,\cdots,\chi_N\}\rangle \tag{2.24}$$

For the previous expression, we can only choose identical permutation in the determinant left part, since the rest of $N!-1$ permutations would yield the same result as selected one [27]. The spin-orbitals are perpendicular to each other, $\langle\chi_i|\chi_j\rangle = \delta_{ij}$, it's evident that only identical permutation survives in the determinant on the right part of Equation 2.27 [27] [29].

$$\langle\Psi_0|G_1|\Psi_0\rangle = \sum_i \langle\chi_1,\chi_2,\cdots,\chi_i,\chi_j,\cdots,\chi_N|h|\chi_1,\chi_2,\cdots,\chi_i,\chi_j,\cdots,\chi_N\rangle \tag{2.25}$$

$$\langle\Psi_0|G_1|\Psi_0\rangle = \sum_i \langle\chi_i|h|\chi_i\rangle \tag{2.26}$$

Something similar we have for the expectation value G_2:

$$\langle\Psi_0|G_2|\Psi_0\rangle = \frac{1}{N!}\langle det\{\chi_1,\chi_2,\cdots,\chi_N\}|G_2|det\{\chi_1,\chi_2,\cdots,\chi_N\}\rangle \tag{2.27}$$

$$\langle\Psi_0|G_2|\Psi_0\rangle = \frac{1}{2}\sum_{ij}\left[\langle\chi_i\chi_j|\frac{1}{\vec{r}_{12}}|\chi_i\chi_j\rangle - \langle\chi_i\chi_j|\frac{1}{\vec{r}_{12}}|\chi_j\chi_i\rangle\right] \tag{2.28}$$

$$\langle\Psi_0|G_2|\Psi_0\rangle = \frac{1}{2}\sum_{ij}\langle\chi_i\chi_j|\frac{1}{\vec{r}_{12}}|\chi_i\chi_j\rangle - \frac{1}{2}\sum_{ij}\langle\chi_i\chi_j|\frac{1}{\vec{r}_{12}}|\chi_j\chi_i\rangle \tag{2.29}$$

For above expression, the first term is the Coulomb contribution and the second one is the Exchange contribution, and the terms cancel each other if $i \equiv j$. To be more explicit for the expression for the spin-orbitals in the angle brackets, let's depict both in the integral form.

For the Coulomb contribution we have:

$$\langle\chi_i(\boldsymbol{X_1})\chi_j(\boldsymbol{X_2})|\frac{1}{\vec{r}_{12}}|\chi_i(\boldsymbol{X_1})\chi_j(\boldsymbol{X_2})\rangle = \int d\boldsymbol{X_1}d\boldsymbol{X_2}|\chi_i(\boldsymbol{X_1})|^2\frac{1}{|\vec{\boldsymbol{r}}_{\boldsymbol{1}}-\vec{\boldsymbol{r}}_{\boldsymbol{2}}|}|\chi_j(\boldsymbol{X_2})|^2 \tag{2.30}$$

Simplifying our notation, $\chi_a(X_b) = \chi_a(b)$ and $dX \equiv d\vec{r}$ but without the spin coordinate.

$$\langle\chi_i(\boldsymbol{1})\chi_j(\boldsymbol{2})|\frac{1}{\vec{r}_{12}}|\chi_i(\boldsymbol{1})\chi_j(\boldsymbol{2})\rangle = \int d\vec{\boldsymbol{r}}_{\boldsymbol{1}}d\vec{\boldsymbol{r}}_{\boldsymbol{2}}|\chi_i(\boldsymbol{1})|^2\frac{1}{|\vec{\boldsymbol{r}}_{\boldsymbol{1}}-\vec{\boldsymbol{r}}_{\boldsymbol{2}}|}|\chi_j(\boldsymbol{2})|^2 \tag{2.31}$$

For the exchange contribution we have:

$$\langle\chi_i(\boldsymbol{1})\chi_j(\boldsymbol{2})|\frac{1}{\vec{r}_{12}}|\chi_j(\boldsymbol{1})\chi_i(\boldsymbol{2})\rangle = \int d\vec{\boldsymbol{r}}_{\boldsymbol{1}}d\vec{\boldsymbol{r}}_{\boldsymbol{2}}\chi_i^*(\boldsymbol{1})\chi_j(\boldsymbol{1})\frac{1}{|\vec{\boldsymbol{r}}_{\boldsymbol{1}}-\vec{\boldsymbol{r}}_{\boldsymbol{2}}|}\chi_j^*(\boldsymbol{2})\chi_i(\boldsymbol{2}) \tag{2.32}$$

As we known for Equation 2.6, the electronic Hamiltonian is the combination of G_1 and G_2. Thus, the expectation value for the Hamiltonian on a given state Ψ_0 is:

$$E_0 = \langle\Psi_0|H|\Psi_0\rangle = \langle\Psi_0|G_1+G_2|\Psi_0\rangle \tag{2.33}$$

$$E_0 = \sum_i\langle\chi_i|h|\chi_i\rangle + \frac{1}{2}\sum_{ij}\left[\langle\chi_i\chi_j|\frac{1}{\vec{r}_{12}}|\chi_i\chi_j\rangle - \langle\chi_i\chi_j|\frac{1}{\vec{r}_{12}}|\chi_j\chi_i\right] \tag{2.34}$$

According to the variational principle, the N spin-orbitals χ_i vary, so that the energy $E_0 = E_0(\{\chi_i\})$ achieves its minimum value [27] [29]. Thus, for the variation of the functional $E_0(\{\chi_i\})$ we employ the Lagrange multipliers technique. For instance, the variation of the first term, $\langle\chi_i|h|\chi_i\rangle$, is $\langle\delta\chi_i|h|\chi_i\rangle + \langle\chi_i|h|\delta\chi_i\rangle$. As with the first term, something similar we have for the second. In the end, applying the stationary condition $\delta E_0(\{\chi_i\}) = 0$ we get the following expression.

$$0 = \sum_i\langle\delta\chi_i|h|\chi_i\rangle + \sum_{ij}\left[\langle\delta\chi_i\chi_j|\frac{1}{\vec{r}_{12}}|\chi_i\chi_j\rangle - \langle\delta\chi_i\chi_j|\frac{1}{\vec{r}_{12}}|\chi_j\chi_i\right] - \sum_i\varepsilon_i\langle\delta\chi_i|\chi_i\rangle \tag{2.35}$$

The equation for the best spin-orbitals is the Hartee-Fock integro-differential equation. **Note**: remembering our notation for the spin-orbital $\boldsymbol{X} = (\boldsymbol{r}, \boldsymbol{\omega})$ (Equation 2.9) combine the spatial coordinate and the spin.

$$h(\mathbf{1})\chi_i(\mathbf{1}) + \sum_{j \neq i} \left[\int d\boldsymbol{X} |\chi_j(\boldsymbol{X})|^2 \frac{1}{|\vec{r}_1 - \vec{\boldsymbol{r}}|} \right] \chi_i(\mathbf{1}) - \sum_{j \neq i} \left[\int d\boldsymbol{X} \chi_j^*(\boldsymbol{X}) \chi_i(\boldsymbol{X}) \frac{1}{|\vec{r}_1 - \vec{\boldsymbol{r}}|} \right] \chi_j(\mathbf{1}) = \varepsilon_i \chi_i(\mathbf{1}) \tag{2.36}$$

The following is the kinetic energy and potential energy experienced by electron-one owing the attraction to the nuclei [29].

$$h(\mathbf{1}) = -\frac{1}{2}\nabla_1^2 - \sum_A^L \frac{Z_A}{\vec{r}_1 - \boldsymbol{r}_A} \tag{2.37}$$

2.1.3.1 The Coulomb and Exchange Operators

The Coulomb term originally represented the interaction between two electrons $(\vec{r}_{12})^{-1}$, but in the Hartree-Fock approximation, electron-one in χ_i experiences a one-electron Coulomb potential in χ_j [29] .

$$v_i^{coul} \chi_i(X) = \sum_{j \neq i} \chi_i(X) \int d\boldsymbol{X'} |\chi_j(\boldsymbol{X'})|^2 \frac{1}{|\vec{r}_i - \boldsymbol{r'}|} \tag{2.38}$$

The exchange term, arising due to the antisymmetric nature of the wave function, i:

$$v_i^{exch} \chi_i(X) = \sum_{j \neq i} \chi_j(X) \int d\boldsymbol{X'} \chi_j^*(\boldsymbol{X'}) \chi_i(\boldsymbol{X'}) \frac{1}{|\vec{r}_i - \boldsymbol{r'}|} \tag{2.39}$$

2.2 Electron density

In Equation 2.14, we introduced the idea of simultaneous probability of finding electron-one at spin-orbit X_1, electron-two at X_2 and so forth. **Note:** in this section we will return to our notation $\vec{r}$ instead of X for convenience. There are situations where we are interested in the total charge density, which is defined as the probability to find any electron at a particular position [28]. For a system where there are N electrons and L nuclei (see section 2.1) the probability is:

$$P(\vec{r}_1 = \vec{r}) = \int |\Psi(\vec{r}, \vec{r}_2, \cdots, \vec{r}_N; \vec{R}_1, \cdots, \vec{R}_L)|^2 d\vec{r}_2 \cdots d\vec{r}_N d\vec{R}_1 \cdots d\vec{R}_L \tag{2.40}$$

The probability of finding any electron at position $\vec{r}$ (electron density), is:

$$n(\vec{r}) = P(\vec{r}_1 = \vec{r}) + P(\vec{r}_2 = \vec{r}) + \cdots + P(\vec{r}_N = \vec{r}) = \sum_i^N |\Psi_i(\vec{r})|^2 \tag{2.41}$$

The electrons are indistinguishable particles, which means that each term in Equation 2.41 is given by Equation 2.40 [26].

$$n(\vec{r}) = N \int |\Psi(\vec{r}, \vec{r}_2, \cdots, \vec{r}_N; \vec{R}_1, \cdots, \vec{R}_L)|^2 d\vec{r}_2 \cdots d\vec{r}_N d\vec{R}_1 \cdots d\vec{R}_L \tag{2.42}$$

The previous equation is very important in this work, because as we will see in the next pages, all properties of the system can be determined from a unique functional of the ground state density [31]. The electron density is an observable and can be measured experimentally by X-ray diffraction.

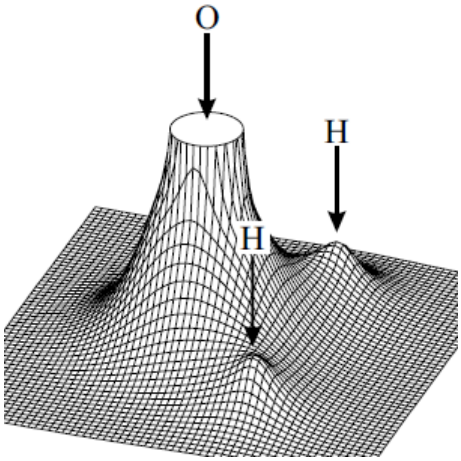

(a) The $n(\vec{r})$ projected onto the plane [26]

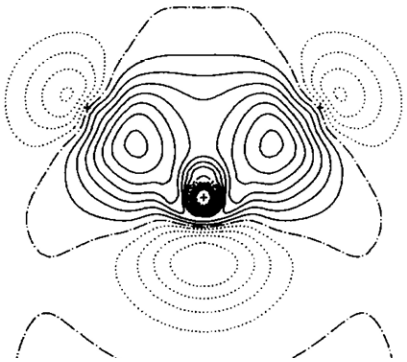

(b) Contour lines for electron density [32]

Figure 2.2: Representation of the electron density of the water molecule, H_2O

Figure 2.2 is an example of the representation of electron density. The cusp that appears is a consequence of the singularity in the Hamiltonian (Equation 2.6) when $r_{iA} \to 0$, so at any position of an atom the density $n(\vec{r})$ exhibits a maximum due to the attractive force exerted by the nuclei [26] [32]. In the oxygen atom, the maximum is more noticeable because it has more positive charges (protons) than hydrogen atoms.

2.3 Density functional theory

Density Functional Theory (DFT) is a quantum-mechanical method used in physics and chemistry to study the electronic structure of atoms and molecules[33]. The method employs a certain type of functions called functionals that depend on the electron density (Equation 2.42). Today, thanks to computers and theoretical studies in this area, there are a wide variety of functionals which can be employed to study different sorts of systems. On the following pages, we will discuss more about the types of functionals.

The main difficulty presented by the many-body problem is non-linearity of differential equations but the other challenge is the quantity of variable to manage. For instance, for a system with N electrons we will have a wave function of $3N$ Cartesian spatial coordinates $\Psi(\vec{r}_1, \vec{r}_2, \cdots, \vec{r}_N)$ with $\vec{r} = (x, y, z)$. Thus, the reduction of variables is convenient[28].

$$E = \langle \Psi | H | \Psi \rangle = \int d\vec{r}_1 \cdots d\vec{r}_N \Psi^*(\vec{r}_1, \cdots, \vec{r}_N) H \Psi(\vec{r}_1, \cdots, \vec{r}_N) \tag{2.43}$$

The central idea of the DFT is that the energy E of the system only depends on the electron density [26], so that.

$$E = F[n] \tag{2.44}$$

Although the energy of a quantum state is generally a functional of the entire wave function $\Psi(\vec{r}_1, \vec{r}_2, \cdots, \vec{r}_N)$, which contains $3N$ variables, the ground state energy (Equation 2.44) depends on $n(\vec{r})$, which is a function of three variables only [28] .

2.3.1 Hohenberg-Kohn theorems

Theorem 1 *The external potential $V_{ext}(\vec{r})$ depends solely on electron density $n(\vec{r})$. Owing to the external potential define the Hamiltonian, $\hat{H}$ of the system, the ground state of the system is functional only on electron density $n(\vec{r})$ [26] .*

To prove the theorem, we are going to use the Hamiltonian (Equation 2.4) that appears in the Born-Oppenheimer approximation (see subsection 2.1.1) without the term E_{nuc}.

$$H = -\frac{1}{2}\sum_{i=1}^{N}\nabla_i^2 + \frac{1}{2}\sum_{i\neq j}^{N}\frac{1}{|\vec{r}_i - \vec{r}_j|} - \sum_i V_n(\vec{r}_i) \tag{2.45}$$

$V_n(r)$ is the Coulomb potential (external potential) of the nuclei experienced by electrons.

$$V_n(\vec{r}) = -\sum_A \frac{Z_A}{|\vec{r} - \vec{R}_A|} \tag{2.46}$$

For convenience, let's introduce some symbolic notations for kinetic energy and for the Coulomb interaction.

$$\hat{T} = -\frac{1}{2}\sum_{i=1}^{N}\nabla_i^2 \qquad ; \qquad \hat{W} = \frac{1}{2}\sum_{i\neq j}^{N}\frac{1}{|\vec{r}_i - \vec{r}_j|} \tag{2.47}$$

Thus, substituting the previous Hamiltonian in Equation 2.43, we have:

$$E = \langle\Psi|\sum_i V_n(\vec{r}_i)|\Psi\rangle + \langle\Psi|\hat{T} + \hat{W}|\Psi\rangle \tag{2.48}$$

Using the relation between electron density (Equation 2.42) and wave function, the first term can be rewritten.

$$E = \int n(\vec{r})V_n(\vec{r})d\vec{r} + \langle\Psi|\hat{T} + \hat{W}|\Psi\rangle \tag{2.49}$$

Now let's suppose that the wave function, Ψ is the wave function that corresponds to the ground state energy, E_0, and of course for the potential V_n and electron density n_0. In addition, suppose that there is another potential, $V_n' \neq V_n$ with the same electron density, n, with wave function Ψ' and ground state energy E' [28]. Thus, we have:

$$E' = \langle\Psi'|\sum_i V_n'(\vec{r}_i)|\Psi'\rangle + \langle\Psi'|\hat{T} + \hat{W}|\Psi'\rangle \tag{2.50}$$

As we suppose, Ψ' is the wave function that corresponds to the energy E'. Since Ψ is not the wave function associated with the ground state energy E', the following is true:

$$\langle\Psi|\sum_i V_n'(\vec{r}_i)|\Psi\rangle + \langle\Psi|\hat{T} + \hat{W}|\Psi\rangle > E' \tag{2.51}$$

$$\int n(\vec{r})V_n'(\vec{r})d\vec{r} + \langle\Psi|\hat{T} + \hat{W}|\Psi\rangle > E' \tag{2.52}$$

Employing Equation 2.49 and subtracted with the previous, we have:

$$E - E' > \int n(\vec{r})V_n(\vec{r})d\vec{r} - \int n(\vec{r})V_n'(\vec{r})d\vec{r} \tag{2.53}$$

We can repeat the entire reasoning by simply starting from V_n instead of V_n'. In this case we would find that:

$$E' - E > \int n(\vec{r})V_n'(\vec{r})d\vec{r} - \int n(\vec{r})V_n(\vec{r})d\vec{r} \tag{2.54}$$

Adding up Equation 2.53 with 2.54, we found that $0 > 0$ which is not true. Due to this incongruity, the possibility that two different external potential V_n' and V_n, lead to the same ground state density, n, is not true [28].

Theorem 2 *The functional $F[n]$ that yields energetically the most stable state of the system, gives the lowest energy if and only if the true electron density n_0 of the ground state is given. [26]. Let's define:*

$$E_0 \leqslant \bar{E} = F[\bar{n}] = \int \bar{n}(\vec{r})\bar{V}_n'(\vec{r})d\vec{r} + \langle\bar{\Psi}|\hat{T} + \hat{W}|\bar{\Psi}\rangle \tag{2.55}$$

The previous expression means that the trial density $\bar{n}$ is the upper limit of the true ground energy, E_0, which $\bar{n}$ satisfies $\bar{n} \geqslant 0$ and $\int \bar{n}(\vec{r})d\vec{r} = N$, and also it has its corresponding external potential $\bar{V}$, which fixes its own Hamiltonian $\bar{H}$ and therefore its own wave function $\bar{\Psi}$[26]. This wave function can be considered as a trail wave function for the Hamiltonian H, which is produced by the external potential V.

$$\langle\bar{\Psi}|H|\bar{\Psi}\rangle = \int \bar{n}(\vec{r})V_n(\vec{r})d\vec{r} + \langle\bar{\Psi}|\hat{T} + \hat{W}|\bar{\Psi}\rangle \tag{2.56}$$

As we defined before (Equation 2.42), the density depends on the wave function, therefore $\bar{n}$ depends on $\bar{\Psi}$ which is the trial wave function.

$$\langle\bar{\Psi}|H|\bar{\Psi}\rangle = \int \bar{n}(\vec{r})V_n(\vec{r})d\vec{r} + \langle\bar{\Psi}|\hat{T} + \hat{W}|\bar{\Psi}\rangle = F[\bar{n}] = E \geqslant E_0 = \langle\Psi_0|H|\Psi_0\rangle \tag{2.57}$$

The equality, $E = E_0$ can be reached in the case when $\bar{n} = n_0$, because **Theorem 1** ensures that the same external potential, V leads to a unique density, n, in this case the density of the ground state, n_0. In the end, we have that the functional $F[\bar{n}]$ delivers the ground state energy if it inputs the true ground state density.

2.3.2 Kohn-Sham equations

In the previous pages, we introduced the concept of electron density $n(\vec{r})$. The Hohenberg-Kohn theorems told us in few words that the ground state energy is a unique functional of this density. In this part of the work, we will see one of the most popular methods for finding the electron density.

Equation 2.44 means that there is a functional $F[n(\vec{r})]$ that depends on the density only, $n(\vec{r})$, and in Equation 2.49 there is an expression for this dependence. Combining both ideas, we have:

$$F[n(\vec{r})] = \int n(\vec{r})V_n(\vec{r})d\vec{r} + \langle\Psi(\vec{r})|\hat{T} + \hat{W}|\Psi(\vec{r})\rangle \tag{2.58}$$

For the previous expression, the terms $\hat{T}$ and $\hat{W}$ are the kinetic energy and the Coulomb interaction respectively, which depend implicitly on the density $n(\vec{r})$. Now, we are going to write this dependence explicitly using Equations 2.47 and 2.41.

$$\hat{T}[n(\vec{r})] = -\frac{1}{2}\sum_i^N \langle\Psi_i(\vec{r})|\nabla^2|\Psi_i(\vec{r})\rangle \tag{2.59}$$

$$\hat{T}[n(\vec{r})] = -\frac{1}{2}\sum_i^N \int |\nabla\Psi_i(\vec{r})|^2 d\vec{r} \tag{2.60}$$

$$\hat{W}[n(\vec{r})] = \frac{1}{2}\sum_{i=1}^N\sum_{j>i}^N \int\int |\Psi_i(\vec{r})|^2 \frac{1}{|\vec{r} - \boldsymbol{r'}|}|\Psi_j(\boldsymbol{r'})|^2 d\vec{r}d\boldsymbol{r'} \quad ; \quad \vec{r} = (x, y, z) \neq \boldsymbol{r'} = \boldsymbol{(x', y', z')} \tag{2.61}$$

$$\hat{W}[n(\vec{r})] = \frac{1}{2}\int\int \frac{n(\vec{r})n(\boldsymbol{r'})}{|\vec{r} - \boldsymbol{r'}|} d\vec{r}d\boldsymbol{r'} \tag{2.62}$$

Kohn and Sham introduced an extra term in Equation 2.58:

$$F[n(\vec{r})] = \int n(\vec{r})V_n(\vec{r})d\vec{r} + \hat{T}[n(\vec{r})] + \hat{W}[n(\vec{r})] + E_{XC}[n(\vec{r})] \tag{2.63}$$

Where $E_{XC}[n(\vec{r})]$ represents everything that we did not take into account for the system of non-interacting particles. This extra term is called the exchange-correlation energy [26] [28] [31].

According with the **Theorem 2** the energy E of the system is minimum when we have the true ground state density, n_o. In this case the minimum can be computed using the variational derivative.

$$\frac{\delta F[n(\vec{r})]}{\delta n(\vec{r})} = 0 \tag{2.64}$$

Applying the ideas of variational derivative, this leads us to an equation of wave functions (Equation 2.65), where the orbitals $\phi_i(\vec{r})$ must fulfill the following constrain $\langle\phi_i|\phi_j\rangle = \delta_{ij}$. The orbitals are called "Kohn-Sham orbitals" and don't have a physical meaning but they are only an auxiliary tool for solving the self-consistent (SC) problem and compute the true density for the ground state [34].

$$\left[-\frac{1}{2}\nabla^2 + V_n(\vec{r}) + V_H(\vec{r}) + V_{XC}(\vec{r})\right]\phi_i(\vec{r}) = \epsilon_i\phi_i(\vec{r}) \tag{2.65}$$

The terms $V_H(\vec{r})$ and $V_{XC}(\vec{r})$ are defined as:

$$V_H(\vec{r}) = \int d\boldsymbol{r'}\frac{n(\boldsymbol{r'})}{|\vec{r}-\boldsymbol{r'}|} \quad ; \quad V_{XC}(\vec{r}) = \frac{\delta E_{XC}[n]}{\delta n} \tag{2.66}$$

The first term is the kinetic energy of the electrons in a system of non-interacting particles, $V_n(\vec{r})$ is the external potential (Equation 2.46), $V_H(\vec{r})$ is the Hartree potential and $V_{XC}(\vec{r})$ is the exchange-correlation potential.

$$\left[-\frac{1}{2}\nabla^2 + V_{eff}(\vec{r})\right]\phi_i(\vec{r}) = \epsilon_i\phi_i(\vec{r}) \tag{2.67}$$

Equation 2.65 often is expressed in terms of effective potential and kinetic energy of electron i. Therefore, electron i moves under effective potential V_{eff}, which contains terms that we have already mentioned. Equation 2.65 or 2.67 looks similar to the Schrödinger equation, but is called the Kohn-Sham equation. The equation describes a system of non-interacting particles that give place to a density (Equation 2.68) equal to the density of system where there are interactions between particles.

$$n(\vec{r}) = \sum_i^N |\phi_i(\vec{r})|^2 \tag{2.68}$$

Equation 2.65 is in principle exact and the approximation only enters in the unknown functional for the exchange-correlation energy, E_{XC}. Thus, the aim of DFT is to find a better approximation for this quantity [26].

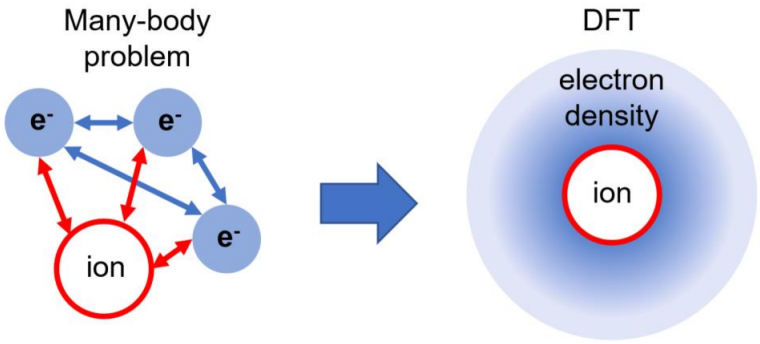

Figure 2.3: Schematic illustration of transforming many-electron system to electron density, $n(\vec{r})$ [1]

2.3.3 Exchange-correlation functionals

2.3.3.1 Jacob's Ladder

DFT provides practical estimates for the ground-state energy and electron density of a many-electron system. In particular, it predicts the sizes and shapes of molecules, the crystal structures of solids and the work required to stretch or break chemical bonds [35].

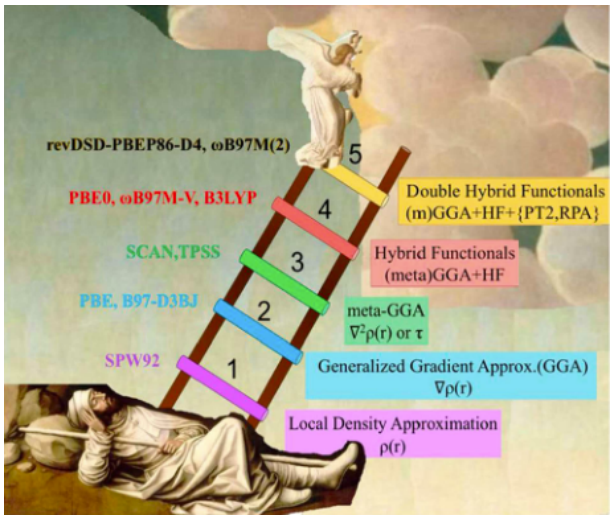

Figure 2.4: Illustration of Jacob's Ladder of DFT [2]

As we mentioned, in Equation 2.65, V_{XC} (which is related with E_{XC}) is the only unknown term and its value is approximated. The real usefulness of density functional theory arises from the possibility of making simple but accurate approximations for the functional $E_{XC}[n]$ [35]. The proliferation of approximate exchange-correlation functionals has led to the functional zoo.

Owing to the wide variety of functionals that have been developed, there is a hierarchy where the functionals are located according with the parameters and the accuracy that each one has to describe the system. The hierarchy of the approximation is a kind of ladder lifted up to the goal of "chemical accuracy" or "Heaven" (Figure 2.4). Heaven is the elusive goal of the exact exchange-correlation functional, and thus the exact solution of the Schrödinger equation [2] [35].

As you climb the ladder (Figure 2.4), the functionals retain the previous step parameters and incorporate others. We will give a description of some of the rungs, since the various functionals used in this work belong to different rungs.

2.3.3.2 Local Spin Density Approximation, LSDA

This is one of the most popular approaches to exchange-correlation (XC) functionals. To begin considering the LSDA let's start with the simplest version of it, which is the Local Density Approximation (LDA). For LDA the exchange-correlation energy depends on the total density $n(\vec{r})$ (Equation 2.68):

$$E_{XC}^{LDA}[n(\vec{r})] = \int \varepsilon_{xc}(n(\vec{r}))n(\vec{r})d\vec{r} \equiv \int \varepsilon_{xc}n(\vec{r})d\vec{r} \tag{2.69}$$

Where ε_{xc} is the many-body exchange-correlation energy per electron of a uniform gas of interacting electrons [27]. For the potentials, we will use Equation 2.66.

Let's define $L = L(\vec{r}, n(\vec{r}), n'(\vec{r})) = \varepsilon_{xc}(n(\vec{r}))n(\vec{r})$ and applying the variational derivative we have:

$$\int \frac{\delta E[n]}{\delta n}\varphi(\vec{r})d\vec{r} = \int \left[\frac{\partial L}{\partial n} - \frac{d}{d\vec{r}}\frac{\partial L}{\partial n'}\right]\varphi(\vec{r})d\vec{r} \tag{2.70}$$

Thus, the exchange-correlation potential is given by:

$$V_{XC} = \frac{\delta E_{XC}^{LDA}[n]}{\delta n} = \frac{\partial L}{\partial n} - \frac{d}{d\vec{r}}\frac{\partial L}{\partial n'} \tag{2.71}$$

We note that $\frac{\partial L}{\partial n'} = 0$, because L doesn't depend on the derivative of the density, n', which simplifies the process to get V_{XC}^{LDA}

$$V_{XC}^{LDA} = n(\vec{r})\frac{d\varepsilon_{xc}(n(\vec{r}))}{dn(\vec{r})} + \varepsilon_{xc}(n(\vec{r})) \tag{2.72}$$

Now, let's consider the general version, which is LSDA. For this version, the exchange-correlation energy depends on the spin-up ($n_\uparrow$) and spin-down ($n_\downarrow$) densities [31].

$$E_{XC}^{LSDA}[n_\uparrow, n_\downarrow] = \int \varepsilon_{xc}(n_\uparrow, n_\downarrow)n(\vec{r})d\vec{r} \tag{2.73}$$

As we know, $n(\vec{r})$ is the total density, $n(\vec{r}) = n_\uparrow + n_\downarrow$. Also we have that, $\varepsilon_{xc}(n_\uparrow, n_\downarrow)$ can be written in two parts:

$$\varepsilon_{xc} = \varepsilon_x(n_\uparrow, n_\downarrow) + \varepsilon_c(n_\uparrow, n_\downarrow) \tag{2.74}$$

$$E_{XC}^{LSDA}[n_\uparrow, n_\downarrow] = E_X^{LSDA} + E_C^{LSDA} = \int \varepsilon_x(n_\uparrow, n_\downarrow)n(\vec{r})d\vec{r} + \int \varepsilon_c(n_\uparrow, n_\downarrow)n(\vec{r})d\vec{r} \tag{2.75}$$

Now, we are in the position to introduce the fractional spin polarization, $\Gamma = \Gamma(\vec{r})$

$$\Gamma = \frac{n_\uparrow - n_\downarrow}{n_\uparrow + n_\downarrow} = \frac{n_\uparrow - n_\downarrow}{n} \tag{2.76}$$

To compute the exchange-correlation potential (Equation 2.66), we can perform that by parts. As an example, let's take just the exchange term from Equation 2.75.

$$E_X[n_\uparrow, n_\downarrow] = \frac{1}{2}\left(E_X[2n_\uparrow] + E_X[2n_\downarrow]\right) \tag{2.77}$$

Equation 2.77 is called the "spin-scaling relation" and $E_X(n)$ is the exchange energy of an unpolarized system of density n. Employing the fractional spin polarization, densities are rewritten.

$$n_\uparrow = n\frac{1+\Gamma}{2} \quad ; \quad n_\downarrow = n\frac{1-\Gamma}{2} \tag{2.78}$$

Rewriting Equation 2.77 in terms of the fractional spin polarization, we get:

$$E_X[n_\uparrow, n_\downarrow] = \frac{1}{2}(E_X[n(1+\Gamma)] + E_X[n(1-\Gamma)]) \tag{2.79}$$

Since Γ depends on the densities implicitly, the following is true:

$$E_X^{LDA}[n_\uparrow, n_\downarrow] = \int d\vec{r}n(\vec{r})\varepsilon_x^{LDA}(n_\uparrow(\vec{r}), n_\downarrow(\vec{r})) \tag{2.80}$$

Where ε_x^{LDA} is the exchange energy per electron for a uniform gas of interacting electrons. The correlation energy, E_C is more difficult to cast in terms of a functional, but its contribution to the total energy is much smaller than the E_X [31] [36].

2.3.3.3 Generalized Gradient Approximation, GGA

As we already know, Equation 2.73 depends on the quantities of spin-up and spin-down densities. Now we present the GGA which is an improvement of the LSDA.

$$E_{XC}^{GGA}[n_\uparrow, n_\downarrow] = \int d\vec{r}f(n_\uparrow, n_\downarrow, \nabla n_\uparrow, \nabla n_\downarrow) \tag{2.81}$$

As seen, GGA depends on electron density and on the gradient of the electronic densities. Thus, functionals belong to this rung of Jacob's ladder are know as semi-local XC functionals. In comparison with LSDA, GGA functionals tend to improve total energies, atomization energies, energy barriers and structural energy differences. Typically, GGA functionals favor density inhomogeneity more than LSDA does [37].

Employing the same ideas as what we used in LSDA (Equation 2.75), the exchange-correlation energy can be written in two parts, $E_{XC} = E_X + E_C$

It is important to mention that there are many ways to build the GGA functional. For instance, here is an expression for the GGA correlation energy:

$$E_C^{GGA}[n_\uparrow, n_\downarrow] = \int d\vec{r} n[\varepsilon_C(r_s, \Gamma) + H(r_s, \Gamma, t)] \tag{2.82}$$

where r_s is the local Seitz radius ($n = 3/4\pi r_s^3 = k_F^3/3\pi^2$), $t = |\nabla n|/2\phi k_s n$ is a dimensionless density gradient, Γ is the fractional of spin polarization (Equation 2.76), $\phi(\Gamma) = [(1+\Gamma)^{2/3} + (1-\Gamma)^{2/3}]/2$ and $k_s = \sqrt{4k_F/\pi a_0}$ is the Thomas-Fermi wave number ($a_0 = \hbar^2/me^2$).

In the same way, there is an expression for the GGA exchange energy:

$$E_X^{GGA}[n_\uparrow, n_\downarrow] = \int d\vec{r} n \varepsilon_X(n) F_X(s) \tag{2.83}$$

$F_X(s)$ is a dimensionless parameter with the following shape:

$$F_X(s) = 1 + k - \frac{k}{1 + \mu s^2/k} \tag{2.84}$$

where k and μ are parameters, and $s = |\nabla n|/2k_F n = (r_s/a_0)^{1/2}\phi t/c$ is another gradient density with c as another parameter adjusted to the system. For more information about how to construct GGA functionals see the paper of Perdew *et al.* [37]. As we saw, GGA involves a wide variety of parameters that are adjusted according to our interest and the properties that we want to preserve for the system. It is convenient to define the functional (Equation 2.81) as a generalized form [31].

$$E_{XC}^{GGA}[n_\uparrow, n_\downarrow] = \int d\vec{r} n \varepsilon_x(n) F_{XC}(n_\uparrow, n_\downarrow, |\nabla n_\uparrow|, |\nabla n_\downarrow|, \cdots) \tag{2.85}$$

2.3.3.4 Meta-GGA

The meta-GGA approximation consider kinetic energy of density as another parameter. Although GGAs and meta-GGAs add more physical information into the density-functional approximation, they are constructed to maintain the accuracy for the E_{XC} [38].

The functionals for the third rung of Jacob's ladder (Figure 2.4) are given as:

$$E_{XC}^{MGGA}[n_\uparrow, n_\downarrow] = \int d\vec{r} n \varepsilon_{xc}(n_\uparrow, n_\downarrow, \nabla n_\uparrow, \nabla n_\downarrow, \tau_\uparrow, \tau_\downarrow) \tag{2.86}$$

where $n(\vec{r}) = n_\uparrow(\vec{r}) + n_\downarrow(\vec{r})$ is the total density, and $\tau(\vec{r})$ is the kinetic energy density for the occupied Kohn-Sham orbitals $\phi_i(\vec{r})$ 2.68)[36] [39].

$$\tau(\vec{r}) = \sum_i \frac{1}{2} |\nabla \phi_i(\vec{r})|^2 \tag{2.87}$$

In Equation 2.86 we can verify that Meta-GGA contains information of the previous rungs but add another local variable, the kinetic energy density, τ.

2.3.3.5 Hybrid Functionals

In this rung, we have the combination of the HF Approximation (see subsection 2.1.3) and DFT. HF theory gives an exact version of exchange energy, which is quantum effect owing to the Pauli exclusion principle. For paired electrons as the case of electrons in $3d$ orbital of Mn atom, this effect is relevant. Although hybrid functionals take account new effects, unfortunately it depicts deficiencies in describing chemical bonding [40].

For DFT, we have the Kohn-Sham equations where the unique term to approximate is the exchange-correlation energy, E_{XC}. Therefore, it makes sense that if we want to combine H-F theory with DFT, we need to focus our attention on this term.

There exists a rigorous *ab initio* formula for the exchange-correlation energy E_{XC} of Kohn-Sham density functional theory known as the "adiabatic formula" [40] given as:

$$E_{XC} = \int_0^1 U_{XC}^{\lambda} d\lambda \tag{2.88}$$

where λ is an interelectronic coupling-strength parameter and U_{XC}^{λ} is the potential energy of exchange correlation. Equation 2.88 literally connects the non-interacting Kohn-Sham reference system ($\lambda = 0$) to the fully-interacting real system ($\lambda = 1$) [40]. The total energy difference between the fully-interacting and the non-interacting cases is related to λ [41].

The *ab initio* calculation of E_{XC} employing Equation 2.88 is very difficult. For solving the equation, a linear approximation is used:

$$E_{XC} \backsimeq \frac{1}{2} U_{XC}^{0} + \frac{1}{2} U_{XC}^{1} \tag{2.89}$$

The term U_{XC}^{0} is the exchange and electron correlation potential of non-interacting system, meanwhile U_{XC}^{1} is the exchange and electron correlation potential of the interacting real system. We note that U_{XC}^{0} is just the Kohn-Sham exchange energy E_X meanwhile the second term is defined as:

$$U_{XC}^{1} \backsimeq U_{XC}^{LSDA} = \int u_{XC}[n_{\uparrow}, n_{\downarrow}] d\vec{r} \tag{2.90}$$

where $u_{XC}[n_{\uparrow}, n_{\downarrow}]$ is the exchange-correlation potential-energy density of a spin-polarized electron gas. The explicit shape of u_{XC} for electron gas was given by Perdew and Wang [42].

Another reason why U_{XC}^{0} is practically the exchange energy E_X, is because this term is by far the dominant component of the E_{XC}. Rewriting the Equation 2.89, we have:

$$E_{XC} \backsimeq \frac{1}{2} E_X + \frac{1}{2} U_{XC}^{LSDA} \tag{2.91}$$

Now, we are in position to write an expression for the exchange energy, E_X. It can be computed exactly, employing the definition of exchange energy (Equation 2.29) in HF theory but using Kohn-Sham occupied orbitals, ϕ_i [40] [43].

$$E_X = -\frac{1}{2} \sum_{ij} \int \int d\boldsymbol{r_1} d\boldsymbol{r_2} \phi_i^*(\boldsymbol{r_1}) \phi_j(\boldsymbol{r_1}) \frac{1}{|\boldsymbol{r_1} - \boldsymbol{r_2}|} \phi_j^*(\boldsymbol{r_2}) \phi_i(\boldsymbol{r_2}) \tag{2.92}$$

Equation 2.91 is very simple and implies many approximations. It may be useful, therefore, to generalize as follows:

$$E_{XC} \backsimeq c_0 E_X + c_1 U_{XC}^{LSDA} \tag{2.93}$$

with c_0 and c_1 as parameters to be determined by appropriate fits to experimental data [40]. The following are some examples of hybrid functionals that we employ in this work:

$$E_{XC}^{B3LYP} = 0.20 E_X^{H-F} + 0.72 E_X^{B88(GGA)} + 0.08 E_X^{LSDA} + 0.81 E_C^{LYP(GGA)} + 0.19 E_C^{LSDA} \tag{2.94}$$

$$E_{XC}^{PBE0} = 0.25 E_X^{H-F} + 0.75 E_X^{PBE(GGA)} + E_C^{PBE(GGA)} \tag{2.95}$$

Becke's three-parameter functional (B3LYP), which is one of the most famous hybrid functionals [43].

$$E_{XC}^{B2PLYP} = 0.53E_X^{H-F} + 0.47E_X^{B88(GGA)} + 0.73E_C^{LYP(GGA)} + 0.27E_C^{MP2} \tag{2.96}$$

As we can see, the key idea of hybrid functionals is combining DFT and HF exchange terms, and correlation terms from different functionals that have been developed.

2.3.3.6 Range-Separated Hybrid Functional (RSH)

This is a subgroup of hybrid functionals, where the Coulomb interaction term $1/\vec{r}_{12}$ ($\vec{r}_{12}$ being the inter-electronic distance) receives special treatment. Instead of just certain weights for the contribution of E_X^{H-F} and E_X^{DFT}, RSH employs a function ($\omega_{RSF} \equiv \omega_{RSF(\gamma,\vec{r}_{12})}$) to connect both contributions. In the long distance limit, exchange potential of hybrid functionals deviates from its correct ($1/\vec{r}_{12}$) form. For recovering the behavior in some way, the Coulomb interaction is split into two parts: short-range (SR) component treated by DFT, and a long range (LR) component treated by Hartree-Fock [44].

$$\frac{1}{\vec{r}_{12}} = \frac{1 - [\alpha + \beta(1 - \omega_{RSF})]}{\vec{r}_{12}} + \frac{\alpha + \beta(1 - \omega_{RSF})}{\vec{r}_{12}} \tag{2.97}$$

The first term on the left is called Short-Range and the second term is the Long-Range. The function ω_{RSF} could be the complementary error function $erfc(\gamma\vec{r}_{12})$, or the Slater function $e^{-\gamma\vec{r}_{12}}$. In summary RSH, is an improvement of the hybrid functionals and most of the cases are treated as a subgroup of it. In this work wB97M-V is the RSH functional that we are going to implement to study Mn clusters.

Chapter 3

Computational Methods

Density functional theories (DFTs) are very successful techniques for understanding the electronic, structural and vibrational properties of large molecules systems [45]. During these years have been developed many computational packages which implement DFT such as *Gaussian* 98, $ORCA$, $Q-chem$, $SIESTA$, $VASP$, $UTEP-NRLMOL$ and others. In this chapter, we will give some details about each of the computational packages that we employ for this research project.

3.1 The Vienna *ab initio* Simulation Package, VASP

The Vienna *ab initio* Simulation Package (VASP) is an efficient DFT code for studying 3D bulk systems with periodic boundary condition [45]. VASP was developed with the aim of bringing an efficient solution for many computational problems that DFT presents, for instance: (a) calculating the electronic ground-state (b) describing the electron-ion interaction by ultrasoft pseudo-potentials [46] (c) estimating the ground state easily using iterative diagonalization of K-S Hamiltonian [45] [46].

Besides the pseudo-potentials, similar to other packages, VASP employs plane waves (PWs) as one of its basis sets. At the beginning VASP was based on DFT completely, but the current version of the code includes the post-DFT corrections, for instance hybrid functionals.

3.1.1 VASP, basic methodology

3.1.1.1 Supercell approximation

One of the highlight features of VASP is the implementation of supercell approximation. The objective with the supercell is to have a large periodic cell that its local behavior can be repeated many times until cover well our system [47].

In case of VASP which was designed to study crystals the supercell approximation is useful. For studying isolated systems it is important to consider some details like the distance between the systems in each supercell to neglect the interaction between molecules or clusters. For example, if our system has three atoms or particles as seen in Figure 3.1, due to periodic boundary conditions there are several iterations of the initial system.

For this project we study isolated manganese clusters, which means that there is no interplay between each cluster (Figure 3.1 ***b***)) in each supercell. For avoiding the interactions, we try to keep a distance of 12 Å between each cluster as a suggestion from other researchers [48].

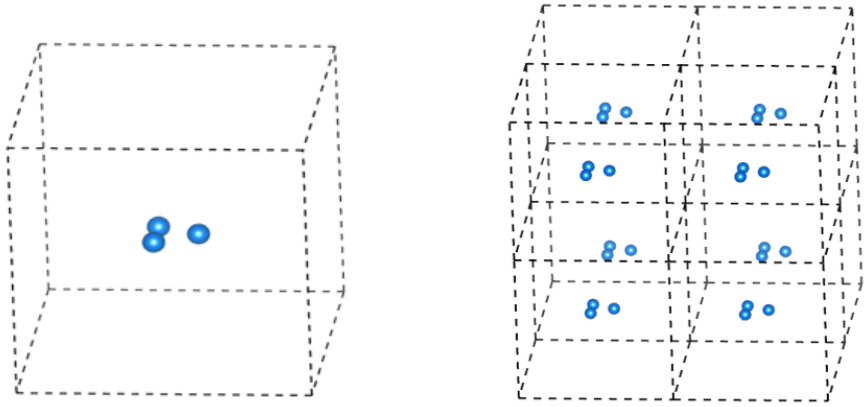

(a) (b)

Figure 3.1: ***a)*** Supercell ***b)*** periodicity of the system with supercell approximation.

3.1.1.2 Plane Waves, PWs

For solving the one-electron Kohn-Sham Equations (2.65), VASP employs a Hamiltonian method that relies on a diagonalization of the Hamiltonian [6]. This method utilizes an expansion of the Kohn-Sham orbitals $\phi_i(\vec{r})$ into some kind of basis, given as:

$$\phi_i = \sum_k C_k^i \xi_k \tag{3.1}$$

where ξ_k are the basis functions and C_k^i are the expansion coefficients for the electron i.

Since VASP originally deals with crystals employing the supercell approximation, the potential has the periodicity of the supercell. Let's define:

$$V(\vec{r} + \vec{R}) = V(\vec{r}) \tag{3.2}$$

with $\vec{R}$ as the translational lattice vectors. For the present work, the supercell approximation allows us to simulate the cluster like a crystal. For solving the Kohn-Sham Equations in VASP code, we have the plane waves as a basis set. Thus, Kohn-Sham orbitals are expressed as:

$$\phi_i \vec{k}(\vec{r}) = U_{i\vec{k}}(\vec{r}) e^{j\vec{k}.\vec{r}} \tag{3.3}$$

with $\vec{k}$ as the wave number and $U_{i\vec{k}}(\vec{r})$ is a function with the periodicity of the crystal. The above expression is a direct consequence of Bloch's Theorem. The periodic functions can be expanded using planes waves in the reciprocal lattice with $\vec{G}$ as the wave number:

$$U_{i\vec{k}}(\vec{r}) = \sum_{\vec{G}} C_{i\vec{k},\vec{G}} e^{j\vec{G}.\vec{r}} \tag{3.4}$$

As we mentioned, the periodic function has the periodicity of the lattice, $U_{i\vec{k}}(\vec{r} + \vec{R}) = U_{i\vec{k}}(\vec{r})$

$$U_{i\vec{k}}(\vec{r} + \vec{R}) = \sum_{\vec{G}} C_{i\vec{k},\vec{G}} e^{j\vec{G}.(\vec{r}+\vec{R})} = \sum_{\vec{G}} C_{i\vec{k},\vec{G}} e^{j\vec{G}.\vec{r}} \tag{3.5}$$

$$e^{j\vec{G}.\vec{R}} = 1 \tag{3.6}$$

For the above expression, mean that $\vec{G} \cdot \vec{R} = 2\pi * m$ with m as an integer number. Now we are in position to rewrite the Kohn-Sham orbitals:

$$\phi_i\vec{k}(\vec{r}) = \sum_{\vec{G}} C_{i\vec{k},\vec{G}} e^{j\vec{G}.\vec{r}} e^{j\vec{k}.\vec{r}} = \sum_{\vec{G}} C_{i,\vec{G}+\vec{k}} e^{j(\vec{G}+\vec{k}).\vec{r}} \tag{3.7}$$

$C_{i,\vec{G}+\vec{k}}$ are the plane wave coefficients for the electron i. There is a truncation of plane wave expansion, where only the reciprocal lattice vectors whose kinetic energy lower than a defined cut-off energy are took account.

$$\frac{1}{2}|\vec{G}+\vec{k}|^2 < E_{cut} \tag{3.8}$$

The use of a plane wave basis set has several advantages such as: (i) it is easy to change from a real-space representation via a Fast Fourier Transform to momentum-space. (ii) The control of basis set convergence is pretty easy. We can control the number of plane waves whose energy is less than the cut-off energy. (iii) The Hellmann-Feynman forces between atoms in the supercell may be computed in terms of the expectation value of the Hamiltonian with respect to certain ionic coordinates [7].

Is important to highlight that plane wave basis sets are somewhat unusual for molecular applications, because of the associations of plane wave basis sets with free electron like systems [45]. As we are going to see in the following pages, Gaussian functions are the other alternative as a basis set. Gruber *et al.* [49] in its work studied the performance of the plane waves and localized basis sets (Gaussian functions) for small gold clusters. They showed a slightly difference for the binding energy which also is related with the structure of the group of atoms.

3.1.1.3 Projector Augmented Waves, PAWs

The wave function of electrons have different behavior depending its location. For example, electrons' wave function in bonding region is smooth, whereas close to the nucleus it oscillates rapidly. The wave function behavior near nucleus is owing to the large attractive potential of the nucleus [50][51], as is shown in Figure 3.2. The strategy behind PAWs method is the concept of an augmentation region, $\Omega_{\boldsymbol{A}}$. Therefore in 3D there is a sphere around each atom of our system. Inside the sphere instead of using wave functions with rapid oscillation we use a smooth wave function called pseudo wave function [6] [7] [50].

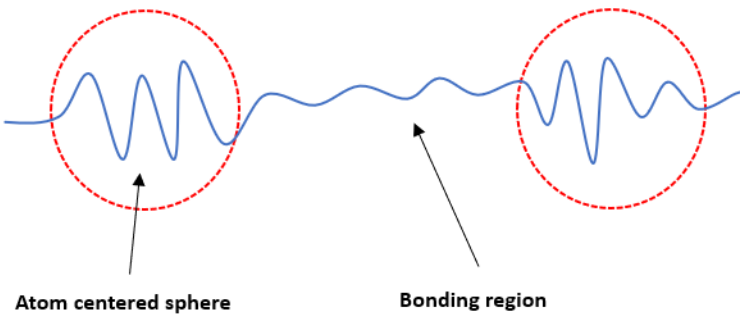

Figure 3.2: Illustration of how wave function of valence electrons oscillate rapidly near atomic cores. The effect is owing to the strong interaction with wave function of core electrons. Wave function in bonding region is smooth.

The PAW method accounts for the nodal features of the valence orbitals and ensures orthogonality between valence and core wave functions [7]. The PAW method utilizes a transformation $\boldsymbol{T}$, of the valence wave functions ϕ (Kohn-Sham orbitals) onto fictitious pseudo wave functions $\tilde{\phi}$ according with the following expression.

$$|\phi\rangle = \boldsymbol{T}|\tilde{\phi}\rangle \tag{3.9}$$

For the above expression, the total energy will be evaluated as fucntion of pseudo-functions.

$$\boldsymbol{T}^* H_{KS} \boldsymbol{T}|\tilde{\phi}\rangle = \epsilon \boldsymbol{T}^* \boldsymbol{T}|\tilde{\phi}\rangle \tag{3.10}$$

Where H_{KS} is the Hamiltonian that appear in the Kohn-Sham equation with eigenvalue ϵ. The transformation $\boldsymbol{T}$ is given as:

$$\boldsymbol{T} = \mathbf{1} + \sum_{\boldsymbol{A}} \tilde{\boldsymbol{T}}_{\boldsymbol{A}} \tag{3.11}$$

where each local contribution $\tilde{\boldsymbol{T}}_{\boldsymbol{A}}$ acts only within augmentation region $\Omega_{\boldsymbol{A}}$ enclosing the atom $\boldsymbol{A}$, indicated by red circle in Figure 3.2 [6]. With this, we have that the wave functions ϕ and $\tilde{\phi}$ match outside or at the surface of the augmentation region, as can be appreciate in the following equation:

$$|\phi_i\rangle = (\mathbf{1} + \tilde{\boldsymbol{T}}_{\boldsymbol{A}})|\tilde{\phi}_i\rangle \tag{3.12}$$

Regarding the pseudo wave function $\tilde{\phi}$, it can be expressed in the following way:

$$|\tilde{\phi}\rangle = \sum_i |\tilde{\varphi}_i\rangle c_i \tag{3.13}$$

within the augmentation region $\Omega_{\boldsymbol{A}}$ and $\tilde{\varphi}_i$ are the partial wave functions multiplied by the constants c_i. So that, the constants are computed:

$$c_i = \langle \tilde{p}_i | \tilde{\varphi} \rangle \tag{3.14}$$

where $\langle \tilde{p}_i|$ is the projector function. Within the augmentation region $\Omega_{\boldsymbol{A}}$, the projector function fulfills the condition $|\tilde{\varphi}_i\rangle\langle\tilde{p}_j| = \delta_{ij}$ with the partial waves $\tilde{\varphi}$. Rewriting Equations 3.11 and 3.9 in terms of the projector function, the total electron density is given as:

$$n(\vec{r}) = \tilde{n}(\vec{r}) + n_1(\vec{r}) + \tilde{n}_1(\vec{r}) \tag{3.15}$$

The first term refers to the density using the pseudo wave functions $\tilde{\phi}$, meanwhile the last two terms are computing within the augmentation region $\Omega_{\boldsymbol{A}}$. The two last terms depend on the Kohn-Sham orbitals ϕ (valence wave function) and on the pseudo partial waves $\tilde{\varphi}$ [6] [7] [50].

3.1.2 Charge density partition methods

In the moment when we try to solve the Schrödinger equation for many particles (Equation 2.1), the wave function describes the total system and not each atom separately. The transfer of charges between atoms, the presence of ionic charges on atoms or molecules and even the local magnetic moment distribution in clusters due to the magnetization is very sensitive to changes in the local environment. Studying these processes are important to understand certain chemical and physical properties [52] [53].

Atomic charges in molecules are not observables, hence not defined by quantum mechanical theory. Quantum mechanics calculations yield a continuous electronic charge density and the problem is how to make the partitions between the atoms or molecules of our system [52]. Fortunately for us, there are some methods that can be used to estimate the electronic charge density and the local magnetic moment for each atom.

3.1.2.1 Wigner-Seitz sphere

This is the simplest method that VASP uses by default and it refers to the case in which for each atom there is a sphere with the same radius that cannot overlap each other. This method is useful when we have certain symmetry in the structure and the same type of atoms. The inaccuracies come around when the locations of the atoms aren't regular, where the local magnetic moment and charge can change for each atom.

3.1.2.2 Bader charge analysis

This approach focuses entirely on the charge density and space is then divided into regions that contain one nucleus but this requirement isn't necessary. At a point on a dividing surface, the gradient for the electron density has no component normal to the surface and it means that gradient of charge density is zero [3] [52].

Shown in Figure 3.3 are unit vectors normal to the surfaces denoted by $\vec{n}$. If the scalar product $\nabla\rho \cdot \vec{n}$ vanishes then $\nabla\rho$ has no component through the surface. Let's see the previous condition isn't satisfied

by the surface ***a)*** in Figure 3.3 but is satisfied by the surface ***b)*** [3]. The path indicated by ***b)*** is called the Bader region.

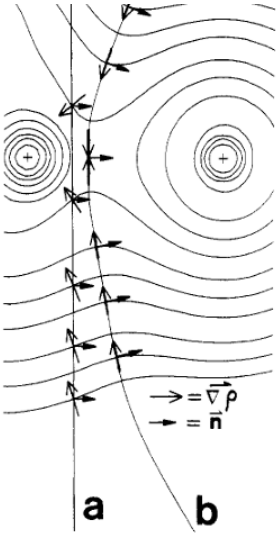

Figure 3.3: A portion of a contour map of a charge distribution showing intersection with two partitioning surfaces [3].

3.1.2.3 Voronoi Deformation Density (VDD)

The VDD method computed the amount of electronic density that flows from or to a certain atom owing to the bonding formation by spatial integration of the deformation density $\rho_{def}(r) = \rho(r) - \rho_{promolecule}(r)$ over the atomic Voronoi Cell (VC) [54].

The VDD atomic charge Q_A^{VDD} of the atom A in volume element $d\vec{r}$ is given as:

$$Q_A^{VDD} = -\int_{VC} [\rho(\vec{r}) - \rho_{promolecule}(\vec{r})] d\vec{r} \tag{3.16}$$

The fictitious promolecule is a superposition of atomic ground-state densities[54]:

$$\rho_{promolecule}(\vec{r}) = \sum_B \rho_B(\vec{r}) \tag{3.17}$$

With VDD method, for each atom the space splits in many regions called Voronoi cells, which are defined to be part of space closer to the nucleus of that atom [54]. The following are the steps to construct the Voronoi cell or polygon (Figure 3.4): (i) connecting the centers of atoms. (ii) Draw the perpendicular bisectors of these centers. We see an area enclosed by intersection lines with each atom of the system in the center. All points inside the cell are closer to the center of the "central" atom [4]. For Voronoi cell in 3D, atoms or ions occupies a volume, and Equation 3.16 is integrated over this volume.

For the analysis of the Local Magnetic Moment (LMM) obtained from our DFT calculations, this method is used. As we will see later, the structure of the clusters presents a certain asymmetry, so the distance between manganese atoms won't be the same. Thus the values of the LMM are expected to be different and this method will give us a good estimation about it.

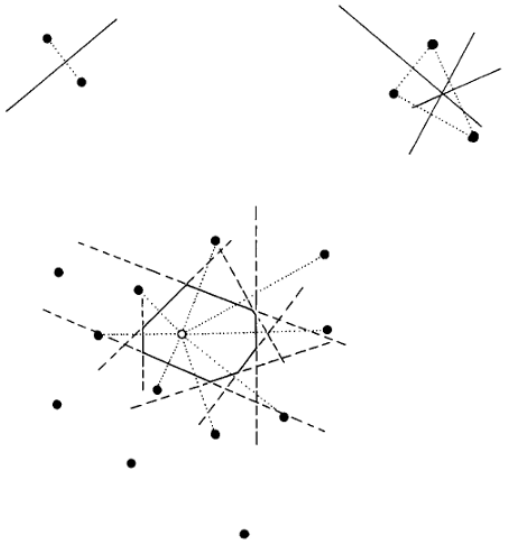

Figure 3.4: Two-dimensional construction of Voronoi cell [4]

3.1.3 Computational details for VASP implementation

All the calculations performed with VASP code for the simulation of Mn clusters comply with certain computational details. As we have mentioned, the code employs plane waves as a basis set and the cut-off energy is $E_{cut} = 500\ eV$ (Equation 3.8).

The Mn atoms are located in supercell (Figure 3.1) taking care that the distance between clusters owing periodicity is roughly 12 Å. Regarding the dimension of a supercell, this might be different for each cluster size. For instance, for the dimer (Mn_2), each side of the supercell is 14 Å. For Mn_3 the sides were 14 Å, 14 Å and 15 Å. So, depending in the quantity of atoms, we could increase the size of supercell.

For solving the Kohn-Sham Equations 2.65 in a system of N electrons, the maximum number of electronic Self-Consistency (SC) step is 200 although it can also change. This means that the maximum number to compute the charge density $n(\vec{r})$ (Equation 2.68) is 200 in each ionic step. After computing the Kohn-Sham orbital for the N electrons, density is calculated and compared with the previous one. If the energy difference is less than $1 \times 10^{-5}\ eV$ we have energetic convergence and the SC-loop is interrupted to move to the next ionic step. If the density does not converge, we use the ending value as a guess for the next electronic SC until it converges.

In each ionic step (where the positions of the nuclei change) the structure is relaxed using the conjugate gradient method. Previous moving to next ionic step, forces on each atom are computed. The maximum number of ionic steps varies between 100-250, which depend in the cluster size and until achieve energy minimization. If the total force on atoms (Feynman-Hellman forces) is less than $-1 \times 10^{-3}\ eV/$Å it means that the optimal structure has been achieved. With the previous, we have that the initial structure of the Mn cluster might change owing to the ionic steps.

3.2 ORCA Package

Orca is one of the most popular quantum chemistry packages that implement DFT. The package is useful to study the electronic structure of a cluster of atoms. In this subsection we are going to give some features about this computational package.

3.2.1 ORCA, basic methodology

3.2.1.1 Slater Type Orbitals, STOs

Slater Type Orbitals are considered as natural basis functions in quantum molecular calculations. This type of orbitals is also called as hydrogen-like because its radial part decays with distance r and its

angular part is described by spherical harmonics, $Y_l^m(\theta, \varphi)$.

$$\Phi(r) = Cr^{n-1}e^{-\zeta * r}Y_l^m(\theta, \varphi) \tag{3.18}$$

where C is a normalization constant, ζ is a constant depending on the effective charge of the nucleus, l is the azimuthal quantum number, n is the principal quantum number, and m is the magnetic quantum number.

3.2.1.2 Triple$-\zeta$ basis set

The ORCA code handles different basis sets such as Gaussian Type Orbitals (GTOs) and STOs. In general GTOs and STOs are localized orbitals, which means they model very well the behavior of atomic orbitals near atomic nuclei. In our case, we work with a linear combination of STOs called triple-zeta or triple$-\zeta$ basis set.

The expansion of Kohn-Sham orbitals in this basis is given as:

$$\phi_{knlm}(\vec{r} - \vec{R}_k) = a_1\Phi(r - R_k, \zeta_1) + a_2\Phi(r - R_k, \zeta_2) + a_3\Phi(r - R_k, \zeta_3) \tag{3.19}$$

Where $\vec{R}_k$ is the position of the nuclei atomic k. This type of basis set is very popular in quantum chemistry due to its accurate results for computing bond length and bonding energy. A triple$-\zeta$ basis, besides its localization also offers some computational advantages, including large reduction of CPU time and high accuracy of calculations. Due to its dependence on the position of the nuclei $\vec{R}_k$ it gives rise to an error called Pulay stress, which affects the ground state energy of the system.

The exact solution for the Schrodinger Equation applied to the hydrogen atom is STOs of the $e^{-\alpha r}$ shape [5]. In an attempt to solve the problem, it is common to employ Gaussian functions with different parameters or magnitude, as seen in Figure 3.5. Thus, develop a linear combination of GTOs, known as linear combination of atomic orbitals (LCAOs) [49]. As we can see, there are many alternatives to expand the Kohn-Sham orbitals and some are more complex than others.

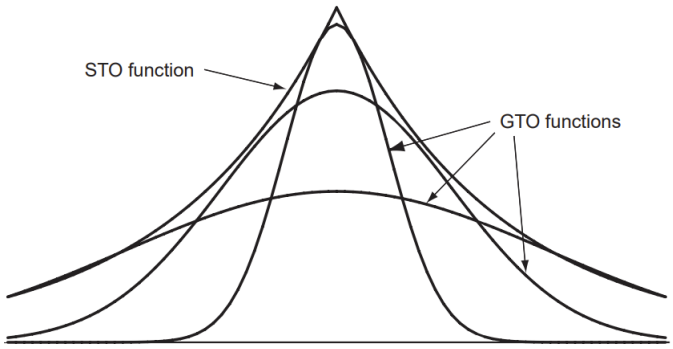

Figure 3.5: Approximating a STOs with several GTOs [5].

3.2.1.3 Pseudo-potentials

It is important to highlight that pseudo-potentials (V^{PS}) are not exclusive to the ORCA code, other codes also use them. These are very important to streamline computation time because they are used to avoid the need for an explicit treatment of the strongly bound and chemically inert core electrons [45] [55]. Thus, pseudo-potentials take account of only the valence electrons, which participate in bonding. Today, with supercomputers and advantage in employing the effective potentials is that these include other effects in the calculations, including relativistic effects e[55].

Pseud-potentials are an additional approximation that can be made on the electronic Hamiltonian, H_{ele}. Rearranging a bit the terms of Equation 2.6, we have:

$$H_{ele} = \sum_{i=1}^{N} \left(-\frac{1}{2}\nabla_i^2 - \sum_{A=1}^{L} \frac{Z_A}{\vec{r}_{iA}} \right) + \frac{1}{2} \sum_{i=1}^{N} \sum_{j>i}^{N} \frac{1}{\vec{r}_{ij}} \tag{3.20}$$

Considering just the valence electrons of the atoms, the Hamiltonian is given as:

$$H_{ele}^{PS} = \sum_{i=1}^{n_v} \left(-\frac{1}{2}\nabla_i^2 - \sum_{A=1}^{L} V_A^{PS} \right) + \frac{1}{2} \sum_{i=1}^{n_v} \sum_{j>i}^{n_v} \frac{1}{\vec{r}_{ij}} \tag{3.21}$$

Where n_v are the valence electrons and V_A^{PS} is the potential or effective potential due to the frozen core which includes the nucleus and the inner electrons of atom $\boldsymbol{A}$.

$$V^{PS} = \frac{Z}{r} - \sum_{l} V_l(r) P_l \tag{3.22}$$

In the above equation, P_l is the projector operator. Thus V^{PS} can be projected on any basis including triple$-\zeta$.

As it depicted in Figure 3.6, the valence wave functions oscillate rapidly in the region close to the core. These oscillations are a consequence of Heisenberg Uncertainly Principle for position-momentum, $[\hat{x}, \hat{p}] \geq \hbar/2$. Close to the nucleus the position is better know, so the uncertainty has to be in the momentum (related to wavelength and with frequency), which imply rapid oscillations. Another standpoint of view is that the valence wave functions has to be perpendicular to the core wave functions, as a consequence of Pauli exclusion principle [6].

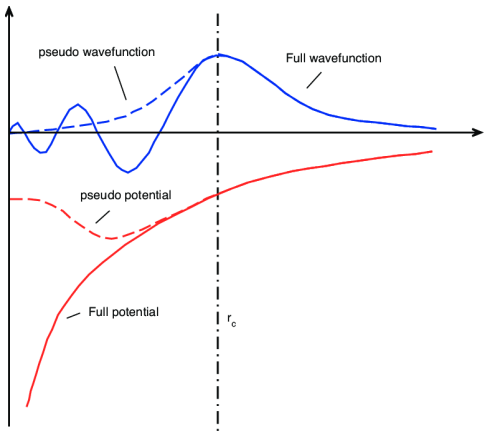

Figure 3.6: Illustration of the concept behind the pseudo-potential [6].

In Figure 3.6 we appreciate that the pseudo-potentials are smooth, because these are constructed with the objective to employ a small number of basis functions.

Chapter 4

Results

In this chapter, we present the main results in the study of manganese clusters (Mn_α, $\alpha = 2, \cdots, 7$), using different functionals. The calculations are performed under two implementations of DFT. The first implementation is with plane waves basis in VASP code (see subsection 3.1) and the second is with localized molecular orbitals (triple$-\zeta$ basis) in ORCA code (see subsection 3.2). On the following pages for each cluster, we will provide information about: bond lengths, bonding energy, ground magnetic state, degenerate states, ferromagnetic (FM) or antiferromagnetic (AF) ordering, local magnetic moment, density of states, and other properties. In addition, the comparison of results with experimental measurements and other studies carried out by other researchers is shown.

4.1 Manganese dimer, Mn_2

Mn_2 is the simplest case of Mn clusters and for this reason it represents a good test system to prove several theoretical methods because its properties are well known. Then these methods can be employed to study more complex systems [17].

For studying Mn_2, we use different type of functionals like: LSDA, GGA (e.g. PBE), meta-GGA (e.g., SCAN, rev-SCAN, rev-TPSS, and SCAN2), hybrid functionals (e.g., B3LYP, wB97M-V, PBE0, B2PLYP), and DFT+U. Each one of these functionals take account of different features of the system including variations of electronic density, correlation, correlation-exchange energy, gradient of density, and others.

We start the discussion about our results with functionals implemented in VASP code, which works with the plane waves basis. In Figure 4.1, for each functional, we approximate the variation of system's energy with distance. In addition, the ground state for each functional appears in the same figure, which will be ferromagnetic ($\mu = 10\ \mu_B$) or antiferromagnetic ($\mu = 0\ \mu_B$) ordering.

According to the experimental measurements (Table 1), the ground magnetic state for Mn_2 is AF with a net spin 0 μ_B, bonding energy of 0.13 $eV \pm 0.10\ eV$ and bond length ranges between 3.2 Å$-$ 3.4 Å [15] [17] [56]. In the following paragraphs we will discuss our results and the reason why one state is more stable than another.

The LSDA functional is the simplest kind of functional in Jacob's ladder (see subsection 2.73). Seeing Figure 4.1 and Table 4.2 we notice that the results completely disagree with experimental values, because we obtained FM ordering as the most stable. Here we notice that our system needs to be described by functionals which take account variations in electron density. The electronic configuration of the Mn atom is $[Ar]3d^5 4s^2$, where $3d$ is localized, and $4s$ is delocalized orbital, so that density is not the same everywhere. Another important detail, which will be useful for coming Mn clusters is that VASP employs PAW method (see subsection 3.1.1.3) and electrons in $4s$, and $3d$ orbitals are treated as valence electrons. As we will see, many properties will be explained based on the behavior of these orbitals.

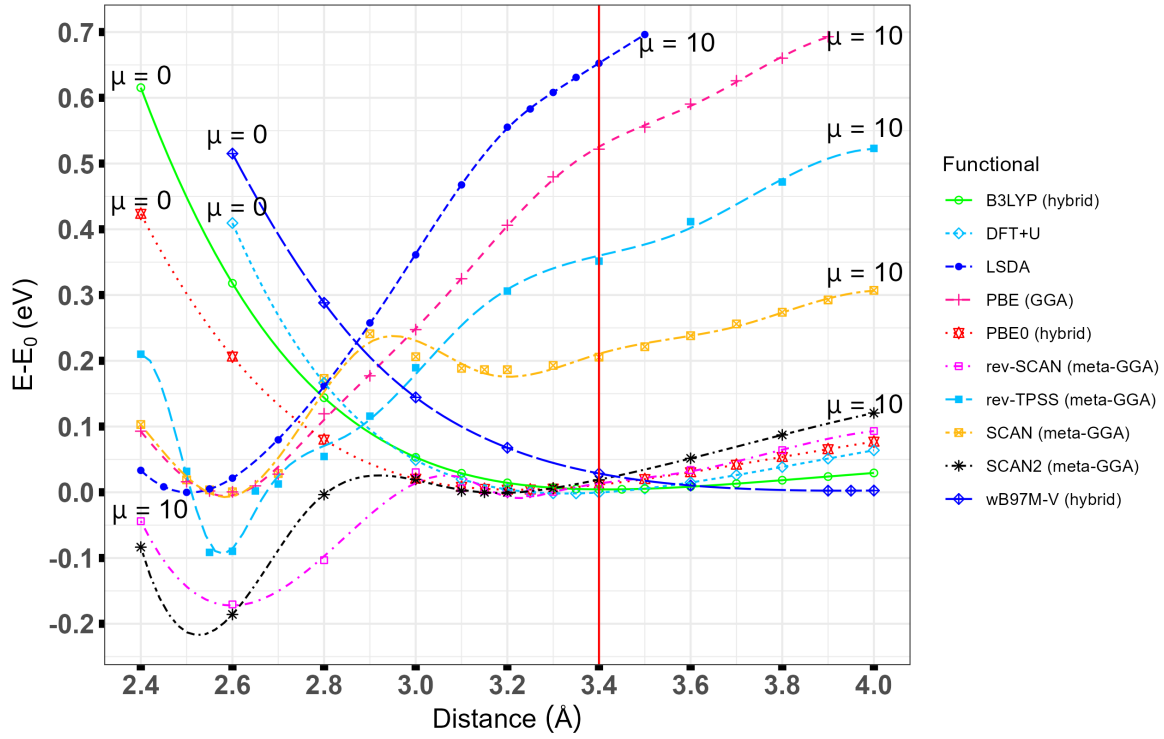

Figure 4.1: Variation of energy of Mn_2 as a function of distance in the plane waves basis set. The red vertical line presents the experimental bond length (3.41 Å) when Mn_2 reaches an equilibrium structure. For this cluster, AF ordering refers to the net magnetic moment 0 μ_B and FM for 10 μ_B.

Analyzing LSDA's density of states (DOS), in Figure 4.2 ***a)*** we see contributions of $4s$ and $3d$ orbitals to the magnetic moment. Also we see the hybridization of $s-d$ orbitals close to the Fermi energy and around -2.25 eV. On the other hand, in Figure 4.3 ***a)*** we have the Crystal Orbital Hamilton Populations (COHP) analysis, where the states close to the Fermi energy are antibonding. For AF ordering, Figure 4.2 ***b)*** we have much $3d$ states close to the Fermi energy. Thus, we see a strong hybridization between $d-d$ orbitals, which means that there is a strong repulsion (atoms are a bit more separated). As well, COHP analysis in Figure 4.3 ***b)*** shows that the states in Fermi energy are bonding, which means that it promotes the formation of the cluster. In general owing to the high exchange energy for d states, the system is more stable. Thus, FM is more stable than AF state according with LSDA. Additional thing, in isomer ***a)*** shows more hybridization owing to the short bond length (2.41 Å) between atoms compared with isomer ***b)*** for a bit large bond length (2.50 Å).

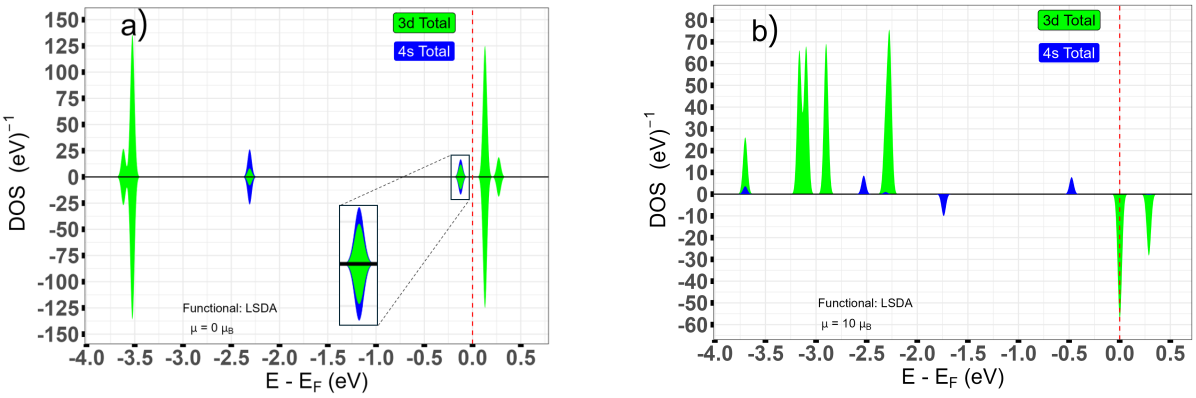

Figure 4.2: The Density of States (DOS) of Mn_2 for low energy states. The red dotted line presents the Fermi energy, E_F. States on the right side of E_F are unoccupied and on the left are occupied.

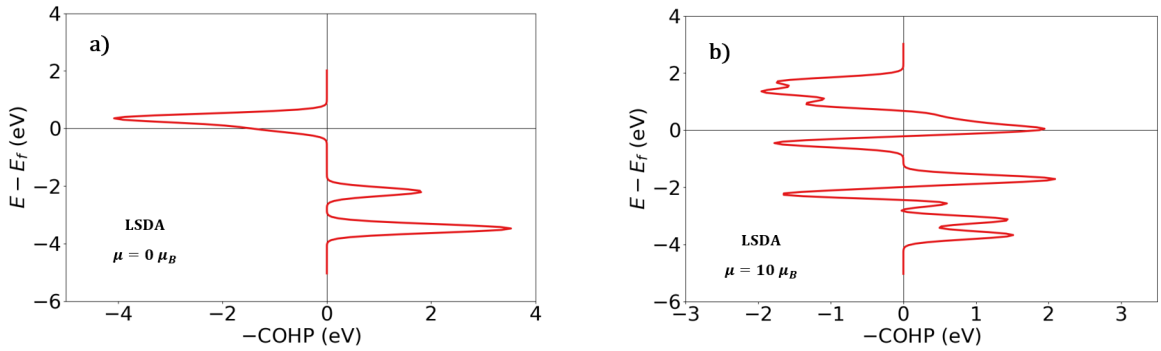

Figure 4.3: The Crystal Orbital Hamilton Populations (COHP) for Mn_2. The bonding orbitals are on the right side of each panel, meanwhile the antibonding are on the left side.

As with LSDA, the PBE functional also provides FM solution for the ground state with 10 μ_B as total magnetic moment and with 2.60 Å for the bond length. Other calculations performed by Bobadova-Parvanova *et al.* [57] obtained the same result with PBE but using NRLMOL code. This code works with all-electron Gaussian basis in contrast with the plane waves basis that VASP uses. Gaussian basis set is recognized as one of the best ways to describe the atomic orbitals. Thus, it make sense that the bonding energy (0.49 eV) reported by them is more accurate and closer to the experimental value than our result computed with Kohn-Sham orbitals expanded in the plane waves basis.

Now let's see DOS and COHP computed for PBE for low energy states. If we look carefully, Figure 4.4 is pretty similar to Figure 4.2 obtained with LSDA. So, it's a great opportunity to see the small differences between both functionals. For Figure 4.4 ***b)*** (FM ordering) there are a bit less $3d$ states close to the Fermi energy, as well there is a reduction of $d - d$ hybridization. In Table 4.1 we see the bonding energy is 0.95 eV which is less than obtained with LSDA. In the same way, the reduction of hybridization implies a weaker bonding and longer bond length (2.58 Å). For COHP analysis in Figure 4.5, for FM solution the states close to the Fermi energy are bonding while for AF solution these are antibonding. In general bonding orbitals mean more stability than antibonding. For isomer ***a)*** which is AF arrangement we see less spliting of d orbitals, because the distance between atoms is a bit large (2.64 Å) compared with isomer ***b)***. Therefore, for AF solution atomic orbitals are less overlapped.

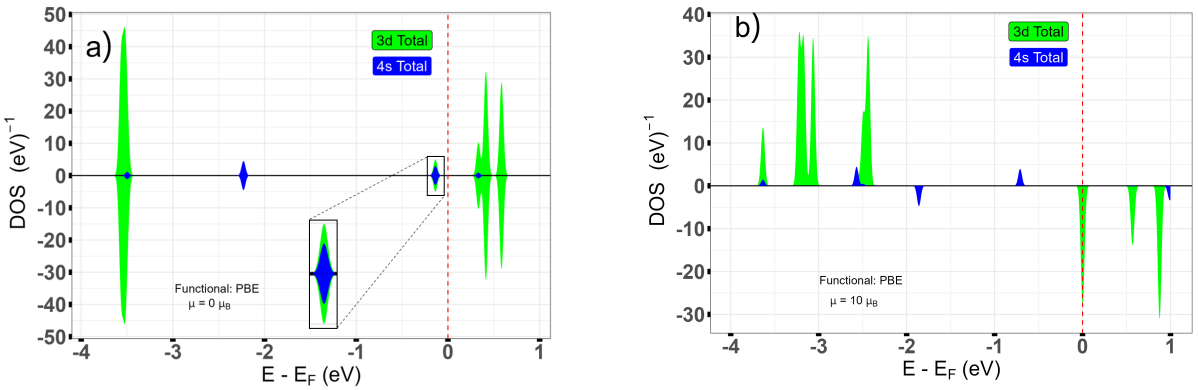

Figure 4.4: The Density of States (DOS) of Mn_2 for low energy states. The red dotted line presents the Fermi energy, E_F. States on the right side of E_F are unoccupied and on the left are occupied.

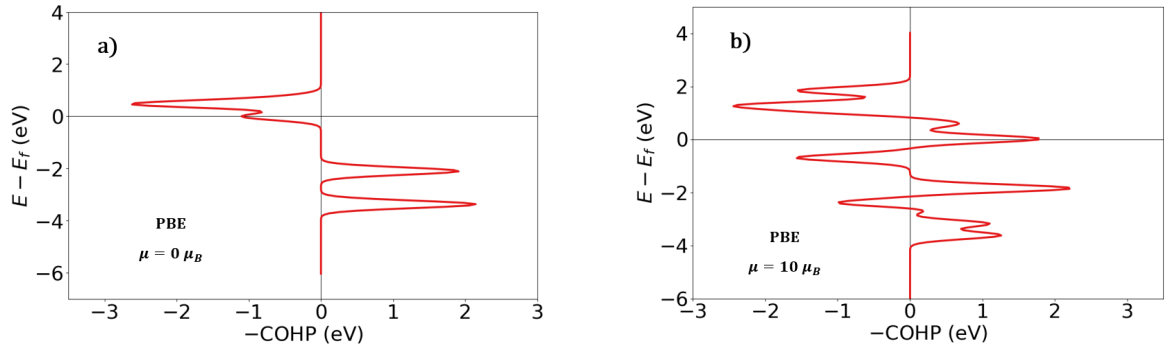

Figure 4.5: The Crystal Orbital Hamilton Populations (COHP) for Mn_2. The bonding orbitals are on the right side of each panel, meanwhile the antibonding are on the other side.

For meta-GGA functionals (see subsection 2.3.3.4), basically all of them yield FM as result for the ground state. Among this kind of functional, let's analyze rev-SCAN which is an improvement of SCAN where make a slight change in SCAN correlation [58]. In Table 4.3 we can see that the difference between AF and FM states is very small ($4.0 \times 10^{-4} eV$) and therefore they can be classified as degenerate states. As we see, the bond length 3.23 Å, and bonding energy 0.22 eV both range between the experimental values. This result tells us that electronic correlation plays an important role in our study and any change of this could trigger changes in system's properties.

As we already commented, Mn is a transition metal with electronic configuration $[Ar]4s^2 3d^5$, and according to Hund's Law, electrons in the $3d$ sub-shell are distributed in different orbitals with the same orientation of spin. Thus, the exchange energy is greater and the system is more stable. Besides, owing to the quantity of electrons in the same orbital it is evident that Coulomb repulsion (correlation) has an important role too. Therefore, the following rung of Jacobs' ladder will throw more light on the explanation of Mn_2 which takes account of the previous concepts.

Hybrid functionals (see subsection 2.3.3.5) are more complex functionals and give a special weight for the exact version of exchange energy from Hartree-Fock Approximation. For Mn_2, the hybrid functionals such as: B3LYP, PBE0 and wB97M-V, are the ones that best describe the behavior of Mn_2. For instance, all these functionals give AF ordering for the ground state with a total magnetic moment 0 μ_B, which is in line with the experimental value (Table 1) [15][16][18]. A research carried out by Yamanaka *et al.* [59] also found that HF plus DFT describes very well Mn_2 features.

Before starting with discussion about hybrid functionals in plane waves implementation, let's see an intrinsic error in DFT. In Kohn-Sham Equation (Equation 2.65) we have Hartree potential ($V_H(\vec{r})$) or the Coulomb interaction between an electron and the average charge of the all electrons in the system. The $V_H(\vec{r})$ considers self-interaction of electrons and this error overestimates artificially orbitals energy. For reducing self-interaction error (SIE) there are some methods like the exchange energy in Hartree-Fock Approximation. The exchange energy causes the electrons to separate by having the same spin orientation. Then, if electrons are separated, the interaction of an electron with itself is reduced although not eliminated.

For PBE0, Table 4.1 shows that the ground state is AF ordering with bond length 3.22 Å and bonding energy 0.18 eV. In Figure 4.6, for DOS analysis we see that for both AF and FM ordering there are several $4s$ states contributing to the magnetic moment. The $4s$ orbital is delocalized and favors antiferromagnetism because it can hold two electrons with opposite spin. Let's consider carefully each case. For AF, in Figure 4.6 ***a)*** we see that $4s$ states (the two peaks) with spin up (or spin down) are separated roughly 2 eV, meanwhile for FM ordering (Figure 4.6 ***b)***) they are separated roughly 1.5 eV. Thus, for FM in energy space the states are closer and the electrons with the same spin are much closer to each other and the system is more unstable (ease to pass from one state to other). If we compare panel ***a)***, and ***b)***, we see more $s - s$ hybridization in ***b)***, so the repulsion is higher (much unstable) than in ***a)***, which also implies a greater bond length (3.40 Å) in ***b)***. In Figure 4.7, for both panels we see that states close to the Fermi energy are antibonding. In general, in antibonding orbital the electrons are not in the middle of atoms and for that reason it favors larger bond lengths. Another important thing to highlight

here is that for both panels there aren't hybridization between $s-d$ orbitals close to the Fermi energy, which is a highlight difference regarding LSDA and PBE. From what has been discussed, it is clear why ***a)*** is more stable.

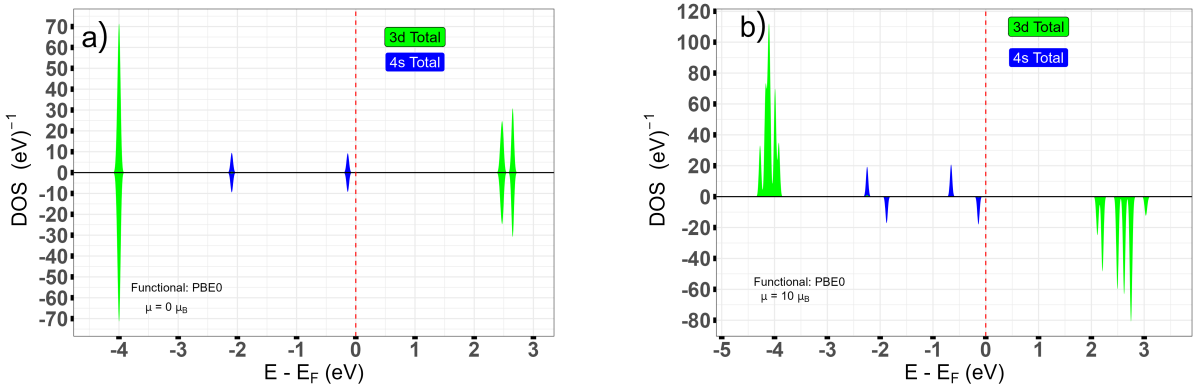

Figure 4.6: The Density of States (DOS) of Mn_2 for low energy states. The red dotted line presents the Fermi energy, E_F. States on the right side of E_F are unoccupied and on the left are occupied.

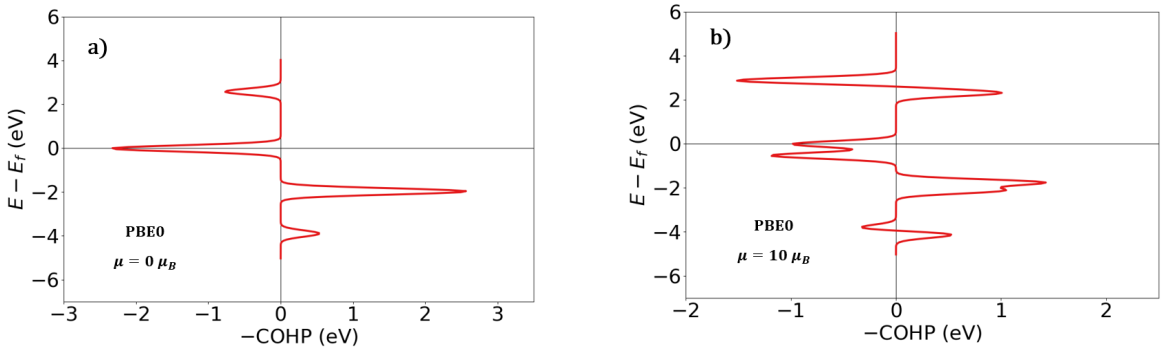

Figure 4.7: The Crystal Orbital Hamilton Populations (COHP) for Mn_2. The bonding orbitals are on the right side of each panel, meanwhile the antibonding are on the other side.

Among the hybrid functionals, DFT+U is a bit of a special case. For this functional, the Hubbard term (U) is included to strengthen electron correlation instead of exchange energy. This type of functional was studied by Huang *et al.* [21] too, employing GGA functionals (e.g. PBE, and PW91) performed in Quantum-ESPRESSO (QE) code. Their result was 3.33 Å for bond length and 0 μ_B for total magnetic moment for the ground state. As we can see, their results are pretty similar as our results that we are reporting (Table 4.1) for DFT+U. The Hubbard term reduces hybridization of $s-d$ orbitals, as a result reduces the expansion of $3d$ orbital, therefore, resulting in weaker binding and longer bond length [21]. Thus adding U to PBE (DFT+U), we pass from FM to AF state and the bond length increases, as seen in Table 4.1.

Now, if we look carefully Figure 4.6 and 4.8, both are quite similar, especially the $4s$ states, but the physics behind them is different. PBE0 takes account the accurate version of exchange energy, meanwhile DFT+U strengthens the correlation effect. In Figure 4.9 we see that states close to the Fermi energy are antibonding, and this also explains the increase of bond length for the ground state compared to what was obtained with LSDA, GGA and meta-GGA functionals.

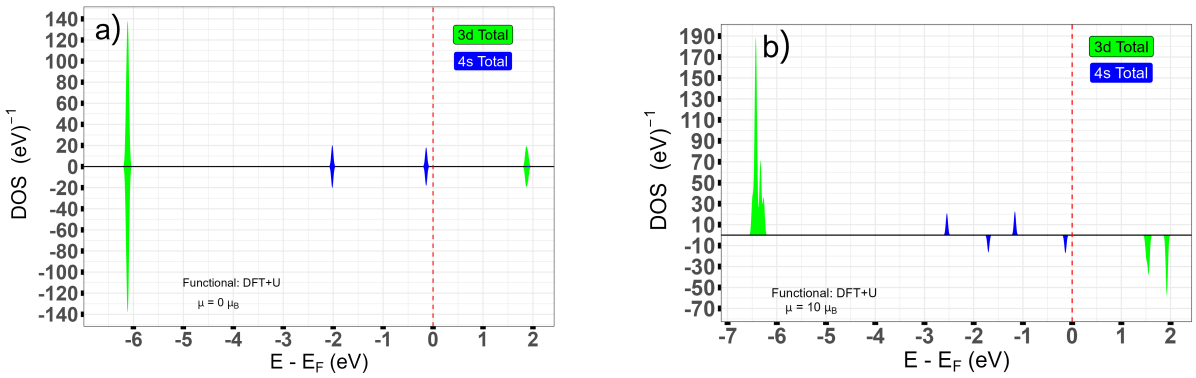

Figure 4.8: The Density of States (DOS) of Mn_2 for low energy states. The red dotted line presents the Fermi energy, E_F. States on the right side of E_F are unoccupied and on the left are occupied.

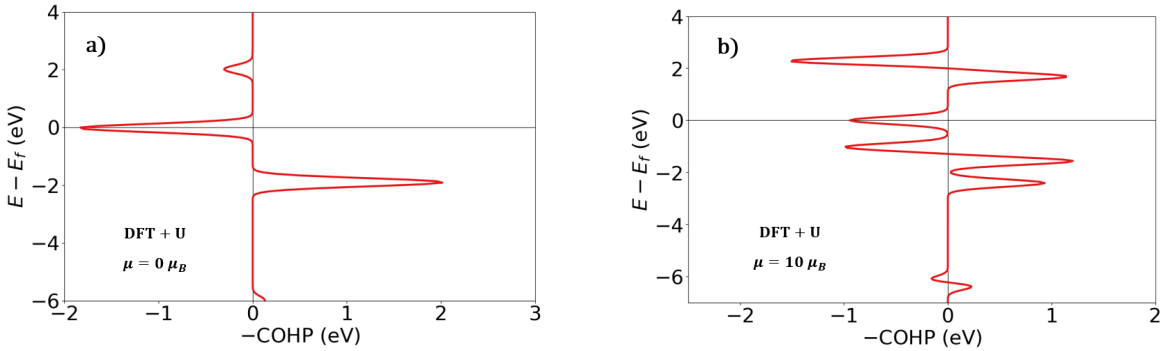

Figure 4.9: The Crystal Orbital Hamilton Populations (COHP) for Mn_2. The bonding orbitals are on the right side of each panel, meanwhile the antibonding are on the other side.

We want to emphasize again that the following functionals: B3LYP, PBE0, and wB97M-V are distinguished from DFT+U, because these combine Hartree-Fock exchange energy with DFT's exchange energy. As we have already shown, Mn is an element with a half-filled shell. Owing to the five electrons in the d orbital, the exchange energy is strong. Among hybrid functionals, B3LYP best describes Mn_2. For bond length we report 3.41 Å, and for bonding energy we also obtain an acceptable value 0.07 eV (see Table 4.1). Figure 4.10 depicts Mn_2 with its bond length and AF arrangements (0 μ_B) as the ground magnetic state. Similar results are reported by Yamanaka *et al.* [59] using GAMESS code which uses Gaussian type of orbitals. They find 0.42 Å for the bond length and 0.056 eV for bonding energy.

Functional	**Magnetic Ordering**	**Bond Length** (Å)	**Bonding Energy** (eV)	**Difference,** $\lvert AF - FM \rvert$ (eV)
LSDA	FM	2.50	1.20	0.39
PBE	FM	2.58	0.95	0.43
SCAN	FM	2.58	0.45	0.20
B3LYP	AF	3.41	0.07	0.35
DFT+U	AF	3.33	0.19	0.02
PBE0	AF	3.22	0.18	0.02
rev-SCAN	FM	3.23	0.22	4.0×10^{-4}
rev-TPSS	FM	2.67	0.68	0.33
SCAN2	FM	3.16	0.26	9.2×10^{-3}
wB97M-V	AF	3.95	–	7.6×10^{-3}

Table 4.1: Mn_2 characterization parameters, using different functionals in the plane waves basis set. Hybrid functionals are those that best describe Mn_2.

The last column of Table 4.1, is the difference between AF (0 μ_B) and FM (10 μ_B) orderings. We work with an *ab initio* method in the DFT framework where calculations are performed at 0 K. For experimental works, like performed by Knickelbein [22], he works within $\backsim$ 5 K or a bit lower than that. To determine if the states are degenerate or not, let's use the scale factor for energy $\Delta E = k_B T$ where $k_B = 8.61 \times 10^{-5} eV/K$. For most functionals, the difference is big because to pass from one state to another the temperature need to be high. For example consider wB97M-V, with $\Delta E = 7.6 \times 10^{-3} eV$ for which the temperature $T \backsim 88$ K is considerable higher than 5 K. Therefore AF and FM aren't degenerate states, which means that experimentally is not possible to measure both below 5 K. In contrast for rev-SCAN, $\Delta E = 4.0 \times 10^{-4} eV$ and temperature is $T = 4.6$ K which is a pretty low value (less than 5 K). In that case, for rev-SCAN AF and FM arrangements are degenerate states.

The local magnetic moment (LMM) for Mn_2, employing different functionals is given in Table 4.2, and these values were computed using the Voronoi Deformation Density (VDD) method (see the subsection 3.1.2.3). LMM depends on the exchange interaction, because when an electron flips its spin with respect to the other electron, the local magnetism is reduced. As we are going to show for other Mn clusters, LMM is related to the symmetry of the cluster geometry too.

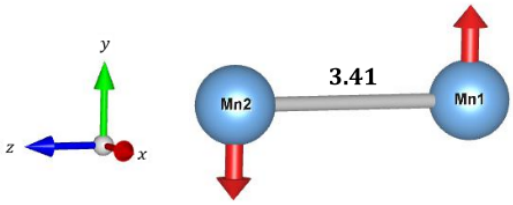

Figure 4.10: Bond length for Mn_2 in its ground magnetic state with the B3LYP functional in the plane waves basis set. B3LYP belongs to hybrid functionals which consider certain percentage of Hartree-Fock exchange energy.

For B3LYP, we have the Density of States (DOS) for the most stable states 0 μ_B and 10 μ_B. As shown in Figure 4.11 ***a)*** only 4*s* states are close to the Fermi energy, which means that AF is favored. Since 4*s* is a delocalized orbital, the bond length tends to be larger (3.41 Å). In addition, Figure 4.12 ***a)*** shows that 4*s* states are antibonding close to the Fermi energy and bonding roughly around -2 eV. In Figure 4.11 ***b)*** we see that electrons in the 3*d* orbital are much closer to the Fermi energy than electrons in the 4*s* orbital. The 3*d* orbital is a localized orbital, so electrons are closer to each other. In spite repulsion is strong, electrons are in a bonding orbital (Figure 4.12 ***b)***) so the bond length tends to be short (2.60 Å) although the system is unstable.

Functional	$\boldsymbol{\mu_1}$ (μ_B)	$\boldsymbol{\mu_2}$ (μ_B)	$\boldsymbol{\mu}$ **Total** (μ_B)
B3LYP	5.0263	-5.0263	0
DFT+U	5.1031	-5.1031	0
LSDA	4.9998	5.0002	10
PBE	4.9967	5.0033	10
PBE0	4.9605	-4.9605	0
rev-SCAN	5.0018	4.9982	10
rev-TPSS	4.9996	5.0004	10
SCAN	4.9916	5.0084	10
SCAN2	4.9987	5.0013	10
wB97M-V	-5.0291	5.0291	0

Table 4.2: Local magnetic moment μ_i and total magnetic moment for Mn_2 computed with the Voronoi Deformation Density method.

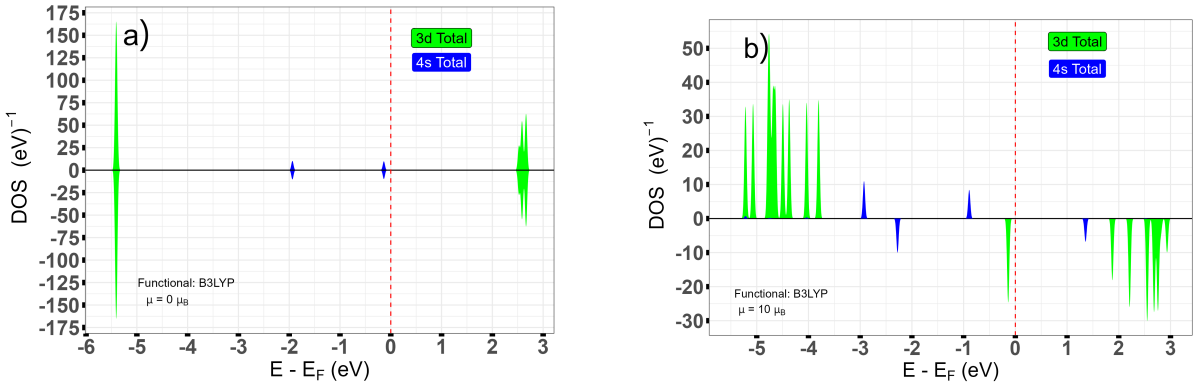

Figure 4.11: The Density of States (DOS) of Mn_2 for low energy states. The red dotted line presents the Fermi energy, E_F. States on the right side of E_F are unoccupied and on the left are occupied.

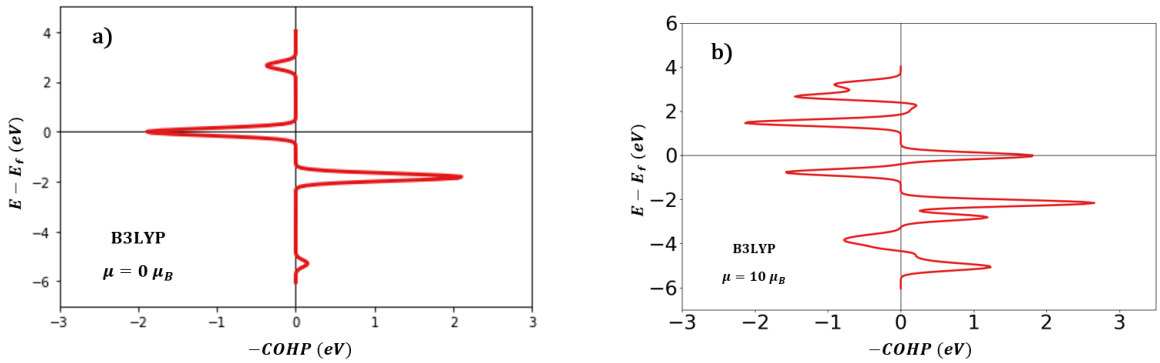

Figure 4.12: The Crystal Orbital Hamilton Populations (COHP) for Mn_2. The bonding orbitals are on the right side of each panel, meanwhile the antibonding are on the other side.

For another hybrid functional, wB97M-V in the plane waves basis gives an AF solution for the ground state. For DOS analysis in Figure 4.13 we note that states for 4s orbitals are closer each other compared with 4s orbitals for B3LYP' DOS. In both panels we see that, 4s occupied states close to the Fermi energy are antibonding (Figure 4.14). Although wB97M-V gives an AF solution for the ground state, it yields a bit longer bond length 3.95 Å (Table 4.1). As well for the FM solution, the bond length is large, 4.01 Å.

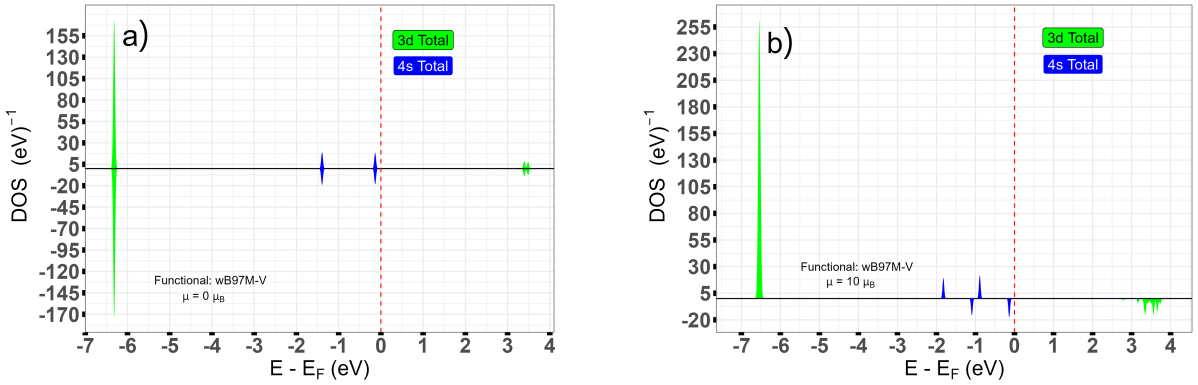

Figure 4.13: The Density of States (DOS) of Mn_2 for low energy states. The red dotted line presents the Fermi energy, E_F. States on the right side of E_F are unoccupied and on the left are occupied.

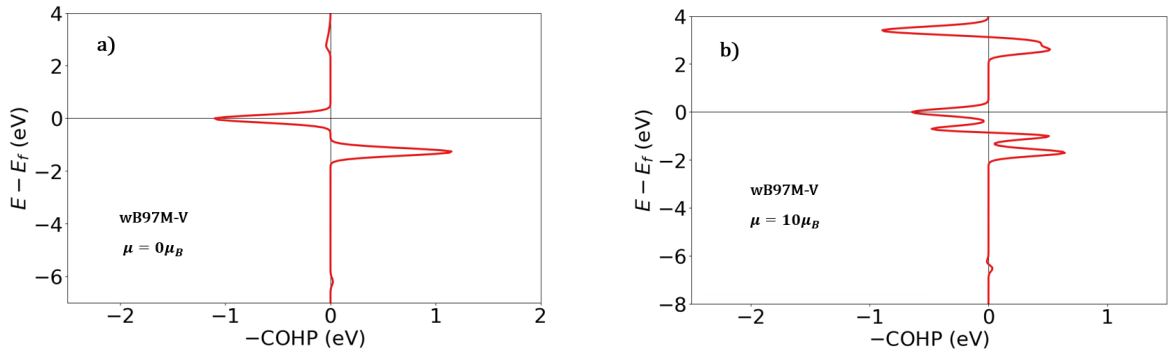

Figure 4.14: The Crystal Orbital Hamilton Populations (COHP) for Mn_2. The bonding orbitals are on the right side of each panel, meanwhile the antibonding are on the other side.

For the triple−ζ basis set in ORCA code (see subsection 3.2), we worked with B2PLYP and wB97M-V [60][61][62][63] hybrid functionals. Kohn-Sham orbitals are expanded in the triple−ζ which in general capture in a better way shape and size of atomic orbitals.

On the ground magnetic state, both functionals yield an AF ordering with a net spin of 0 μ_B. For B2PLYP the bond length is 3.58 Å whereas for wB97M-V it is 3.67 Å (Table 4.3). As shown in Figure 4.15, the behavior of the energy of the system described by both functionals is similar. Although the bond length is a bit out of range of experimental value, both functionals provide the correct spin arrangement for the ground state. Yamanaka *et al.* [59] for B2PLYP reported AF solution too with 3.93 Å for bond length and 0.011 eV for bonding energy. In Figure 4.16 there are optimal structures obtained for the low energy states computed with wB97M-V.

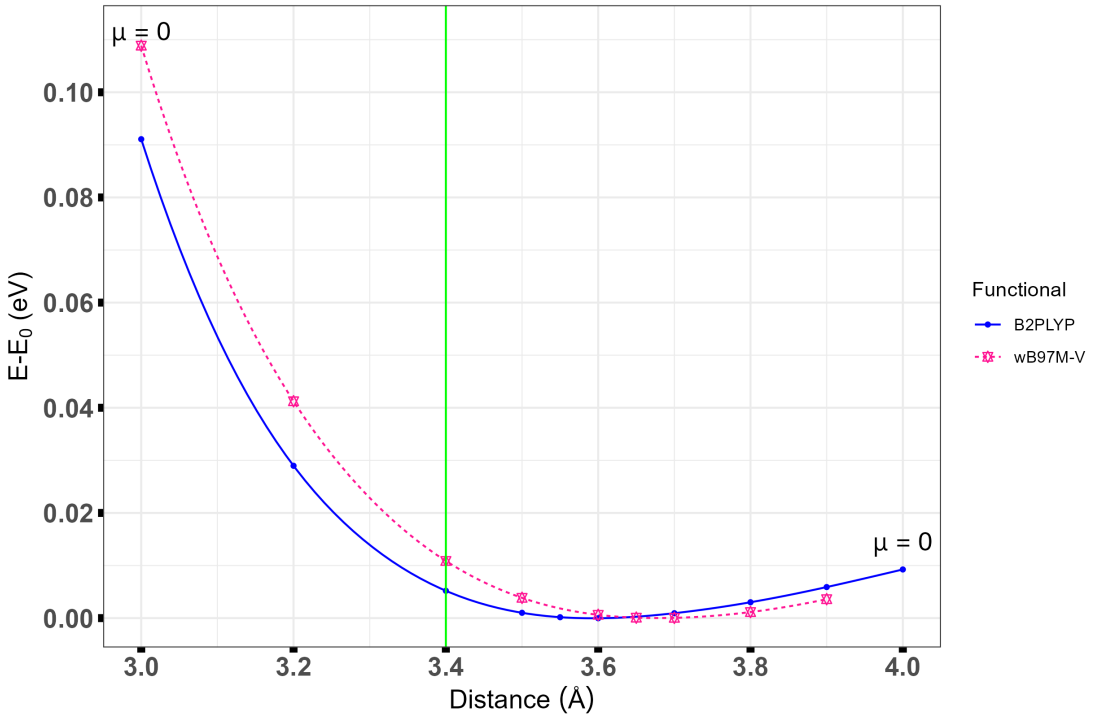

Figure 4.15: Variation of energy of Mn_2 as a function of distance in triple−ζ basis set. The green vertical line presents the experimental bond length (3.41 Å) when Mn_2 reaches its an equilibrium structure. For this cluster, AF ordering refers to the net magnetic moment 0 μ_B and Fm for 10 μ_B.

Functional	Magnetic Ordering	Bond Length (Å)	Difference, $\|AF - F\|$ (eV)
B2PLYP	AF	3.58	0.83
wB97M-V	AF	3.67	0.93

Table 4.3: Mn_2 characterization parameters, using hybrid functionals in the triple$-\zeta$ basis set.

Finally in Figure 4.16, we see the behavior of energy as a function of net magnetic moment for three functionals. The B3LYP functional gives the most accuracy results compared with the experimental measurements in the plane waves basis, whereas with triple$-\zeta$ basis we worked with B2PLYP, and wB97M-V functionals. As shown in Figure 4.16, the states of minimum energy are $\mu = 0\ \mu_B$ and $\mu = 10\ \mu_B$, and all functionals yield that same result. Here we see that hybrid functionals even implemented in codes (VASP, and ORCA) with different basis (plane waves, and triple$-\zeta$) describe pretty well Mn_2. These results encourage us to implement the same functionals for studying clusters up to seven atoms.

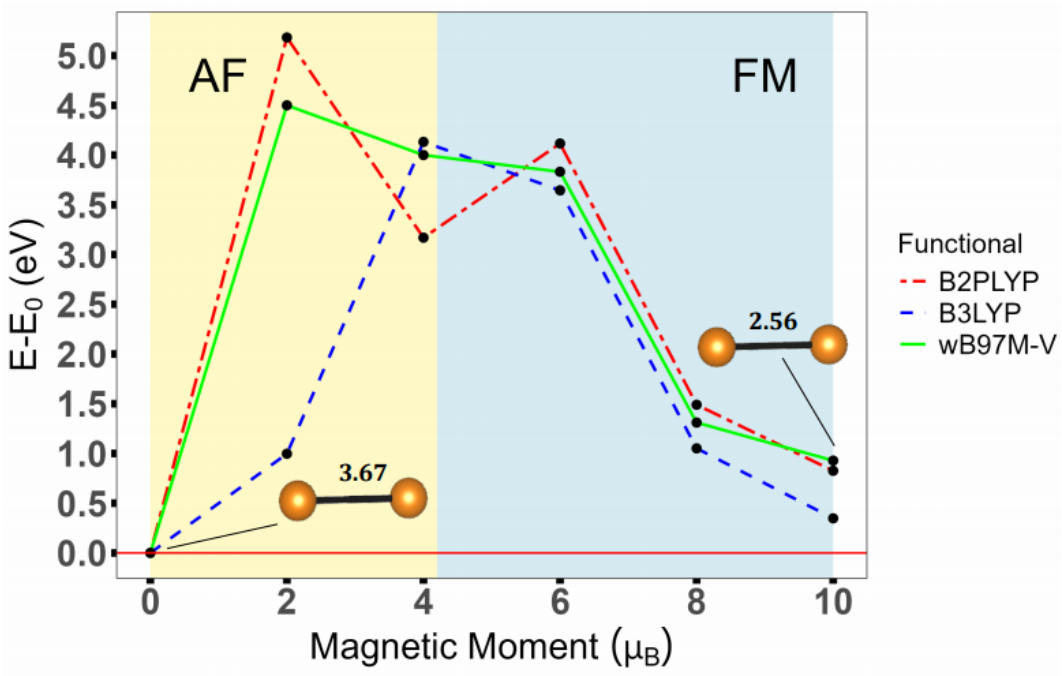

Figure 4.16: Variation of energy of Mn_2 as a function of magnetic moment. With the plane waves basis we have B3LYP functional whereas for the triple$-\zeta$ basis we work with B2PLYP, and wB97M-V. Low energy states correspond to 0 μ_B (AF) and 10 μ_B (FM). The optimal structures were obtained with wB97M-V in the triple$-\zeta$ basis.

4.2 Manganese trimer, Mn_3

For the cluster of three atoms, there are a couple of starting structures. For instance, one option could be to place three atoms in the same line with some distance between them like with the dimer (Figure 4.10). Another option is has a triangle as starting geometry. For our study we chose an equilateral triangle as initial locations of the three atoms. We have to keep in mind that by ionic steps and structural relaxation, the initial geometry can change.

For Mn_3, the possible atomic moments are odd numbers like 1 μ_B, 3 μ_B until 15 μ_B as shown in Figure 4.17. The highest magnetic moment is 15 μ_B which is achieved when the electrons in $3d$ orbitals

for each atom have the same orientation (spin down or up). The lowest magnetic moment 1 μ_B occurs when 7 of the total 15 electrons in d orbitals have opposite orientation. As a guide for the rest of the chapter, AF is when individual atomic magnetic moments have opposite orientation whereas FM is when magnetic moments have the same orientation.

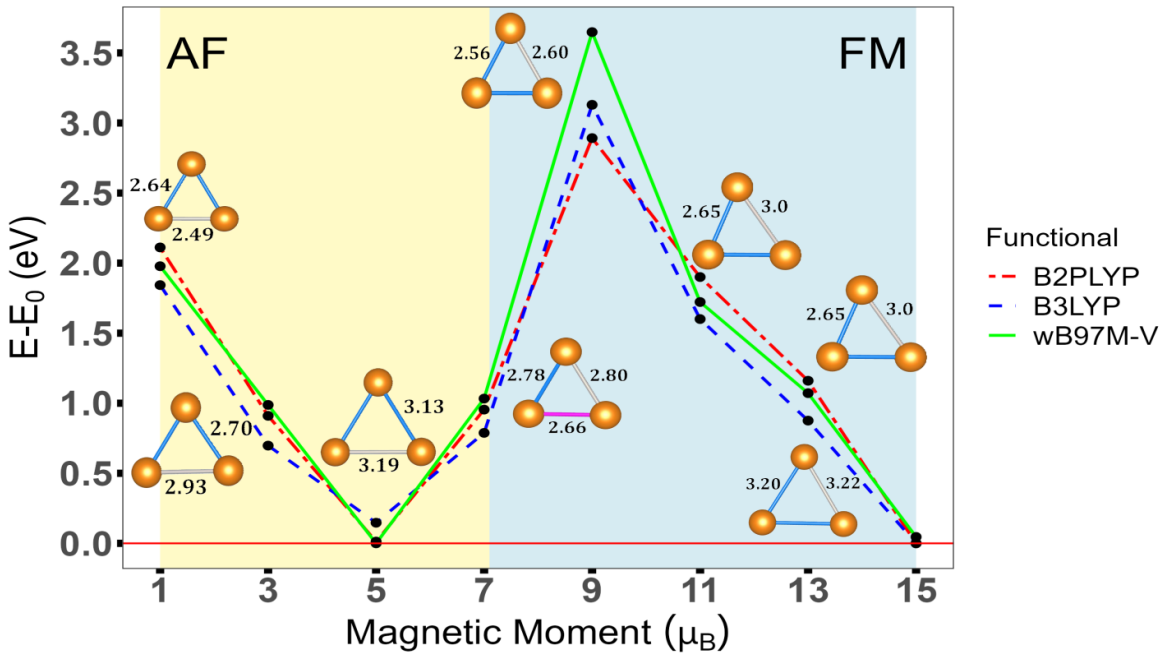

Figure 4.17: Variation of energy of Mn_3 as a function of magnetic moment. With the plane waves basis we have B3LYP functional whereas for the triple$-\zeta$ we work with B2PLYP, and wB97M-V. Low energy states correspond to 5 μ_B (AF) and 15 μ_B (FM). The optimal structures were obtained with wB97M-V in the triple$-\zeta$ basis.

Figure 4.17 shows the energy of the system as a function of magnetic moment for three hybrid functionals. In the triple$-\zeta$ basis we work with B2PLYP, and wB97M-V. In the plane waves basis we work with B3LYP. In our findings there are two states with minimum energy $\mu = 15\ \mu_B$ and $\mu = 5\ \mu_B$. For B3LYP, Figures 4.20 and 4.17 show that the FM ordering (15 μ_B) is the most stable state, followed by the AF ordering (5 μ_B). AF ordering is $\Delta E = 0.15\ eV$ above the ground state. This result is quite similar to that reported by Bodadova-Parvanova *et al.* [57] but they used the PBE (GGA) functional in the NRLMOL code with the Gaussian basis. In addition, Kabir *et al.* [48] reported a similar result with the same functional but using VASP code.

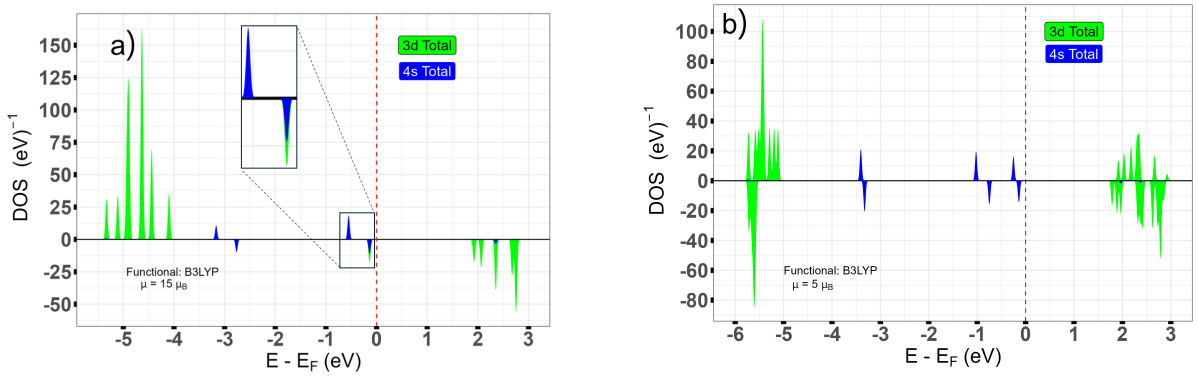

Figure 4.18: The Density of States (DOS) of Mn_3 for low energy states. The red dotted line presents the Fermi energy, E_F. States on the right side of E_F are unoccupied and on the left are occupied.

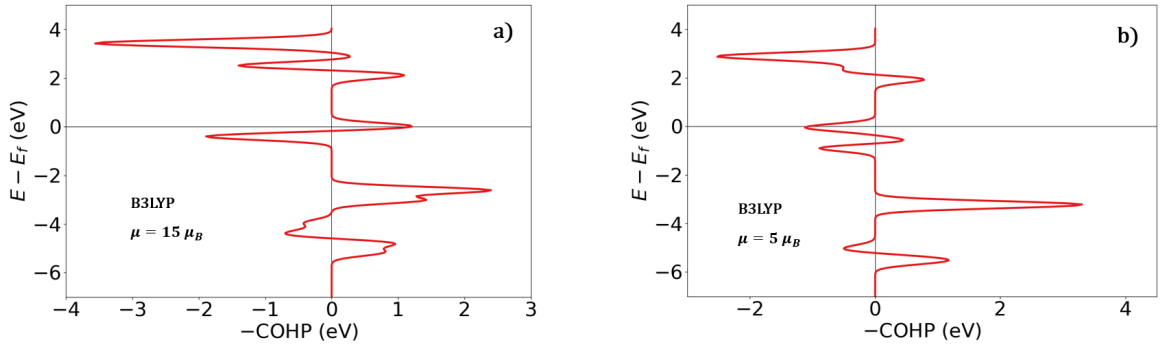

Figure 4.19: The Crystal Orbital Hamilton Populations (COHP) for Mn_3. The bonding orbitals are on the right side of each panel, meanwhile the antibonding are on the other side.

For the DOS analysis, in Figure 4.18 ***a)*** we see a strong hybridization of $s-s$, and $s-d$ orbitals close to the Fermi energy. The $s-d$ hybrid orbitals are bonding as shown in Figure 4.19 ***a)***, therefore the bonding among atoms is strong, and the bond length may be short owing to the $3d$ orbitals. On the other hand, in Figure 4.18 ***b)*** for AF ordering, we see that there aren't $3d$ states close to the Fermi energy, and the $4s$ states favor antiferromagnetism. In Figure 4.19 ***b)*** we see that $4s$ states are antibonding, which makes the system less stable. In addition, the long bond lengths of the AF structure (Figure 4.20 ***b)***) is due to the contribution of $4s$ states as these are delocalized orbitals and also because these states are more separated energetically from each other and from the Fermi energy. In Figure 4.18 ***a)*** there are more degenerate $3d$ states in contrast of Figure 4.18 ***b)*** where is less. High degeneracy is owing to the symmetric structure (Figure 4.20) for isomer ***a)***.

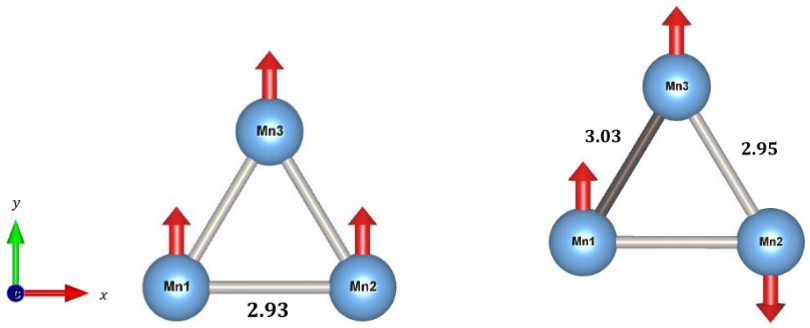

(a) ($\Delta E = 0\ eV$, $15\ \mu_B$) **(b)** ($\Delta E = 0.15\ eV$, $5\ \mu_B$)

Figure 4.20: The low energy states for Mn_3 and their optimal structures obtained with B3LYP functional in the plane waves basis. ΔE is the energy difference with respect to the ground state ($15\ \mu_B$).

Isomer	$\boldsymbol{\mu_1}$ (μ_B)	$\boldsymbol{\mu_2}$ (μ_B)	$\boldsymbol{\mu_3}$ (μ_B)	$\boldsymbol{\mu}$ **Total** (μ_B)
a)	4.9997	5	5.0003	15
b)	4.9819	-4.9641	4.9822	5

Table 4.4: Local magnetic moment μ_i and total magnetic moment for Mn_3 computed with the Voronoi Deformation Density method using the B3LYP functional.

Figure 4.20 presents the optimal final geometries obtained with B3LYP functional for stable states. For $15\ \mu_B$ we have an equilateral triangle with sides of 2.93 Å whereas for $5\ \mu_B$ we have an isosceles triangle with sides 2.95 Å and 3.03 Å. For the isosceles triangle, the short distance is between the atoms with anti-parallel spins, in accordance with the Pauli exclusion principle. In general, the large bond lengths correspond to AF ordering because the $4s$ orbitals are antibonding. Meanwhile for FM ordering

the $4s$ are bonding as shown in Figure 4.19. It is clear that for both isomers, $4s$ orbitals, play a crucial role to understand the bond length.

Table 4.4 shows LMM for the most stable states, and all values are close to 5 μ_B or -5 μ_B. The homogeneity of spatial distribution of the magnetic moment also explains the symmetry of isomers obtained with B3LYP.

For B2PLYP, the ground state corresponds to FM ordering (15 μ_B) but the other minimum (5 μ_B) is only $\Delta E = 0.013\ eV$ above it. As we see, we have the same local minima and ground state such as with B3LYP.

With wB97M-V in the triple$-\zeta$ basis we obtained a different result than the previous functionals. As shown in Figure 4.17, for wB97M-V the most stable state is AF ordering (5 μ_B) while the FM ordering (15 μ_B) is $\Delta E = 0.045\ eV$ above. Unfortunately, for this cluster there are no experimental measurements about the ground magnetic state to compare with our computational results. However, based on the experimental values for the other clusters (Table 1) where net spin isn't large, we conjecture that 5 μ_B (1.67 μ_B per atom) is the best approximation to the true value.

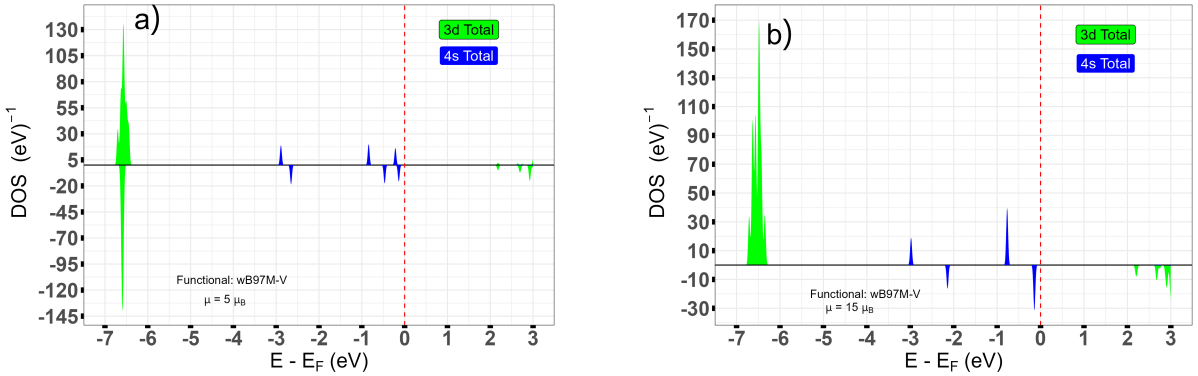

Figure 4.21: The Density of States (DOS) of Mn_3 for low energy states. The red dotted line presents the Fermi energy, E_F. States on the right side of E_F are unoccupied and on the left are occupied.

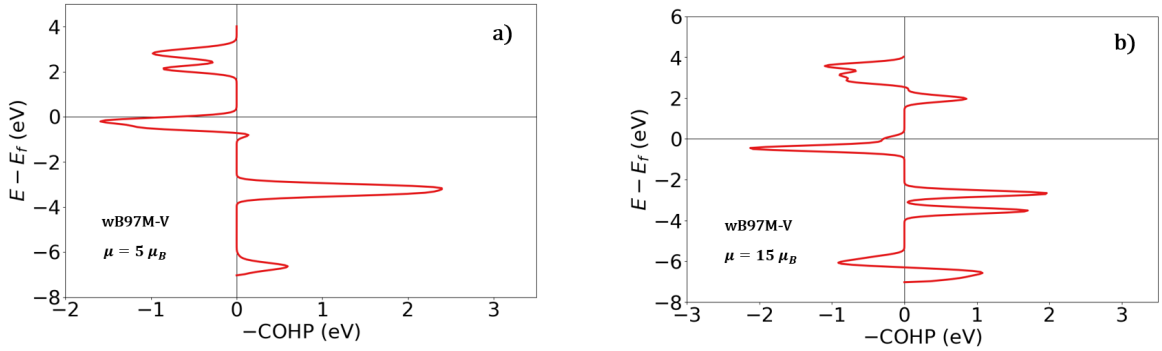

Figure 4.22: The Crystal Orbital Hamilton Populations (COHP) for Mn_3. The bonding orbitals are on the right side of each panel, meanwhile the antibonding are on the other side.

As shown in Figure 4.17, the type of functional is very important, even with functionals which belong to the same Jacob's ladder (see subsection 2.3.3.1). B3LYP and B2PLYP functionals both are hybrid functionals (see subsection 2.3.3.5) but wB97M-V belongs to a subgroup of hybrid functionals called Range-Separated Hybrid (RSH) functional (see subsection 2.3.3.6). The main difference between both is the treatment of exchange energy, and RSH is more accurate for longer inter-electronic distance. As we have mentioned for Mn_2, our systems in general are sensitive to exchange energy, so any change on this may yield different results.

The wB97M-V functional also was worked with the plane waves basis, and we have an AF solution for the ground state with a magnetic moment 5 μ_B. The other stable state corresponds to 15 μ_B which is $\Delta E = 0.038\ eV$ above the AF solution. In summarize, with the same functional, the Kohn-Sham equations solved in different basis set gave the same solution for the ground state.

Now let's analyze the DOS for each stable state obtained with wB97M-V in the plane waves basis. Figure 4.21 ***a)*** is the DOS for AF arrangement, where there are $4s$ states close to the Fermi energy, although the hybridization is not strong. Looking at Figure 4.22 the $4s$ are classified as antibonding orbitals. On the other hand, for FM ordering in Figure 4.21 we see a strong hybridization between $s-s$ orbitals close to the Fermi energy. Owing to $s-s$ being as delocalized orbitals these favor a large bond length. As with the AF ordering, for the FM arrangement we note (Figure 4.22 ***b)***) that the $4s$ states close to the Fermi energy are antibonding, but these antibonding orbitals are greater than $4s$ antibonding orbitals for the AF ordering. Thus, 5 μ_B is more stable than 15 μ_B, therefore this is the ground state according with wB97M-V functional. Seen carefully Figure 4.21 ***b)*** shows a bit more degeneracy of $3d$ states compared to isomer ***a)***, which mean that optimal structure for ***b)*** is high symmetric.

4.3 Manganese tetramer, Mn_4

As we increase the number of atoms, the problem becomes more complex. For the tetramer and for the following Mn clusters there are multiple degrees of freedom such as: structure, total magnetic moment, and the arrangement of individual atomic magnetic moments. Regarding to the initial structure we chose working with a tetrahedron. Is evident that there are more structures for Mn_4, like the square and rhombus, but most theoretical and computational studies work with the tetrahedron. Therefore with the desire to compare our results with previous studies we employ this geometry too.

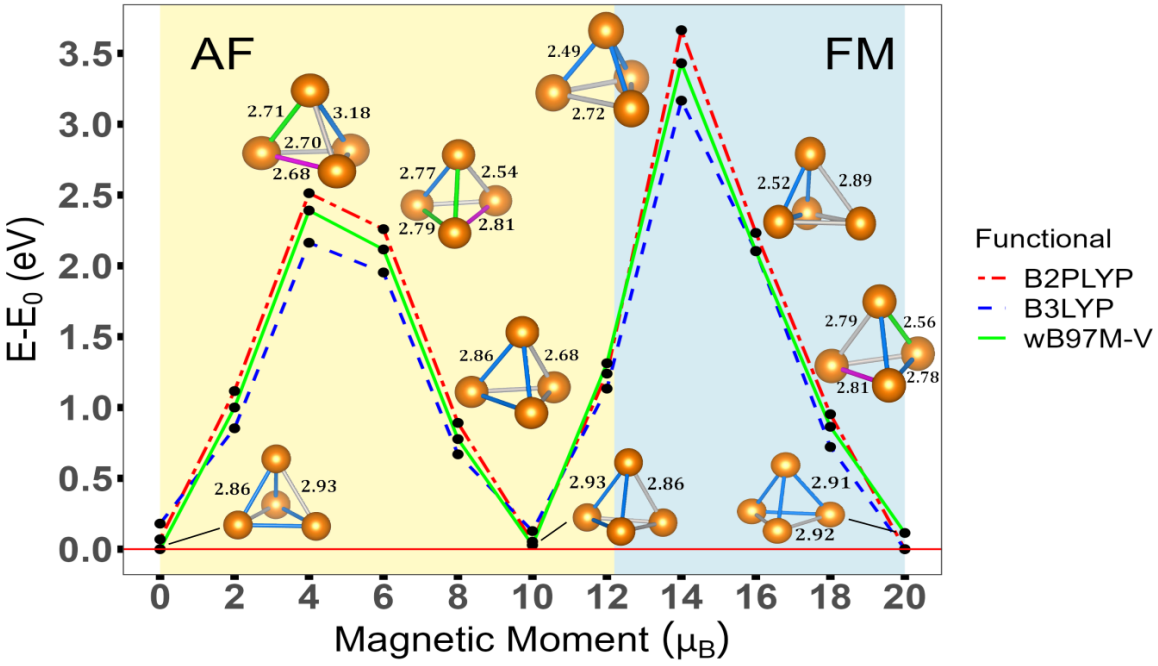

Figure 4.23: Variation of energy of Mn_4 as a function of magnetic moment. With the plane waves basis we have B3LYP functional whereas for the triple$-\zeta$ we work with B2PLYP, and wB97M-V. Low energy states correspond to 0 μ_B (AF), 10 μ_B (AF), and 20 μ_B (FM). The optimal structures were obtained with wB97M-V in the triple$-\zeta$ basis.

With the B3LYP functional, our findings are shown in Figures 4.23 and 4.26. The most stable state is 20 μ_B (5 μ_B per atom) meanwhile the other local minima are 10 μ_B and, 0 μ_B which are $\Delta E = 0.13\ eV$

and, $\Delta E = 0.18\ eV$ above it. According to previous studies [20][21], the ground state that corresponds to Mn_4 is FM state with a net magnetic moment 20 μ_B which agrees with our result. Unfortunately there are no experimental measurements available to verify our computational results. Other first principle calculations also find a ferromagnetic ordering for the ground state. For instance Bobadova-Parvanova *et al.* [57] reported 20 μ_B (5 μ_B per atom) as the ground state and the same result was reported by Kabir *et al.* [48].

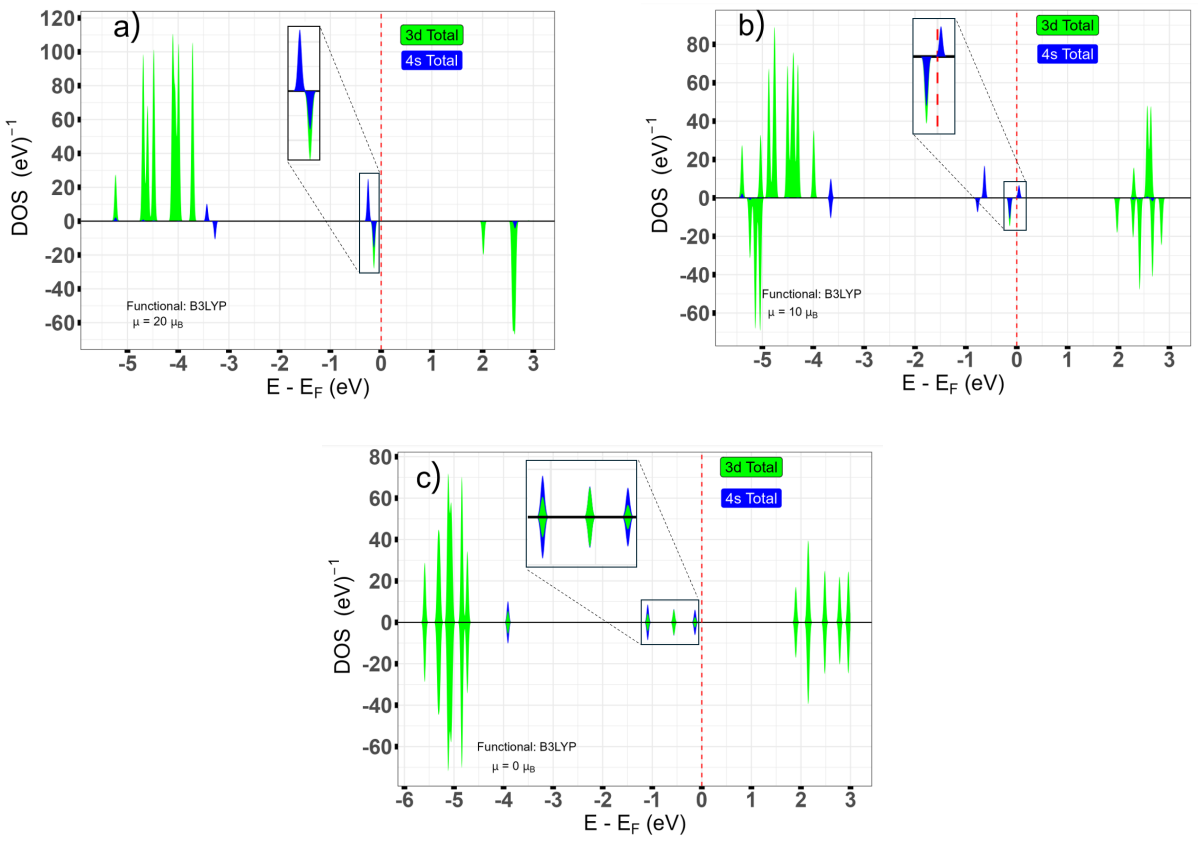

Figure 4.24: The Density of States (DOS) of Mn_4 for low energy states. The most stable state corresponds to $\mu = 20\ \mu_B$ which is a FM solution. The red dotted line presents the Fermi energy, E_F. States on the right side of E_F are unoccupied and on the left are occupied.

Now let's take a look on DOS analysis for each stable state. For isomers ***a)***, ***b)*** and ***c)*** in Figure 4.24 there are occupied electronic states with spin up and down very close to the Fermi energy. For isomer ***a)*** we see a much stronger $s-s$ and $s-d$ hybridization compared with the other isomers. If we see Figure 4.25 ***a)*** COHP analysis, we note that $4s$ and $3d$ orbitals in isomer ***a)*** are bonding orbitals, so that these favor short bond lengths. In general, bonding orbitals have lower energy than original orbitals, so the isomer ***a)*** is more stable. For the AF solutions, the isomers ***b)*** and ***c)*** as we mentioned there are orbital hybridization although for both these new orbitals are antibonding (Figure 4.25 ***b)***, and ***c)***). The antibonding nature of the orbitals close to the Fermi energy explains why the bond lengths for isomers ***b)***, and ***c)*** are a bit larger than for isomer ***a)***. The high degeneracy in panel ***a)*** is consequence of the symmetric structure presented by isomer ***a)***.

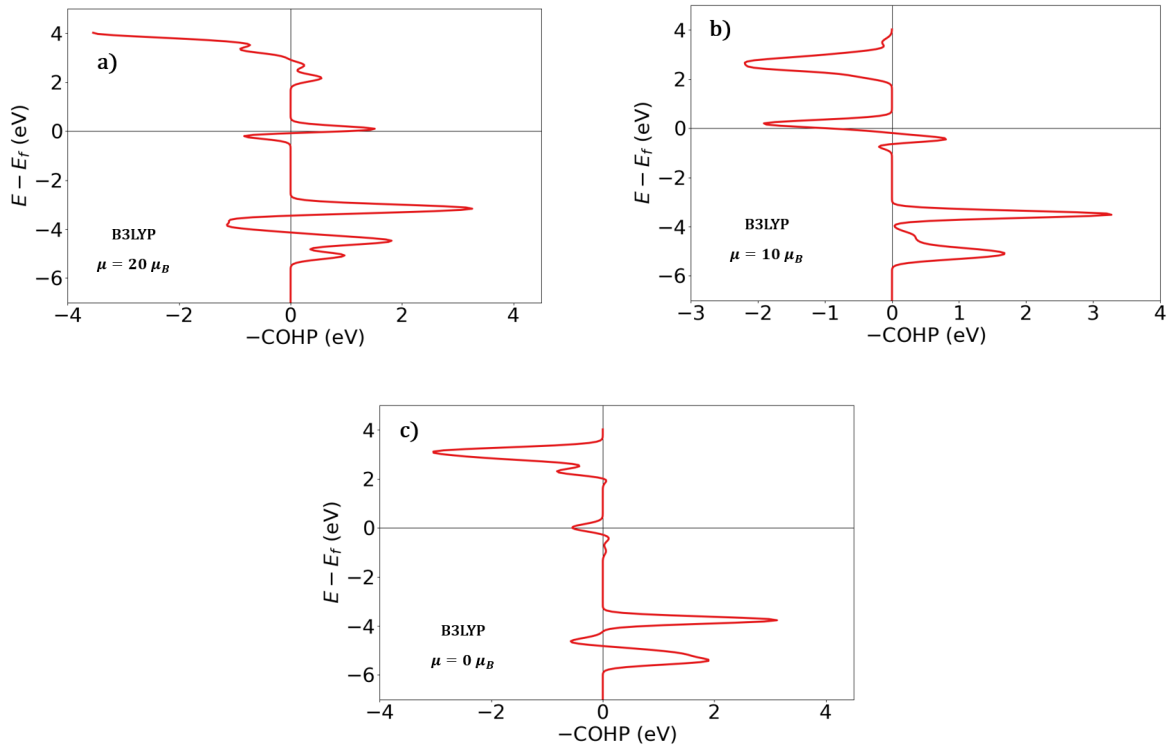

Figure 4.25: The Crystal Orbital Hamilton Populations (COHP) for Mn_4. The bonding orbitals are on the right side of each panel, meanwhile the antibonding are on the other side.

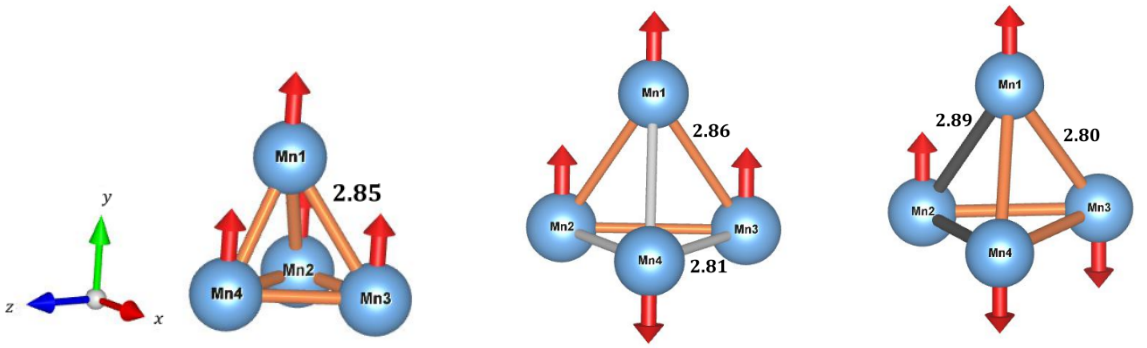

(a) (ΔE =0 eV, 20 μ_B) **(b)** (ΔE =0.13 eV, 10 μ_B) **(c)** (ΔE =0.18 eV, 0 μ_B)

Figure 4.26: The low energy states for Mn_4 and their optimal structures obtained with B3LYP functional in the plane waves basis. ΔE is the energy difference with respect to the ground state (20 μ_B).

For the optimal structures obtained with B3LYP let's see Figure 4.26. The bond lengths in all of these isomers varies between 2.80 Å and 2.89 Å, so the values presented by each one are very similar. For the FM ordering (20 μ_B) we have a regular tetrahedron with a bond length of 2.85 Å, whereas for other states, we have irregular tetrahedrons owing to the anti-parallel spins. For instance, for 10 μ_B, the distance between atoms with the same orientation of spin (spin up) is 2.86 Å. For the same structure, the distance between atoms with opposite spin (spin down and up) is 2.81 Å which is a little smaller than 2.86 Å. Therefore, the variation in the direction of the spin induces a certain asymmetry. The previous analysis agrees with the Pauli exclusion principle.

Isomer	μ_1 (μ_B)	μ_2 (μ_B)	μ_3 (μ_B)	μ_4 (μ_B)	μ Total (μ_B)
a)	5	5.0002	5	4.9999	20
b)	4.9536	4.9536	4.9533	-4.8605	10
c)	4.9064	4.9069	-4.9066	-4.9067	0

Table 4.5: Local magnetic moment μ_i and total magnetic moment for Mn_4 computed with the Voronoi Deformation Density method using the B3LYP functional.

Regarding the local magnetic moment (Table 4.5), for isomer ***a)*** each atom practically has the same magnetic moment. Further, for isomers ***b)*** and ***c)*** there are slight differences in the magnetic moment per atom and this is reflected in the irregular geometries of both isomers.

After discussing for B3LYP functional, now let's examine our results for B2PLYP and wB97M-V implemented in ORCA in the triple$-\zeta$ basis. In Figure 4.23 for B2PLYP the ground state corresponds to 20 μ_B and its difference with 10 μ_B and 0 μ_B is $\Delta E = 0.052\ eV$, and $\Delta E = 0.070\ eV$. Although B3LYP and B2PLYP gave the same ground state, the energy difference with the other isomers is very different.

The wB97M-V functional provides a different results than the previous ones. The lowest energy state has a net spin 0 μ_B (AF ordering), followed by 10 μ_B and 20 μ_B which are $\Delta E = 0.03\ eV$ and, $\Delta E = 0.11$ eV above. According with this functional, Mn_4 lacks magnetism in its ground state. One thing that we notice, as shown in Figure 4.23 is that the local minima are the same for the functionals, although the ground state may be different. Thus, it is very likely that codes that solve the Kohn-Sham equations in different bases will not have relevance to find local minima. However the basis set may be relevant for bond lengths, bonding energy and to determine the ground state.

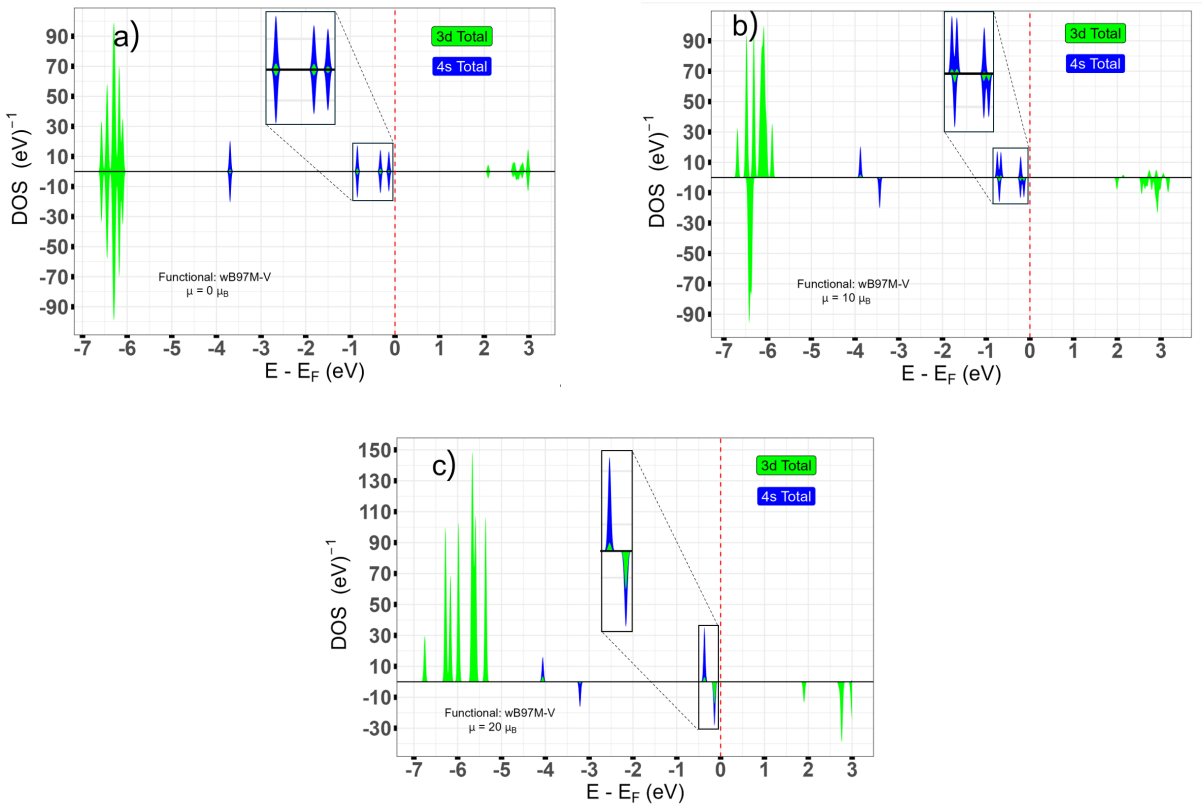

Figure 4.27: The Density of States (DOS) of Mn_4 for low energy states. The most stable state corresponds to $\mu = 0\ \mu_B$ which is an AF solution. The red dotted line presents the Fermi energy, E_F. States on the right side of E_F are unoccupied and on the left are occupied.

Before continuing we want to emphasize that the results obtained with the wB97M-V functional in the plane waves, and in the triple$-\zeta$ basis are basically the same. Even the energy difference ΔE relative to the ground state is the same for both basis. For this reason there is no problem in saying that the behavior of the wB97M-V in the plane waves basis is the same as that shown in Figure 4.23 in the triple$-\zeta$.

Now let's see Figure 4.27 the DOS analysis for the most stable states computed with wB97M-V in the plane waves basis. For isomers ***a)*** and ***b)*** there are $s-s$ orbital hybridization ($3d$ states close to the Fermi energy are practically negligible), whereas for ***c)*** there are $s-s$ and $d-d$ hybridization. In isomer ***c)***, there a bit more $s-d$ orbital hybridization. In the same time, we observe much more s states (promote large bond length) near the Fermi energy, and these states are antibonding (Figure 4.28). For the previous statement isomer ***c)*** is not the most stable state. For ***b)*** the $4s$ orbitals hybridization are a bit greater than for isomer ***a)***, so there are more electrons with the same energy for isomer ***b)*** and these electrons belong to antibonding orbitals (Figure 4.28). As we already know, the shape of s orbitals is like a sphere, so electrons have much place to move but especially for this case the motion is not between the atoms therefore does not promote bonding. Finally, for the ground state ($0\ \mu_B$) it is evident that there are the same $4s$ states with spin up and down. Therefore the electrons are more together and promote bonding making the cluster more stable.

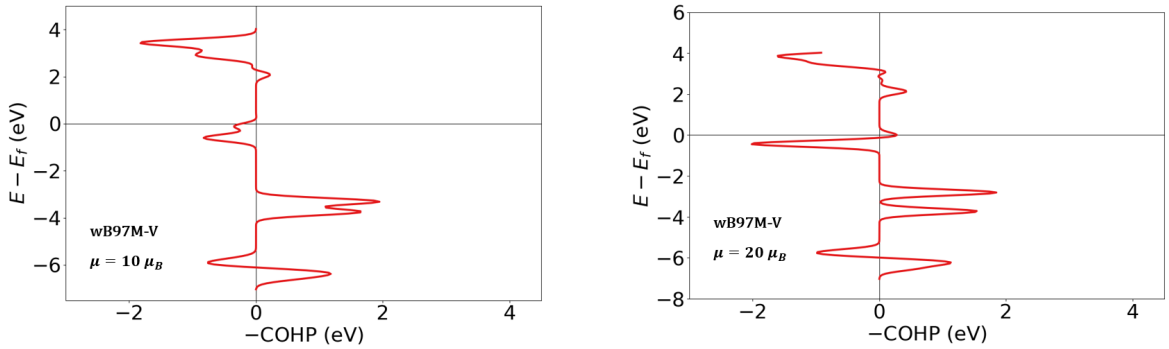

Figure 4.28: The Crystal Orbital Hamilton Populations (COHP) for Mn_4. The bonding orbitals are on the right side of each panel, meanwhile the antibonding are on the other side.

In Figure 4.23 we see some optimal structures obtained with wB97M-V in the triple$-\zeta$ basis. In general, the bond lengths for the lower energy states range between 2.86 Å$-$ 2.93 Å. Also, we note certain symmetry among the stable states in contrast with higher energy states. Finally, if we compare the bond lengths of the most stable states obtained with wB97M-V and B3LYP, the bond lengths are longer for the first one. If we look DOS analysis for both (Figures 4.24, and 4.27), we see more $s-d$ hybridization in B3LYP than with wB97M-V. The $4s$ orbitals are delocalized, although the presence of $3d$ orbitals causes a strong repulsion. However these orbitals are localized, and even bonding orbitals, which promote short bond lengths.

4.4 Manganese pentamer, Mn_5

We have studied Mn_5 cluster under collinear and non-collinear atomic spin moment schemes. Collinear arrangement is the first approach, where spins are parallel or antiparallel to each other, whereas for non-collinear spin arrangements point in various directions. As we are going to discuss, the motivation behind non-collinear arrangements is to find an explanation for smaller magnetic moments for larger Mn clusters. So, let's examine each one of approaches.

4.4.1 Collinear structure for Mn_5

For Mn_5, we consider a triangular bipyramid as an initial geometry for atoms locations. For studying this cluster we employed the following functionals: B3LYP, B2PLYP, and wB97M-V. As we already discussed for previous clusters, the basis set doesn't have a significant impact for the determination of the stable states, although it could change which one is the most stable. In Figure 4.29 we have the variation of energy with the magnetic moment, and here it is easy to identify the lower energy states.

For B3LYP the ground magnetic state is FM ordering with a net spin 25 μ_B (5 μ_B per atom). This result agrees with the result obtained in ESR experiment, 5 μ_B per atom (Table 1 [21]). However, it disagrees with the result obtained in the molecular beam deflection experiment, 0.79 $\mu_B \pm 0.25$ μ_B per atom (Table 1 [22]), which is an AF solution. Computational study performed by Huang *et al.* [21] with Hubbard method (DFT+U) gives FM solution for the ground state with magnetic moment 5 μ_B per atom. Hubbard method emphasizes on correlation effect but B3LYP emphasizes on exchange energy, but both yield the same result. As we can see is hard to reach a consensus between the results and the physical reason behind them.

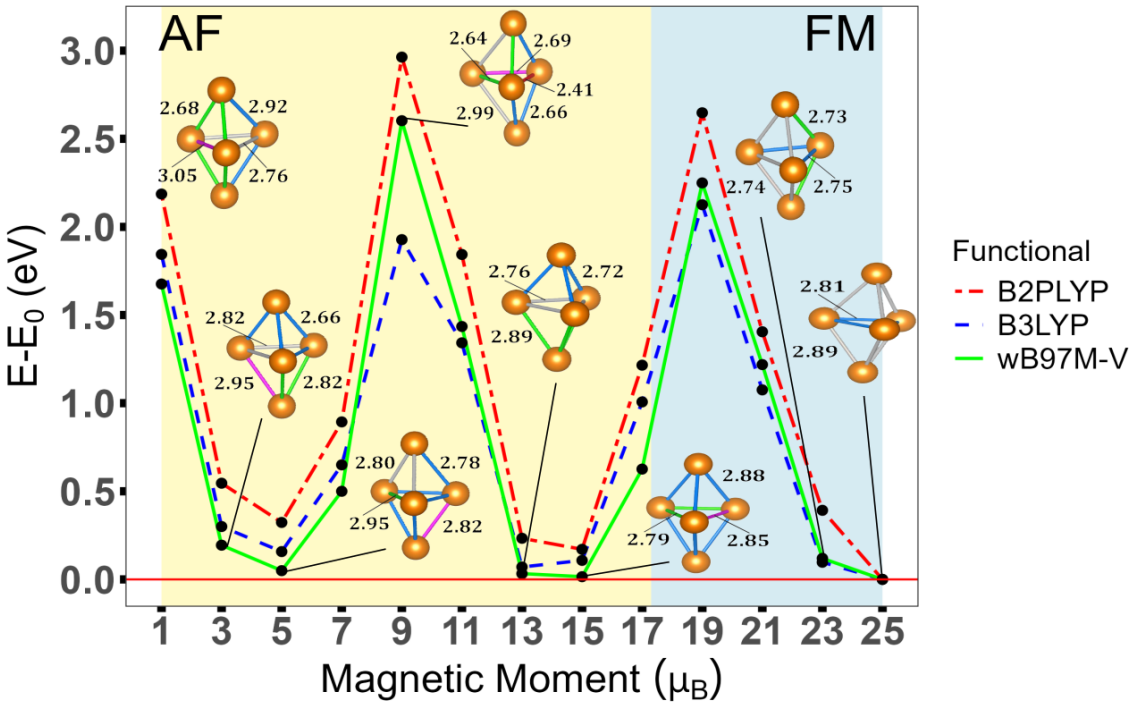

Figure 4.29: Variation of energy of Mn_5 as a function of magnetic moment. With the plane waves basis we have B3LYP functional whereas for the triple$-\zeta$ basis we work with B2PLYP, and wB97M-V. Low energy states correspond to 5 μ_B (AF), 13 μ_B (AF), 15 μ_B (AF), and 25 μ_B (FM). The optimal structures were obtained with wB97M-V in triple$-\zeta$ basis.

In Figure 4.30, we have relative energy ΔE of many of low energy states with respect to the ground state. As we can see there is no any degenerate states, owing the energy difference is big. The state closest to the ground state is 13 μ_B which is an AF solution.

Figure 4.31 are the DOS analysis for stable states. In our findings we see $4s$ and $3d$ orbitals are close to the Fermi energy, which are relevant for giving an explanation of the ground state, molecular bonding, bond lengths and other properties. For isomers ***b***), and ***c***) we note that above -1 eV there are basically only $3d$ states, and electrons in these states are localized which means they aren't free to move everywhere. In general $3d$ orbitals favor short bond lengths owing to their shape, and at the same time strong repulsion among electrons and strong hybridization causes unstable isomers. For isomer ***a***) we see a greater participation of $3d$ and $4s$ states near the Fermi energy, and as shown in Figure 4.32 these states are bonding orbitals. Electrons in bonding orbitals play an essential role to keep atoms together and for stabilizing the cluster. In each panel of Figure 4.31 we see the splitting of d orbitals and these is

abundant in the range of -6 eV − 4 eV. As with other clusters, high degeneracy of $3d$ states for isomers ***a)*** and ***c)*** is owing at the high symmetry of structures. we emphasizes that $3d$ states close to the Fermi energy is due to the self-interaction error (SIE), which is not removed completely by B3LYP.

Isomer	μ_1 (μ_B)	μ_2 (μ_B)	μ_3 (μ_B)	μ_4 (μ_B)	μ_5 (μ_B)	μ **Total**
a)	5.2317	4.8472	4.8455	4.8461	5.2295	25
b)	4.4868	4.6388	4.636	4.6378	-5.3993	13
c)	5.1227	-4.8092	4.7823	4.7811	5.1232	15
d)	4.7663	4.771	4.77	-4.69	-4.6173	5

Table 4.6: Local magnetic moment (LMM) μ_i and the total magnetic moment for Mn_5 computed with the Voronoi Deformation Density method using the B3LYP functional.

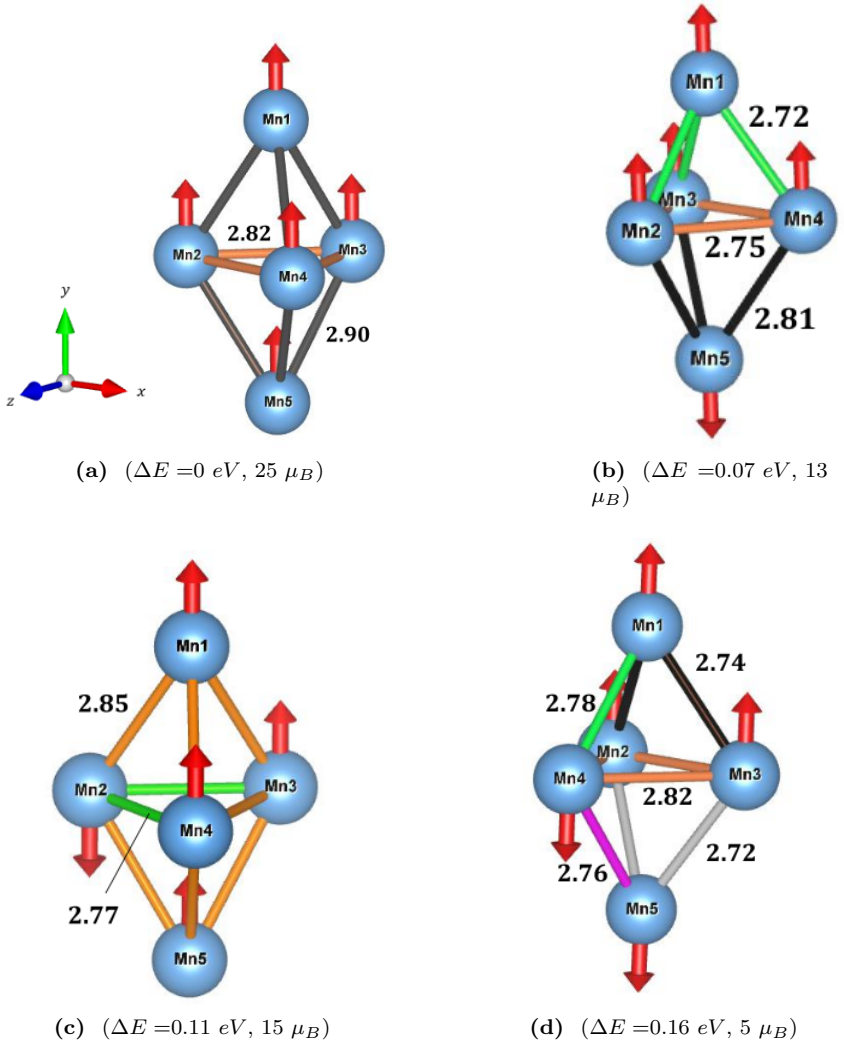

(a) (ΔE =0 eV, 25 μ_B)

(b) (ΔE =0.07 eV, 13 μ_B)

(c) (ΔE =0.11 eV, 15 μ_B)

(d) (ΔE =0.16 eV, 5 μ_B)

Figure 4.30: The low energy states for Mn_5 and their optimal structures obtained with B3LYP functional in the plane waves basis. ΔE is the energy difference with respect to the ground state (25 μ_B).

Regarding optimal structures, in Figure 4.30 we see the results obtained with B3LYP. In isomer ***a)*** we observed a regular bypiramidal structure. The bond lengths range between 2.82 Å− 2.90 Å which are greater than bond lengths from other stable states. Besides, in Figure 4.31 we note a strong hybridization of orbitals $4s$ and $3d$, especially for $4s$ which causes a larger bond lengths. For isomer ***b)*** we have two

regular pyramids with the same base. The upper pyramid is a bit smaller than lower one. Seeing Table 4.6 in isomer ***b)*** the atom 5 has a greater magnetic moment, therefore the charge is greater too, which implies a strong repulsion. So, if there is a difference of charge (or LMM) between atoms even with opposite spin orientation the bond length may be larger. Finally, in case of isomer ***c)*** it is an irregular bypiramid, because for the upper pyramid the bond lengths are 2.78 Å and 2.74 Å, whereas for the lower pyramid the sides are 2.76 Å, 2.82 Å, and 2.72 Å. Seeing Table 4.6 for isomer ***c)***, most of atoms have different LMM which means that in some parts there are strong Coulomb interactions yielding large bond lengths and in other it is not. The short bond lengths for isomers ***b)***, and ***c)*** also can be explained by $3d$ states close to the Fermi energy (Figure 4.31) and much less $4s$ states. $3d$ orbitals are localized meaning that electrons are confined in a narrow space promoting short bond length.

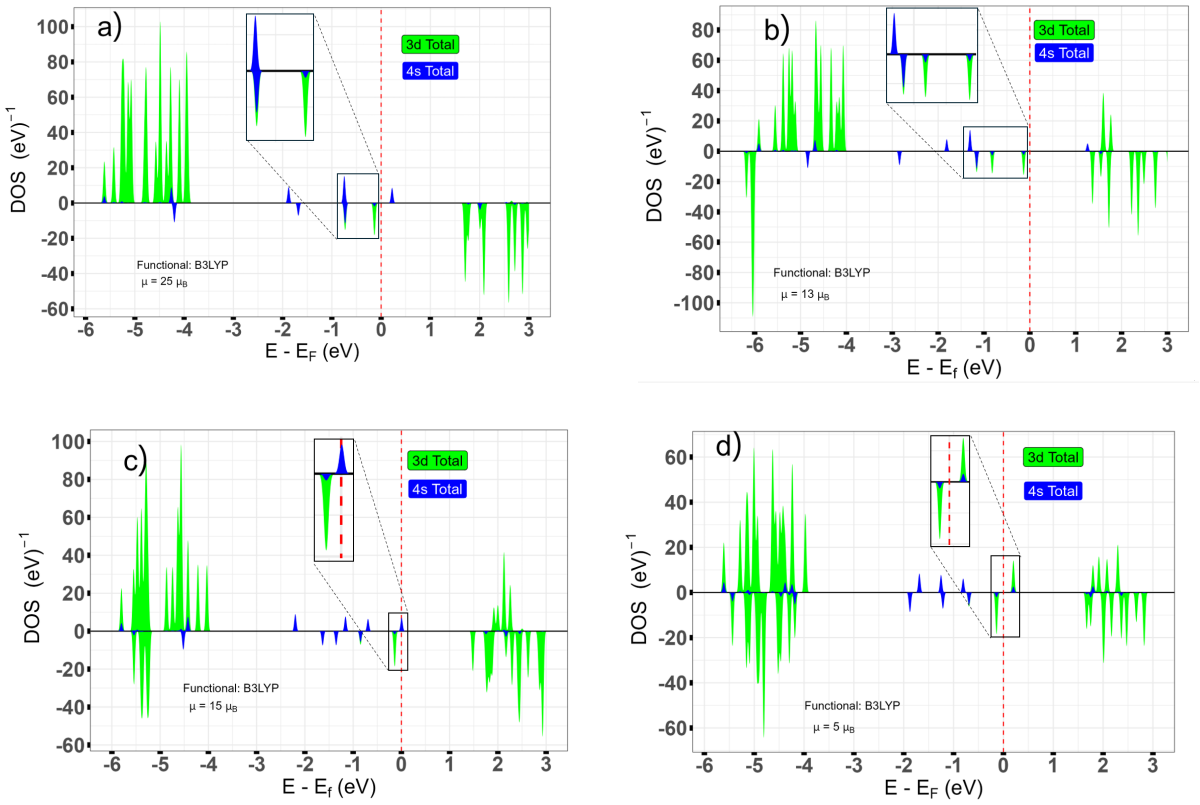

Figure 4.31: The Density of States (DOS) of Mn_5 for low energy states. The most stable state corresponds to $\mu = 25\ \mu_B$ which is a FM solution. The red dotted line presents the Fermi energy, E_F. States on the right side of E_F are unoccupied and on the left are occupied.

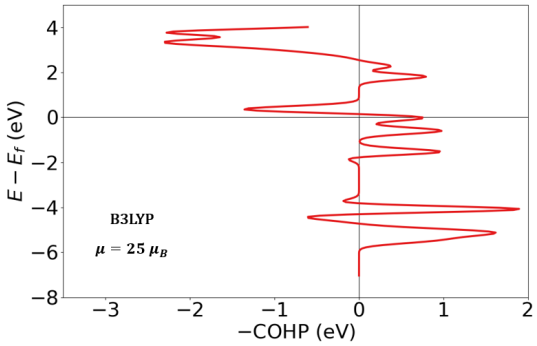

Figure 4.32: The Crystal Orbital Hamilton Populations (COHP) for Mn_5. The bonding orbitals are on the right side of each panel, meanwhile the antibonding are on the other side.

For B2PLYP functional we also got FM solution (25 μ_B) for the ground state, whereas the states 15 μ_B, 13 μ_B, and 5 μ_B are $\Delta E = 0.17\ eV$, ΔE =0.23 eV and ΔE =0.32 eV above it. Comparing these results with B3LYP, is evident that B2PLYP provides a better distinction (ΔE is greater) between one state and another.

Regarding wB97M-V, we work with this functional in the plane waves basis, and in the triple$-\zeta$ basis. First, we discuss our results in the triple$-\zeta$ basis which are depicted in Figure 4.29. This functional as well gives a FM solution for the ground state with magnetic moment 25 μ_B. The following are low energy states too with magnetic moment 15 μ_B, 13 μ_B, 5 μ_B, and 23 μ_B which are $\Delta E = 0.015\ eV$, $\Delta E = 0.033\ eV$, 0.050 eV, and, 0.12 eV above 25 μ_B. As we can see, ΔE are small values compared with the differences obtained in previous functionals. For the same functional but in the plane waves basis we have a bit different results, because we report an AF solution for the ground state with a net spin 15 μ_B (3 μ_B per atom). Other stable stables have a net spin 5 μ_B and, 25 μ_B with $\Delta E = 0.002\ eV$ and, $\Delta E = 0.066\ eV$ above the ground state. As we already mentioned, for a same functional its performance to determine the ground state may change in a different basis set. Finally, although our result 3 μ_B per atom is a bit far away from the experimental value 0.79 $\mu_B \pm 0.25\ \mu_B$ per atom (Table 1 [22]) is the only one functional which gives an AF solution for the ground state.

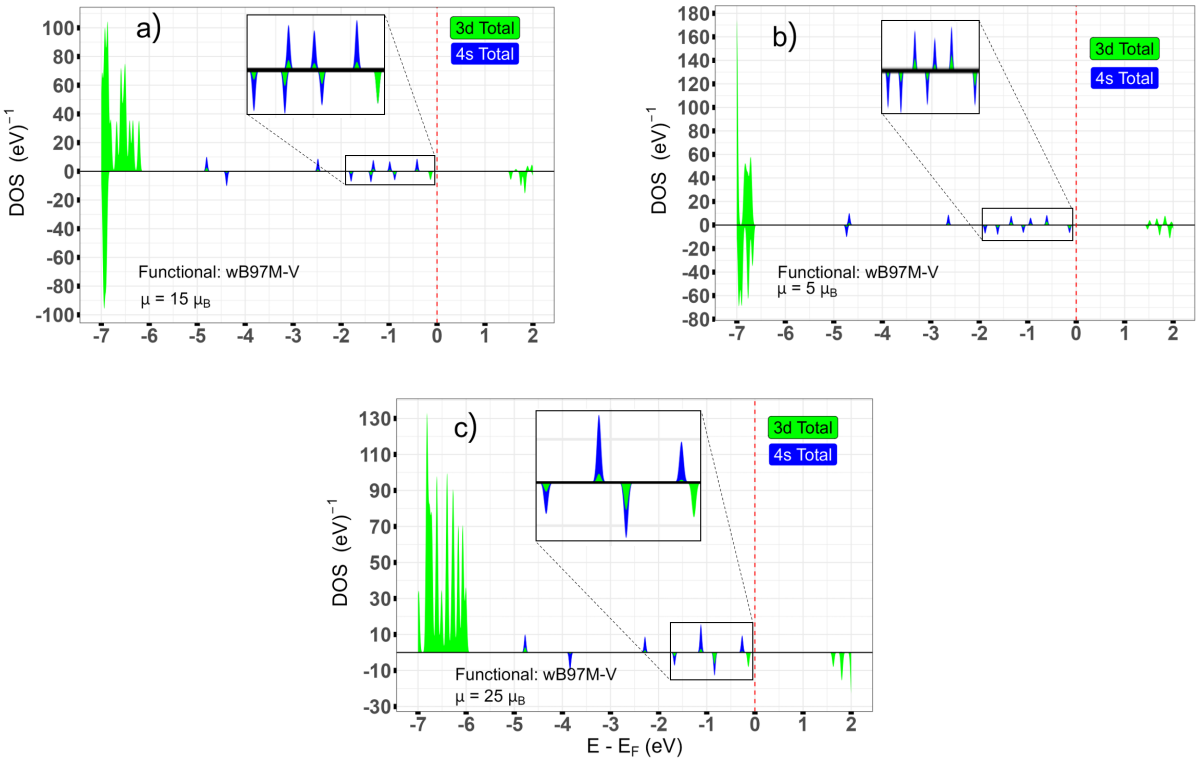

Figure 4.33: The Density of States (DOS) of Mn_5 for low energy states. The most stable state corresponds to $\mu = 15\ \mu_B$ which is an AF solution. The red dotted line presents the Fermi energy, E_F. States on the right side of E_F are unoccupied and on the left are occupied.

Now let's examine the DOS obtained with wB97M-V functional in the plane waves basis. Seeing Figure 4.33 we note that the states close to the Fermi energy are very similar for isomers ***a)*** and ***b)***. As we already mentioned, s orbitals promote large bond lengths. If we look for isomers ***a)*** and ***b)*** have less $4s$ states compared with isomer ***c)***. Thus, for the same cluster with different net magnetic moment the population of $4s$ states is relevant to determine the stability of the system. Keeping out $3d$ states (population of them close to the Fermi energy is basically the same) in our analysis, less $4s$ states favor the stability.

Referring to other computational studies, for instance Kabir *et al.* [48] employing PBE functional in VASP code found that magnetic moment 3 μ_B, 13 μ_B and 5 μ_B are the most stables. The first one

with magnetic moment 3 μ_B (0.6 μ_B per atom) is the ground state. Likewise, Bobadova-Parvanova *et al.* using PBE in NRLMOL code [57] reported 3 μ_B, 13 μ_B and 23 μ_B as stable isomers with 3 μ_B as a ground state too. Studies carried out by Jones *et al.* [64] employing NRLMOL code reported 3 μ_B as ground magnetic state for Mn_5 cluster. As we note, both works coincide with the net spin for the ground state. Our result is different although it is an AF solutions. Based on experimental measurements about Mn_5 it is very likely that the solution it is indeed AF.

Morisato *et al.* [65] discussed the concepts of collinear (CL) and non-collinear (NCL) arrangements for spins. For CL arrangement, his group also worked with the bypiramid geometry and according to their calculations the ground state is AF with a net magnetic moment 3 μ_B. The information about NCL will be provided in the next subsection.

4.4.2 Non-collinear structure for Mn_5

For the non-collinear (NCL) approach, we also considered triangular bipyramidal geometry for the initial locations of atoms. According to other studies carried out in DFT framework, the ground state energy exhibit degeneracy and it is not well defined [65]. Therefore, NCL approach can remove this degeneracy and yields to a well-define ground state [65].

According to recent experiments, the net magnetic moment is 0.79 $\mu_B \pm 0.25$ μ_B [22] for the ground state, which is a small number. The NCL approach emerged as an attempt to explain the small magnetic moment of clusters, because electron spins have more options of orientations to achieve a small magnetic moment close to zero.

Let's briefly review some studies that address the NCL spin. Han *et al.* [66] studied the material wurtzite CoO (cobalt oxide) and they showed that NCL spin structures are more stable than CL configurations. This means that collinear spin orders have higher energies than NCL configurations. On the other hand, Morisato *et al.* and his co-workers found that the ground state is a ferromagnetic collinear configuration with a net magnetic moment of 3 μ_B, however, almost degenerate with this is a NCL state [65]. The magnetic moment for the NCL spin arrangement is 5.91 μ_B, which is only $\Delta E = 0.01$ eV above the ground state.

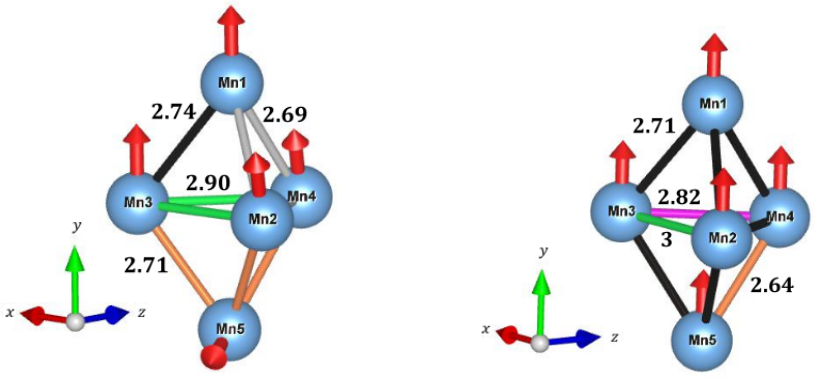

(a) ($\Delta E = 0$ eV, 18.63 μ_B) **(b)** ($\Delta E = 0.004$ eV, 25 μ_B)

Figure 4.34: Ferromagnetic and antiferromagnetic noncollinear configurations for Mn_5 and their optimal structures obtained with B3LYP functional in the plane waves basis. ΔE is the energy difference with respect to the ground state with a net magnetic moment 18.63 μ_B.

In Figure 4.34 we have two NCL isomers with 18.63 μ_B (3.72 μ_B per atom) and 25 μ_B (5 μ_B per atom) magnetic moments respectively. The energy difference between both is only $\Delta E = 0.004$ eV which is small. As we see, our antiferromagnetic NCL spin arrangement result for the ground state overestimate the value obtained experimentally by Knickelbein [22], although it is agree that the antiferromagnetic is more stable than the ferromagnetic configuration. For most of our calculations under NCL approach we notice that the initial NCL arrangement converge to collinear arrangement. Thus, using XC hybrid functional (e.g. B3LYP) NCL are not stable compared with CL arrangement. So, we conclude that NCL

approach is not need to achieve small magnetic moments to explain the experimental values.

4.5 Manganese hexamer, Mn_6

For studying this cluster we have considered two different geometries like square bipyramid and bicapped tetrahedron. The first geometry presents a high symmetry in contrast with the second one. Owing to the difference in locations of atoms, there are distinct spin arrangements. Bicapped tetrahedron offers more spin arrangements [57]. We are going to study several spin arrangements to find the ground state for each geometry and also determine which one is the most stable.

4.5.1 Square bipyramid geometry

For Mn_6, the net magnetic moments are even numbers as 0 μ_B, 2 μ_B, 4 μ_B until 30 μ_B which is the maximum value. As with the previous clusters, we employed hybrid functionals such as: B3LYP, B2PLYP, and wB97M-V. Figure 4.36 depicts the behavior of energy as a function of magnetic moment for Mn_6, employing hybrid functionals.

With B3LYP in the plane waves basis, Figure 4.35 shows several of the low energy structures and their relative energy ΔE with respect to the ground state with net magnetic moment 8 μ_B (1.33 μ_B per atom). Unfortunately, the result that we are reporting is bigger than the experimental value 0.55 μ_B $\pm$ 0.10 μ_B per atom (see Table 1 [22]), but later we will discuss why we got that result. Among the four low energy arrangements, 26 μ_B is the only one which presents FM ordering, which agrees with studies carried out by Bodadova *et al.* [57], Morisato *et al.* [65] and Kabir *et al.*[48].

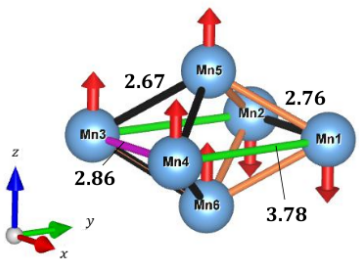

(a) ($\Delta E = 0$ eV, 8 μ_B)

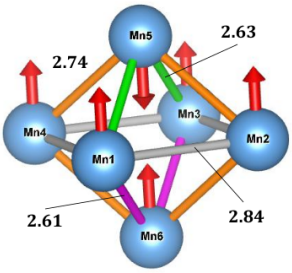

(b) ($\Delta E = 0.09$ eV, 18 μ_B)

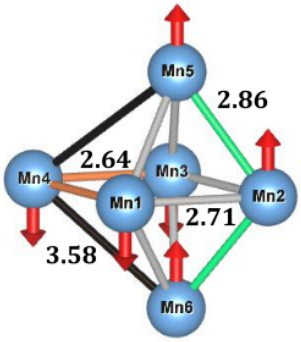

(c) ($\Delta E = 0.14$ eV, 2 μ_B)

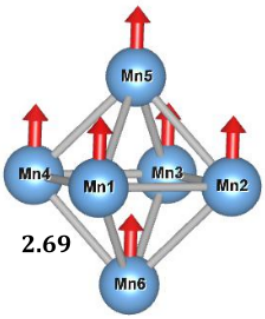

(d) (ΔE =0.16 eV, 26 μ_B)

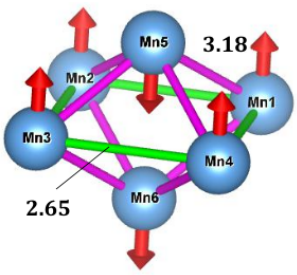

(e) (ΔE =0.17 eV, 12 μ_B)

Figure 4.35: The low energy states for Mn_6 and their optimal structures obtained with B3LYP functional in plane waves implementation. ΔE is the energy difference with respect to the ground state (8 μ_B).

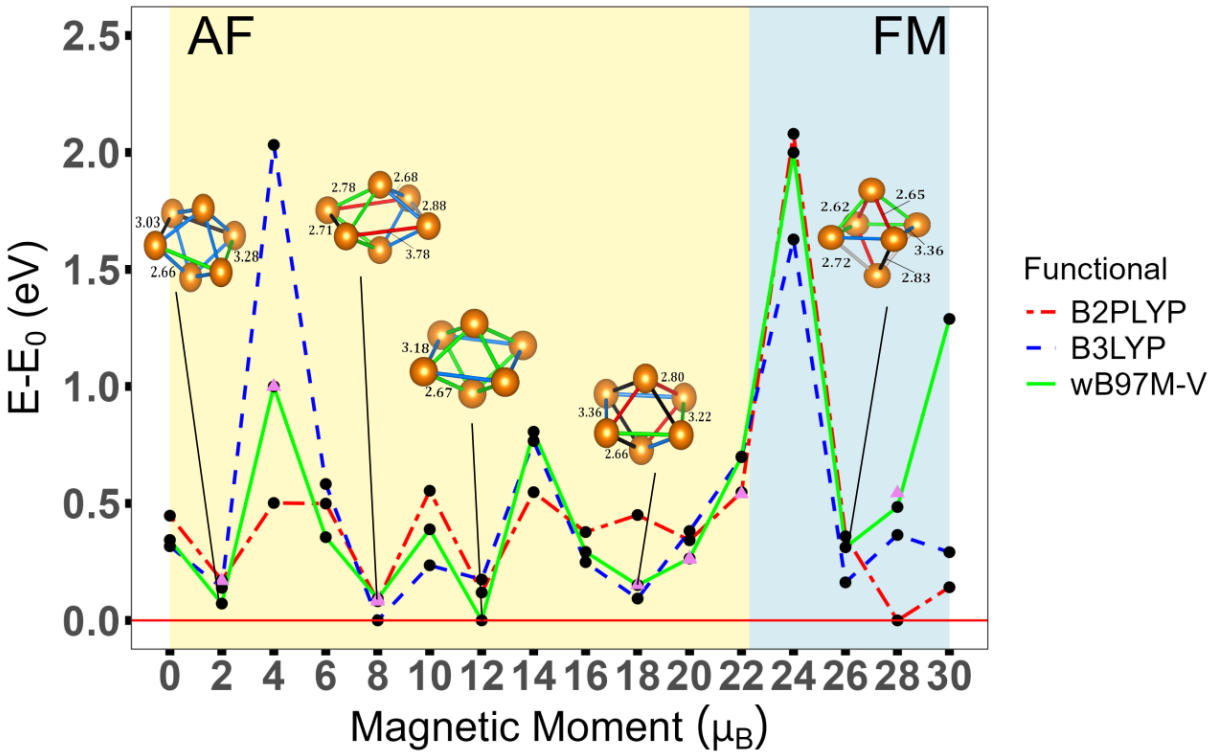

Figure 4.36: Variation of energy of Mn_6 as a function of net magnetic moment. With the plane waves basis we have B3LYP functional whereas in the triple$-\zeta$ we work with B2PLYP, and wB97M-V. In general, low energy states correspond to 2 μ_B (AF), 8 μ_B (AF), 12 μ_B (AF), 18 μ_B (AF), 26 μ_B (FM), and 28 μ_B (FM). The optimal structures were obtained with wB97M-V. ***Note*** **:** the violet triangles mean that the calculations presented saddle points during the process, which mean that the states are not stable altogether.

Regarding DOS, in Figure 4.37 there are four panels corresponding to the most stable states. One of the main features of each panel is the presence of $3d$ states very close to the Fermi energy. As we have been discussing, $3d$ states promote short bond lengths and also owing to their shape there is a strong repulsion between electrons. For the ground state (8 μ_B) at first glance we note more $4s$ states above -1 eV than $3d$ states. This promotes antiferromagnetism and longer bond lengths, which makes the cluster a bit more stable. For isomers ***b)***, ***c)***, and ***d)*** we see a reduction of $4s$ states close to the Fermi energy, which implies slightly more compact structures as seeing in Figure 4.35. For isomer ***d)*** in contrast with the other isomers, we see much $3d$ states with higher energy or many states with the same energy (high degeneracy). This effect is due to a symmetrical structure as we can see in Figure 4.35 ***d)***. The structure ot the other isomers is not symmetric therefore there are less degeneracy. The grade of splitting of the $3d$ orbitals in each panel is due to the overlapping of atomic orbitals.

If we examine the geometry for B3LYP, the regular bypiramid structure is maintained for the FM solution (isomer ***d)***) with bond length 2.69 Å. For the isomers ***a)***, ***b)*** and ***c)*** we have irregular bipyramids due to spins with opposite orientations and for the non-uniform distribution of the local magnetic moment (Table 4.7). Besides, from DOS analysis we can obtain information for bond lengths seeing the $3d$ and $4s$ states close to the Fermi energy. In Figure 4.37 ***d)*** is evident the enormous contribution of $3d$ for the bonding, which promote short bond lengths as we can appreciate in Figure 4.35 ***d)***. Regarding $4s$ states, these promote longer bond lengths and their effects can be seen for other isomers in Figure 4.35.

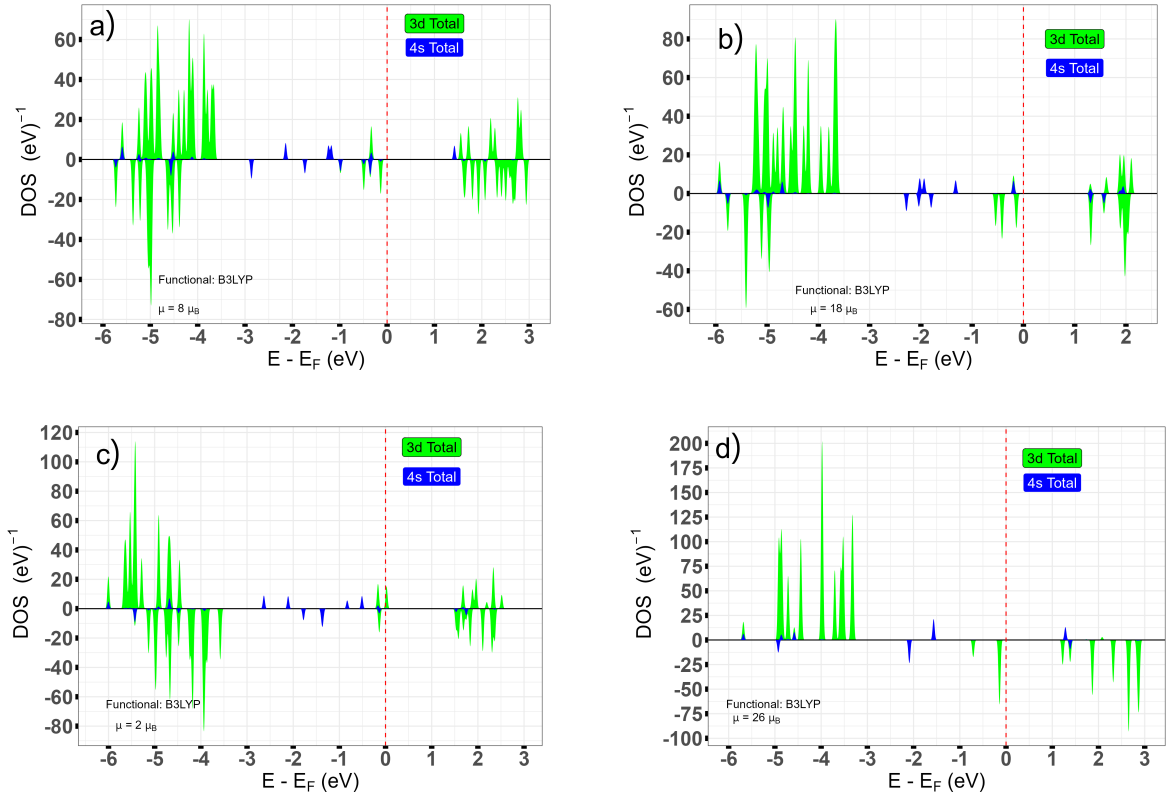

Figure 4.37: The Density of States (DOS) of Mn_6 for low energy states. The most stable state corresponds to $\mu = 5\ \mu_B$ which is an AF solution. The red dotted line represents the Fermi energy, E_F. States on the right side of E_F are unoccupied and on the left are occupied.

In the triple$-\zeta$ basis with B2PLYP, and wB97M-V functionals we got slightly different results compared to B3LYP in the plane waves basis. Figure 4.36 depicts the results obtained with B2PLYP and we found that the ground state has a net spin of 28 μ_B (4.67 μ_B per atom). Other stable states with net spin 8 μ_B, 12 μ_B, and 2 μ_B are only $\Delta E = 0.08\ eV$, $\Delta E = 0.12\ eV$, and $\Delta E = 0.17\ eV$ above the ground state. As we notice, B2PLYP gives a FM solution for Mn_6, but the other stable states are AF ordering.

Isomer	μ_1	μ_2	μ_3	μ_4	μ_5	μ_6	μ **Total**
a)	-4.9776	-4.9796	4.5544	4.5503	4.4245	4.4281	8
b)	4.5346	4.7187	4.5346	4.7184	-4.8948	4.3885	18
c)	-4.312	4.8238	-4.3147	-4.5907	5.1965	5.1972	2
d)	4.3272	4.3334	4.3395	4.3334	4.3332	4.3332	26
e)	5.1789	5.1835	5.1789	5.1743	-4.3573	-4.3583	12

Table 4.7: Local magnetic moment μ_i (in μ_B, $i = 1, 2, \cdots$) and the total magnetic moment for Mn_6 computed with the Voronoi Deformation Density method using B3LYP functional.

For wB97M-V in the triple$-\zeta$ basis, the most stable state corresponds to AF solution with a net spin 12 μ_B (2 μ_B per atom). Some of other stable states like 2 μ_B and 8 μ_B are just $\Delta E = 0.07\ eV$ and $\Delta E = 0.09\ eV$ above the ground state. In Figure 4.36 we have the optimal geometry for each stable isomer. The ground state geometry depicts a certain symmetry, where the ring of four atoms has the same bond length 3.18 Å. We want to highlight some interesting things here. If we examine the geometry of 8 μ_B obtained with B3LYP and wB97M-V both structures have similar values for the bond lengths. Generally, different structures are obtained for different functionals because each takes into account different pa-

rameters to study the same system. For instance, for 26 μ_B the optimal structures obtained with B3LYP and wB97M-V are different, as the first one has symmetric structure whereas the other does not.

4.5.2 Bicapped tetrahedron geometry

As we commented earlier, this geometry depicts certain asymmetry, and it has a more non-symmetric spin arrangement compared to the square bypiramid [57]. In Figure 4.38 we have the results employing B2PLYP in the triple$-\zeta$ basis (in ORCA code), and wB97M-V which was implemented in the plane waves (in VASP code) and in the triple$-\zeta$ basis.

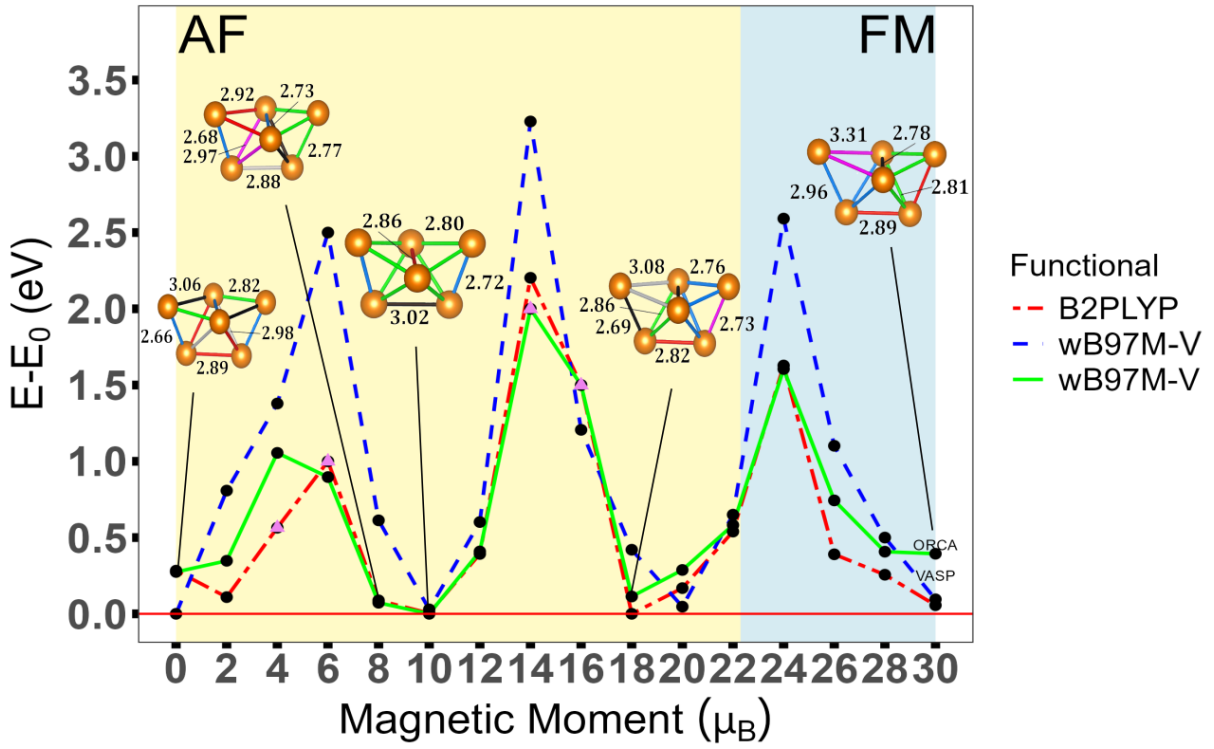

Figure 4.38: Variation of energy of Mn_6 as a function of net magnetic moment. With the plane waves basis we have wB97M-V functional whereas for triple$-\zeta$ we work with B2PLYP and wB97M-V. In general, low energy states correspond to 0 μ_B (AF), 10 μ_B (AF), 18 μ_B (AF), 20 μ_B (AF), and 30 μ_B (FM). The optimal structures were obtained with wB97M-V implemented in triple$-\zeta$ basis. ***Note :*** the violet triangles mean that the calculations presented saddle points during the process, which mean that the states are not stable altogether.

For wB97M-V in the plane waves basis we have the following low energy states 0 μ_B, 10 μ_B, 20 μ_B, and 30 μ_B as seen in Figures 4.38 and 4.39. The ground state is AF with a net spin 0 μ_B which is a bit far away from the experimental value (0.55 $\mu_B \pm 0.10$ μ_B per atom, Table 1 [22]). Bodadova-Parvanova *et al.* [57] also reported an AF solution with this geometry using PBE functional in NRLMOL code although its net spin is 2 μ_B.

The DOS analysis for each isomer in Figure 4.40 shows that the majority of states close to the Fermi energy belong to 4*s*, which is one of the features of wB97M-V as seen for previous Mn clusters. Once again, 4*s* orbital favor larger bond lengths. At first glance isomer ***a)*** has a bit more 4*s* states close to Fermi energy and its effect is seen in larger bond lengths in Figure 4.39 ***a)*** compared with other isomers. In the same way, we see that 3*d* states are more localized (range between -7 eV and -6 eV) as a consequence of large bond lengths, so atomic orbitals are less overlapped.

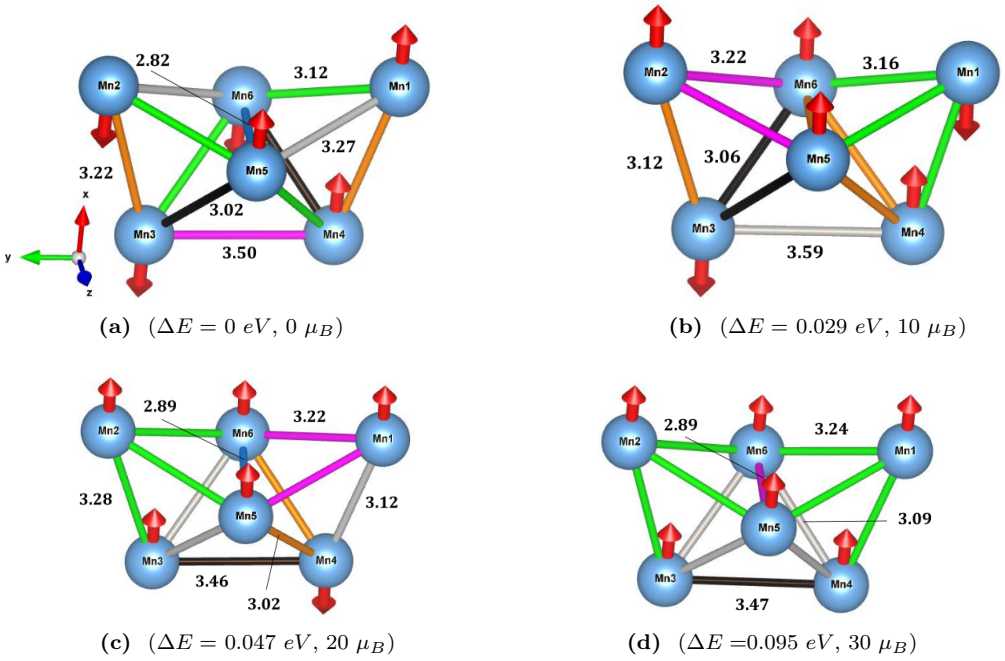

(a) ($\Delta E = 0\ eV$, $0\ \mu_B$) **(b)** ($\Delta E = 0.029\ eV$, $10\ \mu_B$)

(c) ($\Delta E = 0.047\ eV$, $20\ \mu_B$) **(d)** (ΔE =$0.095\ eV$, $30\ \mu_B$)

Figure 4.39: The low energy states for Mn_6 and their optimal structures obtained with wB97M-V functional in the plane waves basis. ΔE is the energy difference with respect to the ground state (0 μ_B).

Regarding optimal structures in Figure 4.39, the ground state has more variation of bond lengths which range between 3.02 Å − 3.50 Å owing to the different orientation of spins. Isomers ***b)***, ***c)***, and ***d)*** also depict long bond lengths. Isomer ***d)***, which is a FM solution conserved a bit more the initial structure. This behavior is explained by local magnetic moment (Table 4.8), where the individual atomic moments seem similar. In general, for FM solutions the optimal structure is pretty similar to the initial structure (before starting with calculations).

Isomer	μ_1	μ_2	μ_3	μ_4	μ_5	μ_6	μ **Total**
a)	5.0023	-5.0024	-4.9938	4.9947	4.8902	-4.8910	0
b)	-4.9414	5.0697	-4.9071	5.0188	4.8805	4.8796	10
c)	5.0868	5.0922	5.0146	-4.9396	4.8729	4.8731	20
d)	5.0926	5.0926	5.0334	5.0337	4.8741	4.8737	30

Table 4.8: Local magnetic moment μ_i (in μ_B, $i = 1, 2, \cdots$) and the total magnetic moment for Mn_6 computed with the Voronoi Deformation Density method using wB97M-V functional.

For wB97M-V in the triple$-\zeta$ basis set gives a net magnetic 10 μ_B (1.67 μ_B per atom) for the ground state. As shown in Figure 4.38, the other low energy states have a magnetic moment of 8 μ_B, 18 μ_B, 0 μ_B and 30 μ_B. The difference in energy for each mentioned isomer with respect to the ground state is $\Delta E = 0.07\ eV$, $\Delta E = 0.11\ eV$, $\Delta E = 0.27\ eV$, and $\Delta E = 0.39\ eV$ respectively. These stable states are basically the same that we reported for the same functional in the plane waves basis. As we note, difference lies in ΔE, which is direct consequence of the triple$-\zeta$ basis employed by ORCA. As we already highlight for other clusters, it seems that the basis set employed by different codes don't have a meaningful impact to determine the stable states. We mean that the same functional may gives the same local minima in any basis set. For the same functional the bonding energy, bond lengths, and the ground state may depend on the basis set, because some basis can be more accurate than others.

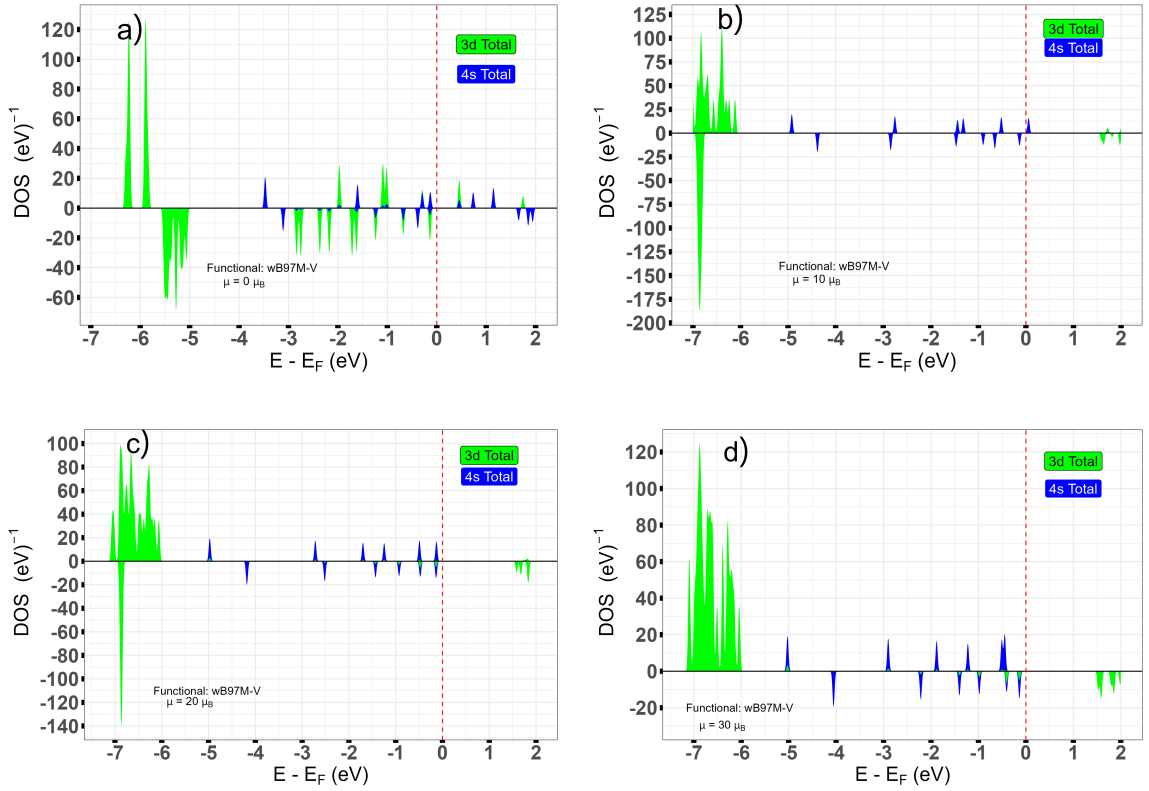

Figure 4.40: The Density of States (DOS) of Mn_6 for low energy states. The most stable state corresponds to $\mu = 0\ \mu_B$ which is an AF solution. The red dotted line represents the Fermi energy, E_F. States on the right side of E_F are unoccupied and on the left are occupied.

In Figure 4.38 there are the optimal structures for the low energy states obtained with wB97M-V functional in the triple$-\zeta$ basis. The bond lengths for the most stable state range between 2.66 Å $-$ 3.08 Å which are shorter than the results (3.02 Å $-$ 3.59 Å) obtained the same functional but in the plane waves basis (Figure 4.39 ***a***)). This is an example how different basis set employed to expand electron's wave functions could give the same local minima but may change bond lengths, bonding energy and even ground state. For instance, the ground state in the plane waves we report a net spin 0 μ_B meanwhile in the triple$-\zeta$ basis is 10 μ_B.

With B2PLYP the most stable state has a net magnetic moment 18 μ_B (3 μ_B per atom), and isomers with net spin 10 μ_B, 30 μ_B, 28 μ_B, 8 μ_B, and 2 μ_B are $\Delta E = 0.004\ eV$, $\Delta E = 0.056\ eV$, $\Delta E = 0.062\ eV$, $\Delta E = 0.088\ eV$, and $\Delta E = 0.11\ eV$ above it. ΔE between 18 μ_B and 10 μ_B is small and to pass from one state to other the temperature has to be increased to $\Delta E/k_B \approx 46$ K. For experimental measurements, temperature normally range between O K $-$ 5 K. Thus 18 μ_B and 10 μ_B cannot be considered as degenerate states. Among our results, 2 μ_B (0.33 μ_B per atom) is the only close to experimental value (0.55 $\mu_B \pm 0.10\ \mu_B$ per atom, Table 1 [22]), but it is $\Delta E = 0.11\ eV$ above the ground state and is evident that are not degenerate states too.

Among our findings, bicapped tetrahedron is more stable than square bipyramid. If we see carefully, bicapped tetrahedron arises from a distortion (breaking symmetry) of square bipyramid. In molecular system there is a theorem called Jahn-Taller Effect (JTE) which explains how geometrical distortion removes degeneracy states [67]. Distortion changes the energy of molecular orbitals allowing to electrons occupy lower energy orbitals in the molecule. Therefore, according to JTE breaking symmetry lower overall energy of the system. Based in our calculations, we saw a reduction of overall energy of each state for bicapped tetrahedron making it more stable. For example, with B2PLYP the most stable state (28 μ_B) for bipyramid is 0.062 eV above the ground state (18 μ_B) obtained for the bicapped tetrahedron. For wB97M-V functional in the triple$-\zeta$ basis the energy difference between the most stable (0 μ_B for bicapped tetrahedron and 12 μ_B for bipyramid) is 0.22 eV. Our findings are not agree with Bobadova-

Parvanova *et al.* [57] work, where they report that bipyramid structure gives lower energy states than with the bicapped tetrahedron. It is important to highlight that they use generalized gradient approximation functional (e.g. PBE) implemented in the NRLMOL code.

4.6 Manganese heptamer, Mn_7

For Mn_7 cluster we also work with two different initial structures: pentagonal bipyramid and capped octahedron. As with the hexamer, the heptamer cluster is also an example of how geometry has an impact on determination of the ground state. According to previous *ab initio* studies of Bobadova-Parvanova *et. al.* [57], these starting geometries emerge as the lowest energy geometries for Mn_7.

4.6.1 Pentagonal bipyramid geometry

Pentagonal bipyramid has a high symmetry and this feature reduces the number of relative arrangements of the individual atomic magnetic moments. However, it is still a complex system due to the number of atoms. For studying this cluster we have employed three hybrid functionals as seen in Figure 4.41.

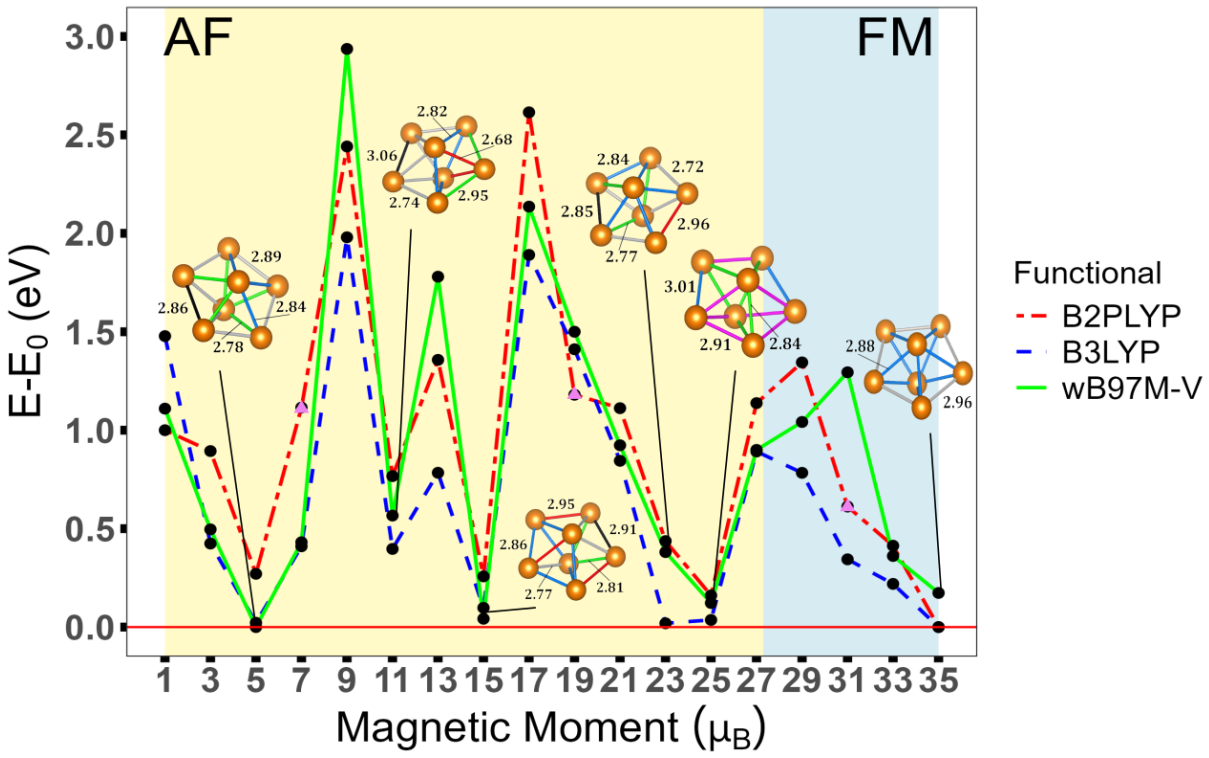

Figure 4.41: Variation of energy of Mn_7 as a function of magnetic moment. With the plane waves basis we have B3LYP functional whereas for the triple$-\zeta$ we work with B2PLYP, and wB97M-V. Low energy states correspond to 5 μ_B (AF), 11 μ_B (AF), 15 μ_B (AF), 25 μ_B (AF), and 35 μ_B (FM). The optimal structures were obtained with wB97M-V in triple$-\zeta$ basis. ***Note*** **:** the violet triangles mean that the calculations presented saddle points during the process, which mean that the states are not stable altogether.

We start the discussion with B3LYP in the plane waves basis, where we have found the ground state with a magnetic moment 35 μ_B (5 μ_B per atom). As shown in Figure 4.42 the other low energy states are: 23 μ_B, 5 μ_B, 25 μ_B, and 11 μ_B where all are antiferromagnetic solutions. The states closer to the ground state are 23 μ_B, 5 μ_B, and 25 μ_B with energy difference of $\Delta E = 0.015\ eV$, $\Delta E = 0.021\ eV$, and

0.036 eV relative to the ground state.

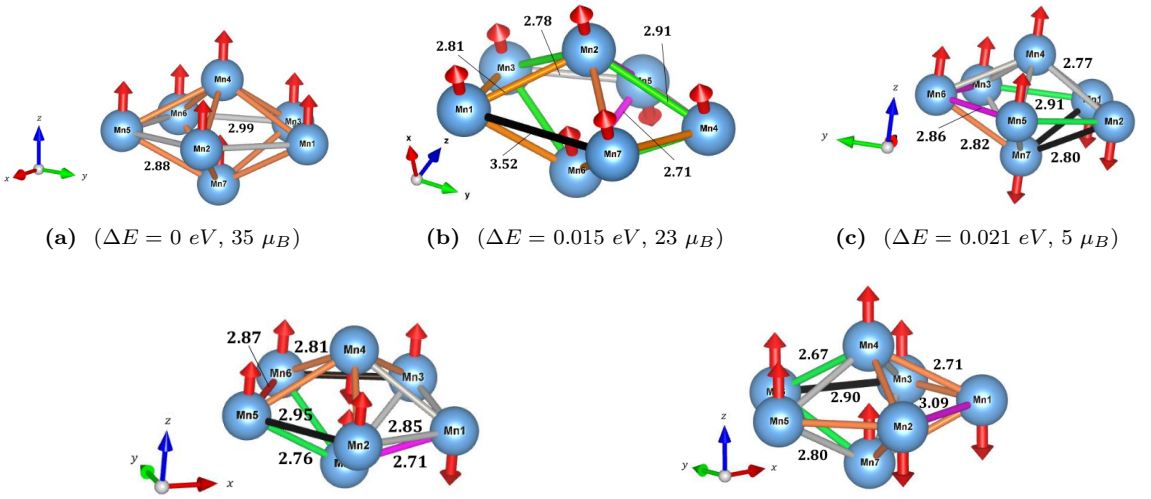

(a) ($\Delta E = 0\ eV$, 35 μ_B) **(b)** ($\Delta E = 0.015\ eV$, 23 μ_B) **(c)** ($\Delta E = 0.021\ eV$, 5 μ_B)

(d) ($\Delta E = 0.10\ eV$, 15 μ_B) **(e)** ($\Delta E = 0.40\ eV$, 11 μ_B)

Figure 4.42: The low energy states for Mn_7 and their optimal structures obtained with B3LYP functional in the plane waves basis. ΔE is the energy difference with respect to the ground state (35 μ_B).

For the isomers that appear in Figure 4.42, we note that the regular bipyramidal geometry is only conserved by 35 μ_B with bond lengths 2.88 Å and 2.99 Å. Regarding the local magnetic moment (LMM), we see that at the ends of the atoms have same LMM 4.63 μ_B and the atoms in the middle have 5.14 μ_B (Table 4.9). As we can see, the symmetry distribution of LMM also explains the symmetry of the geometry. Further, the spin of the electrons of each atom has the same orientation which also allows the symmetry for the structure. For the other isomers, we note certain asymmetry. The asymmetry presented by the other isomers, also can be verified with the asymmetry distribution of LMM (Table 4.9). If we look carefully Figure 4.42, in general short bond lengths correspond to atoms with opposite atomic magnetic moment. Likewise, for atomic moments with the same orientation, long bond lengths are obtained. In spite of some exceptions, behavior of many structures follow the Pauli exclusion principle.

Isomer	μ_1	μ_2	μ_3	μ_4	μ_5	μ_6	μ_7	μ **Total**
a)	5.1478	5.1476	5.1472	4.6291	5.148	5.1475	4.6329	35
b)	4.7854	4.4325	4.8023	4.8021	-5.0397	4.4327	4.7847	23
c)	-4.7653	-4.7641	4.9023	4.3971	4.9021	4.7592	-4.4313	5
d)	-4.7498	5.0199	5.0196	-4.5047	4.8984	4.8984	4.4183	15
e)	-5.3567	-5.361	4.5608	4.1717	4.562	4.248	4.1752	11

Table 4.9: Local magnetic moment μ_i (in μ_B, $i = 1, 2, \cdots$) and the total magnetic moment for Mn_7 computed with the Voronoi Deformation Density method using B3LYP functional.

Figure 4.43 shows the density of states for stable isomers obtained with B3LYP. For each isomer there are contributions of $4s$ and $3d$ orbitals to the magnetic moment. For isomers ***a)*** and ***d)*** there are $3d$ unoccupied states very close to the Fermi energy, which means that the band-gap is very small, therefore the cluster is classed as high conductivity. In Figure 4.43 ***a)*** we observed a greater degeneracy compared to that presented by the other isomers. Degeneracy is due to the high symmetry presented by isomer ***a)***. In contrast for isomer ***c)***, we see less degeneracy because it is asymmetric compared to isomer ***a)***. For each panel in Figure 4.43 we see a high splitting of $3d$ orbitals between -6 eV and -4 eV for each isomer, this mean the overlap of atomic orbitals. In each panel, hybridization of $s-d$ orbitals take place close to the Fermi energy. In Figure 4.43 ***a)*** there are a little bit more $s-d$ hybridization which contribute to

the stability of the cluster.

Employing B2PLYP functional the ground state corresponds to 35 μ_B (5 μ_B per atom) and the other stable states are: 25 μ_B, 15 μ_B, 5 μ_B, and 11 μ_B. For this functional, there is a clear distinction between the ground state and other stable states. The relative energy of each isomer with respect to the ground state is $\Delta E = 0.16\ eV$, $\Delta E = 0.25\ eV$, $\Delta E = 0.27\ eV$, and $\Delta E = 0.77\ eV$.

As we have seen for B3LYP, and B2PLYP, both give FM solutions for the ground state. With the next hybrid functional, wB97M-V in the triple$-\zeta$ basis we report a different result. With wB97M-V the ground state has a magnetic moment 5 μ_B (0.71 μ_B per atom). This functional provides an AF solution for the ground state and the net spin is agree with experimental measurements, 0.72 μ_B $\pm$ 0.42 μ_B per atom (see Table 1 [22]). Among the results presented in Figure 4.41, wB97M-V is the one which provides an AF solution for the ground state and agrees with experiment.

In Figure 4.41 we see the optimal structures for low energy states obtained with wB97M-V. As with B3LYP, the state with net magnetic moment 35 μ_B presents certain symmetry. If we look carefully Figure 4.41, the structure corresponding to the 5 μ_B exhibits short bond lengths. According with our experience the atomic orbitals are overlapped.

Comparing our results with other computational studies, for instance Kabir *et. al.* [48] employing the same geometry, reported 5 μ_B as the ground state and the next lowest spin ordering is 7 μ_B with a relative energy of $\Delta E = 0.09\ eV$. In addition, a similar result was obtained by Bobadova-Parvanova *et. al.* where local minima correspond to 5 μ_B, 11 μ_B and 29 μ_B [57].

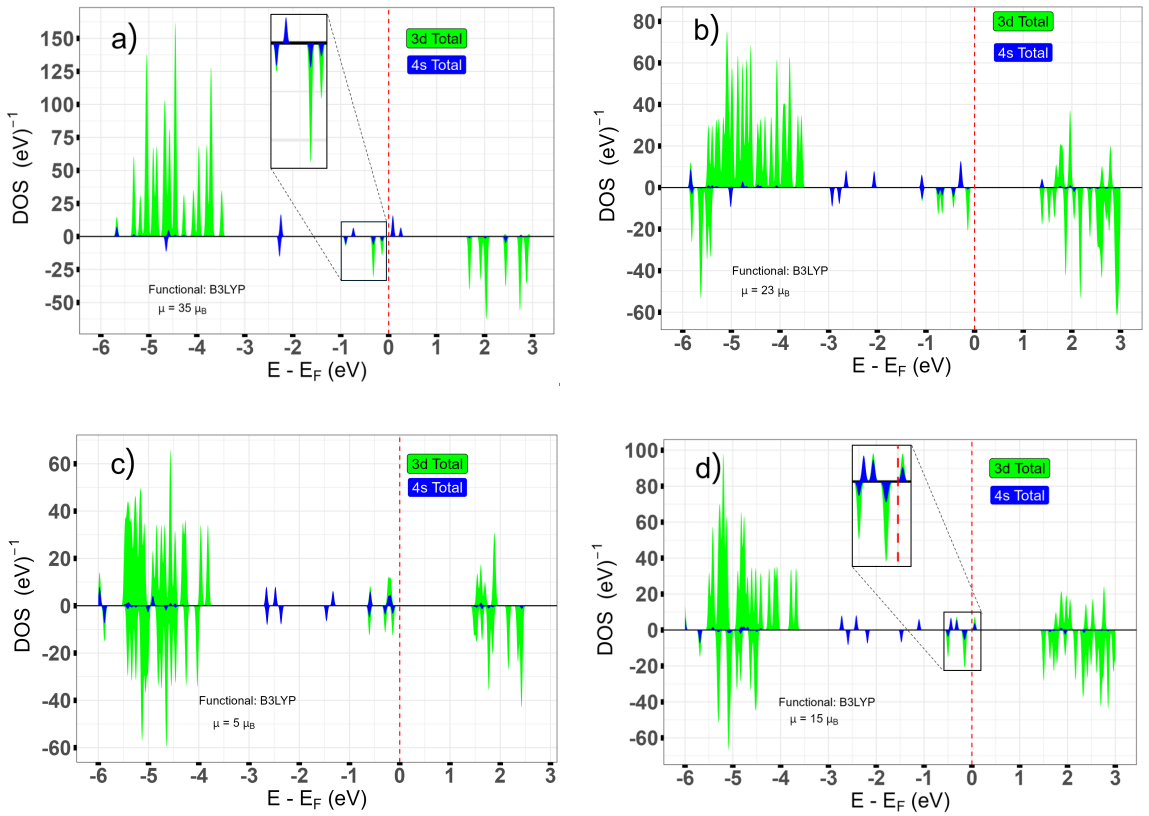

Figure 4.43: The Density of States (DOS) of Mn_7 for low energy states. The most stable state corresponds to $\mu = 35\ \mu_B$ which is a FM solution. The red dotted line presents the Fermi energy, E_F. States on the right side of E_F are unoccupied and on the left are occupied.

Among the two geometries that we study for Mn_7, the pentagonal bipyramidal is the most stable. The energy difference between the most stables state of bipyramid (35 μ_B) and capped octahedron (3

μ_B) with B3LYP is 0.096 eV. For wB97M-V in the triple$-\zeta$ basis the energy difference between the most stable states (5 μ_B for bipyramid and 15 μ_B for capped octahedron) is 0.66 eV. Our results is agree with the result reported by Bobadova-Parvanova *et al* [57], where the capped octahedron lies energetically above (0.27 eV) the bipyramid geometry. For the most stable states, Bobadova-Parvanova *et al* reported a magnetic moment 5 μ_B in bipyramid structure and 3 μ_B in capped octahedron.

4.6.2 Capped octahedron geometry

As shown in Figure 4.44, capped octahedron is an asymmetry structure compared with the previous geometry. To study Mn_7 cluster with this geometry we use the B3LYP hybrid functional in the plane waves basis. In our findings, these are the low energy states: 3 μ_B, 23 μ_B, 35 μ_B and 15 μ_B. As shown in Figure 4.44, 3 μ_B (0.43 μ_B per atom), is the state with lowest energy. Comparing with experimental results 0.72 μ_B $\pm$ 0.42 μ_B (Table 1 [22]) our result is in the range of values.

The magnetic ordering and relative energies ΔE for the stable states with respect to the ground state are shown in Figure 4.44. Comparing our result with other computational study we have that Bobadova-Parvanova *et al*. [57] reported $3\mu_B$ and $35\mu_B$ as stable isomers.

For B3LYP with the bipyramidal geometry, we found that the most stable states has a net spin 35 μ_B, while for capped octahedron geometry is 3 μ_B. As with Mn6, here we also conclude that the ground state depend on geometry. Currently is not possible to determine experimentally the geometry of small clusters. Hence the importance of our work, to shed some light on how the energy of the states is affected by the change in geometry.

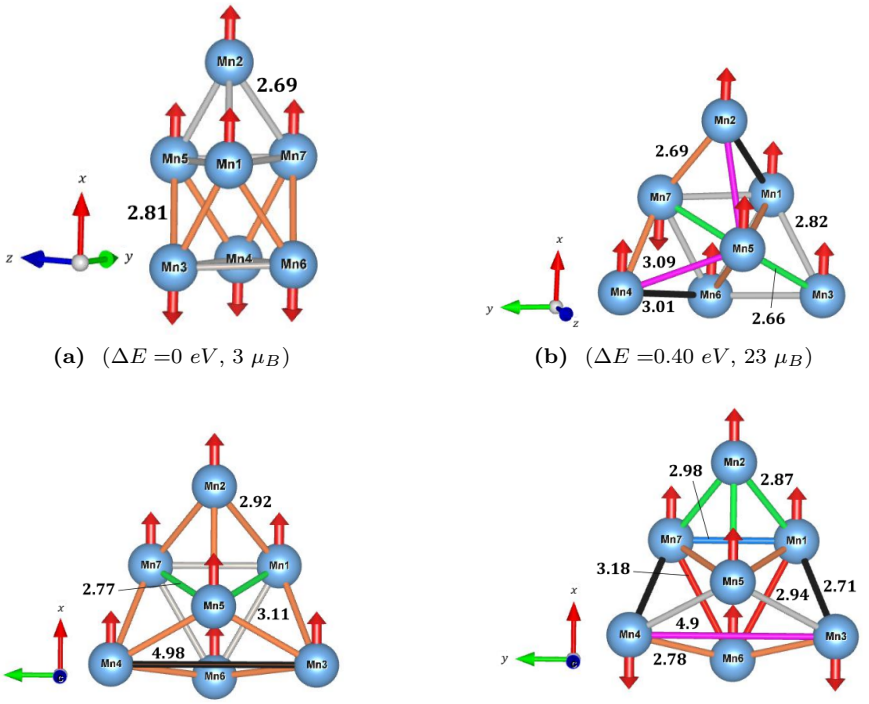

(a) (ΔE =0 eV, 3 μ_B) **(b)** (ΔE =0.40 eV, 23 μ_B)

(c) (ΔE =0.47 eV, 35 μ_B) **(d)** (ΔE =0.48 eV, 15 μ_B)

Figure 4.44: The low energy states for Mn_7 and their optimal structures obtained with B3LYP functional in the plane waves basis. ΔE is the energy difference with respect to the ground state (3 μ_B).

For 3 μ_B the bond lengths are 2.69 Å and 2.81 Å and is the isomer with the shortest bond lengths among the stable states. For the other isomers, the geometry is the same although distorted as shown in Figure 4.44. For instance, for isomer ***d)*** the bond lengths vary between 2.71 Å and 4.90 Å. The isomers ***b*** and ***d)*** are the ones which present more variations for the bond lengths.

The bond length with anti-parallel spins are generally shorter, for example in the isomer ***d)***the bond lentghs are 2.71 Å, 2.78 Å and 2.94 Å. Owing to the complexity of the system, there are exceptions. For instance, in isomer ***a)*** the distances between anti-parallel spins are greater (2.81 Å) than the distance between the parallel spins (2.69 Å).

The local magnetic moment (LMM) for each isomer is in Table 4.10. As can be seen in detail, the isomers ***b)*** and ***d)*** that have a more distorted geometry, the distribution of LMM is in general different for each atom. It is possible that this is not a general behavior of Mn clusters, where the symmetric distribution of the magnetic moment is related with the symmetry of the structure, but for our studies we are observing that.

Isomer	μ_1	μ_2	μ_3	μ_4	μ_5	μ_6	μ_7	μ **Total**
a)	4.3321	4.4468	-4.8159	-4.8158	5.3332	-4.8162	4.3359	3
b)	4.5845	4.9526	4.5518	4.9521	4.3503	4.5853	-4.9767	23
c)	4.9221	5.2368	5.2368	5.2368	4.5233	4.9221	4.922	35
d)	4.8801	4.9961	-4.6567	-4.6568	4.5299	5.0281	4.8793	15

Table 4.10: Local magnetic moment μ_i (in μ_B, $i = 1, 2, \cdots$) and the total magnetic moment for Mn_7 compued with the Voronoi Deformation Density method using B3LYP functional.

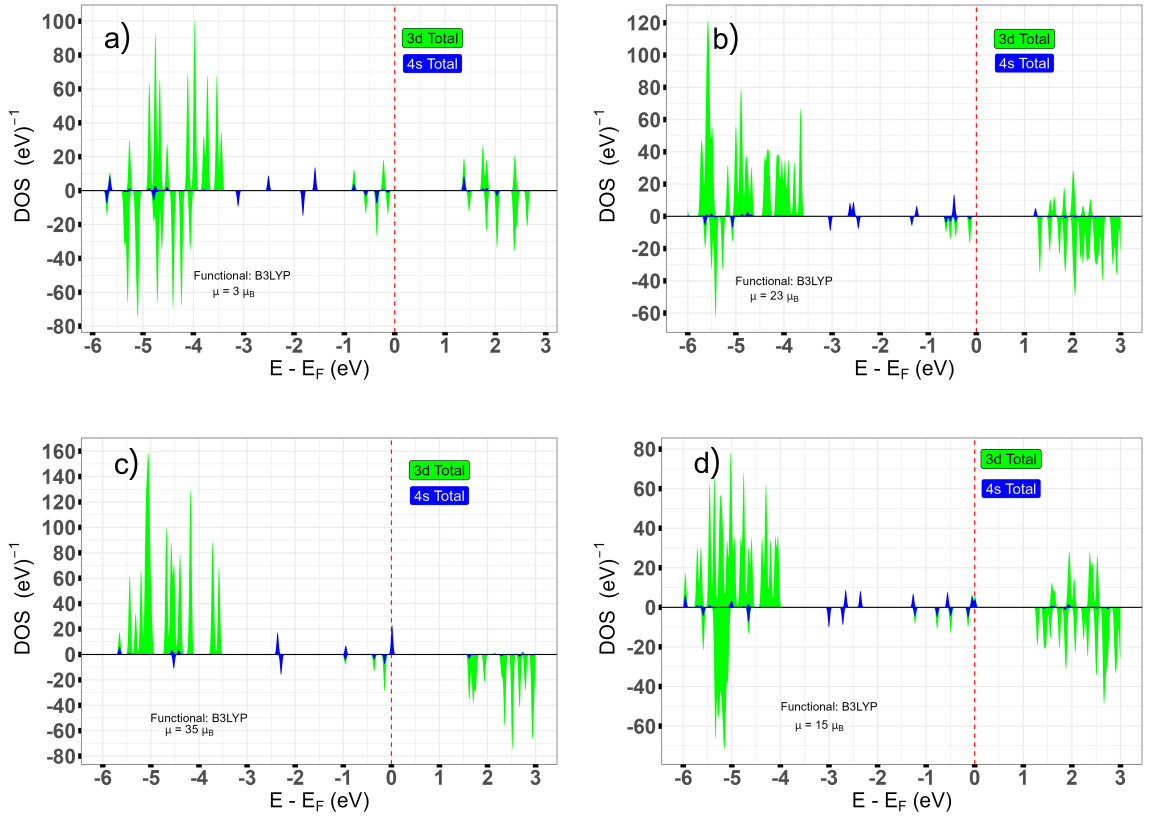

Figure 4.45: The Density of States (DOS) of Mn_7 for low energy states. The most stable states. The most stable state corresponds to $\mu = 3\ \mu_B$ which is an AF solution. The red dotted line presents the Fermi energy, E_F. States on the right side of E_F are unoccupied and on the left are occupied.

Figure 4.45 presents the DOS for the low energy states. In each panel we see $s - d$ orbital hybridization, occupied and unoccupied states with spin up and down. If we see carefully, the d states in panel

a) are more delocalized or splitted than the other DOS, owing to the short bond lengths. The same way, the presence of d states close to the Fermi energy mean that the self-interaction (SI) is a big source of error. B3LYP and other hybrid functionals reduce the SI but not remove it completely. For the ground state (isomer ***a)***) presents more d states close to the Fermi energy, and these states promote short bond lengths owing its nature. The previous statement agrees with the optimal structure in Figure 4.44 ***a)***. In addition, the $3d$ orbitals are more splitted due to the overlapped because atoms are closer.

Finally, with wB97M-V in the triple$-\zeta$ basis we report the following low energy states: 15 μ_B, 3 μ_B, 23 μ_B, and 33 μ_B. The ground state is AF ordering with a magnetic moment 15 μ_B (2.14 μ_B per atom), which is far from the experimental value (Table 1 [22]). The energy difference of the other stable states with respect to the ground state is $\Delta E = 0.005\ eV$, $\Delta E = 0.044\ eV$, and $\Delta E = 0.152\ eV$.

Chapter 5

Conclusions

In this manuscript, we carried out a first-principles study regarding the magnetic-electronic properties of Mn clusters using primarily hybrid functionals (Hartree-Fock (HF) exact exchange energy plus DFT). Besides, in DFT framework two different basis sets were used to perform calculations: plane waves and localized molecular orbitals. We compared our results with previous theoretical studies, and with the available experiment measurements.

We consider small-sized Mn clusters up to seven atoms. We begin our study with the simplest case (Mn_2) employing different kinds of functionals to treat the exchange and electron correlation (XC) effects. The type of functionals include local, semi-local and non-local functionals such as: LSDA, GGAs, meta-GGAs, hybrid functionals and doubly hybrid functionals. We have found that hybrid functionals describe better the structural and magneto-electronic properties of Mn_2. For instance, the B3LYP hybrid functional using a plane waves basis gives an antiferromagnetic ordering, with a bond length of 3.41 Å and bonding energy 0.07 eV for the ground-state. These values are in line with the experimental measurements for the magnetic ordering (antiferromagnetic [15]), bond length (3.20 Å−3.40 Å [15][21]) and bonding energy (0.13 eV ± 0.10 eV [17]). Employing other hybrid functionals such as B2PLYP, and wB97M-V using a triple$-\zeta$ basis set we also obtained the antiferromagnetic (AF) configuration for the ground state. In general, hybrid functionals (e.g., B3LYP, B2PLYP, and wB97M-V) are in agreement with the experimental evidence in the Mn_2 description, for this reason we solely use this kind of XC functionals for Mn_α ($\alpha = 3, \cdots, 7$). The main characteristic of hybrid functionals is the combination of HF exchange with a standard semi-local XC functional to treat the exchange and electron correlation effects. After careful examination, we determine that the HF configuration stabilize the magnetic ordering which is favored by the contribution of $4s$ states close to the Fermi energy. Due to the non localized nature of $s-$type orbitals, in general the $4s$ states promote long bond lengths.

For the case of Mn_3, with B3LYP and B2PLYP we found a ferromagnetic (FM) solution with 15 μ_B as net magnetic moment for the ground state, which agrees with previous computational studies (Kabir *et al.* [48], Bobadova-Parvanova *et al.* [57]) using semi-local functionals (e.g., PBE). The difference that we found between using semi-local functionals as Kabir *et al.* [48] and hybrid functionals is observed in the bond lengths. For instance, with B3LYP we found a long bond length for the ground state (2.93 Å) in contrast of more compact structure obtained with the semi-local functional (2.74 Å [48]). For wB97M-V using both plane waves, and in the triple$-\zeta$ basis set one obtained the AF solution as the most stable state with a net magnetic moment of 5 μ_B. As seen in the density of states (DOS) analysis for wB97M-V, practically it does not show $s-d$ hybridization close to the Fermi energy, instead appear solely $4s$ states. Unfortunately there are no experimental studies yet to compare with our results. Based on Mn_2 where a low spin arrangement together with long bond length are favored by hybrid functional owing to the $4s$ states close to the Fermi energy, we conjecture that antiferromagnetic arrangement (net magnetic moment 5 μ_B) is the most plausible physical result.

In the case of the tetramer structure employing B3LYP hybrid functional we found the FM arrangement (20 μ_B) as the most stable state. This result agrees with previous theoretical studies (Kabir *et al.* [48], Bobadova-Parvanova *et al.* [57]) using semi-local functionals (e.g., PBE), but unfortunately there are no experimental studies which to verify this result with. Using the wB97M-V functional and a plane waves, and with a triple$-\zeta$ basis, we found an AF solution (net magnetic moment 0 μ_B) for the ground

state. The DOS analysis for the ground state with the wB97M-V functional shows very little $s-d$ hybridization. As with Mn_2 and Mn_3 with the wB97M-V hybrid functional due to the greater presence of $4s$ states close to the Fermi energy, the antiferromagnetism is stabilizes. Thus, based on the same line of behavior depicted by previous stable states of clusters (Mn_2 and Mn_3), we conjecture that AF solution given by wB97M-V functional gives the correct physical trend.

Mn_5 is a remarkable case. We study this cluster using collinear (CL) and non-collinear (NCL) approaches. For the first approach, with the wB97M-V hybrid functional and a plane waves basis set we found an AF solution having magnetic moment 3 μ_B per atom for the ground state magnetic configuration. According to the experimental measurements 0.79 μ_B $\pm$ 0.25 μ_B [22] is the magnetic moment per atom for the ground state. Although our result slightly overestimates the magnetic moment for the ground state, it has a good agreement with the results of previous *ab initio* works (Kabir *et al.* [48], Bobadova-Parvanova *et al.* [57]) AF solution. In addition, the experimental results encourage that the only possible solution has to be AF. In the DOS analysis with the wB97M-V XC functional, we see that the hybridization of the $s-d$ orbitals is becoming more relevant for the bonds due to its proximity to the Fermi energy. The hybridization means atomic orbitals are overlapped, which in general imply short bond lengths and therefore more compact structures as seen for Mn_5 compared with previous smaller clusters. In attempt to have another standpoint of view, we performed calculations considering NCL spin arrangements. We obtained an antiferromagnetic NCL spin configuration which is slightly more stable than the ferromagnetic solution, although its magnetic moment (3.72 μ_B per atom) turns to be quite significant and overestimate the experimental value for the ground state.

For Mn_6 we considered two geometries. For the square bipyramid, the B3LYP functional using a plane waves basis and the wB97M-V functional in localized molecular orbitals (triple$-\zeta$) give an AF solution for the ground state having 1.33 μ_B and 2 μ_B per atom respectively. For the bicapped tetrahedron structure, using the wB97M-V functional and considering a plane waves basis set we found that the most stable state has a net magnetic moment of 0 μ_B. For both structures, we obtain AF solutions for the ground state although the magnetic moments overestimate or underestimate the experimental value of 0.55 μ_B $\pm$ 0.10 μ_B per atom [22]. Comparing both structures, the bicapped tetrahedron gives lower energy values than the bipyramid structure, which means that this is most stable geometry. Interestingly, our results respect to the stable structure using hybrid functionals are different than reported by previous *ab initio* studies (Bobadova-Parvanova *et al.* [57]) using semi-local XC functionals. Thus, we have that the treatment of exchange and electron correlation effects has a direct implication to determine the most stable structure. Thus, we conjecture the bicapped tetrahedron as the optimal structure. In this moment is not possible to determine experimentally the structure of clusters as well the type of bonding promote compact structures.

Finally for the heptamer (Mn_7) we considered the pentagonal bypiramid and the capped octahedron as the potential low-lying structures. According to our findings using the B3LYP functional and a plane waves basis set, and the wB97M-V functional in the triple$-\zeta$ basis, pentagonal bypiramid is the most stable. Our result also agrees with previous *ab initio* studies (Kabir *et al.* [48], Bobadova-Parvanova *et al.* [57]) about the most stable structure. Although we obtained the same result for the stable structure with previous studies (using semi-local functionals, e.g., PBE), the bond lengths with hybrid functionals (e.g., wB97M-V) are larger than obtained with semi-local functionals. In our findings, the wB97M-V hybrid functional gives an AF solution for the ground state with a magnetic moment 0.71 μ_B per atom in accordance with the experimental measurement (0.72 μ_B $\pm$ 0.42 μ_B per atom [22]).

The following are general conclusions upon employing hybrid functionals to treat the exchange and electron correlation effects in the study of the electronic and magnetic properties of small Mn clusters (Mn_α, $\alpha = 2, \cdots, 7$): (i) the hybrid functionals (e.g., B3LYP, wB97M-V) tend to give larger bond lengths compared with the ones obtained using semi-local XC functionals (e.g., PBE) reported in previous *ab initio* studies (Kabir *et al.* [48], Bobadova-Parvanova *et al.* [57]). (ii) The wB97M-V functional for most cases gives AF solutions for the ground state. This is a consequence of $4s$ states close to the Fermi energy seen in DOS analysis, which promote antiferromagnetism. (iii) The two different methodologies (plane waves basis and localized molecular orbitals) of the DFT most of the cases give the same local minima for each cluster. Only the ground state may be different in each methodology.

Bibliography

[1] S. Posysaev, "Applications of density functional theory for modeling metal-semiconductor contacts, reaction pathways, and calculating oxidation states," 2018. [Online]. Available: https://api.semanticscholar.org/CorpusID:139463807

[2] J. M. L. Martin and G. Santra, "Empirical double-hybrid density functional theory: A 'third way' in between wft and dft," *Israel Journal of Chemistry*, vol. 60, no. 8-9, pp. 787–804, 2020. [Online]. Available: https://onlinelibrary.wiley.com/doi/abs/10.1002/ijch.201900114

[3] R. F. W. Bader, "Atoms in molecules," *Accounts of Chemical Research*, vol. 18, no. 1, pp. 9–15, 1985. [Online]. Available: https://doi.org/10.1021/ar00109a003

[4] C. W. David, "Voronoi polyhedra and the docking problem," in *Symmetry*, I. HARGITTAI, Ed. Pergamon, 1986, pp. 763–766. [Online]. Available: https://www.sciencedirect.com/science/article/pii/B9780080339863500537

[5] D. C. Young, *Computational Chemistry: A Practical Guide for Applying Techniques to Real World Problems*, 1st ed. John Wiley and Sons, Inc, 2001.

[6] M. Råsander, "A theoretical perspective on the chemical bonding and structure of transition metal carbides and multilayers," Ph.D. dissertation, 01 2010.

[7] J. Hafner, "Ab-initio simulations of materials using vasp: Density-functional theory and beyond," *Journal of Computational Chemistry*, vol. 29, no. 13, pp. 2044–2078, 2008. [Online]. Available: https://onlinelibrary.wiley.com/doi/abs/10.1002/jcc.21057

[8] J. M. del Campo, J. L. Gázquez, S. B. Trickey, and A. Vela, "Non-empirical improvement of PBE and its hybrid PBE0 for general description of molecular properties," *The Journal of Chemical Physics*, vol. 136, no. 10, p. 104108, 03 2012. [Online]. Available: https://doi.org/10.1063/1.3691197

[9] F. Abu-Awwad and P. Politzer, "Variation of parameters in becke-3 hybrid exchange-correlation functional," *Journal of Computational Chemistry*, vol. 21, pp. 227–238, 02 2000.

[10] F. Neese, "The orca program system," *WIREs Computational Molecular Science*, vol. 2, no. 1, pp. 73–78, 2012. [Online]. Available: https://wires.onlinelibrary.wiley.com/doi/abs/10.1002/wcms.81

[11] F. Neese, F. Wennmohs, U. Becker, and C. Riplinger, "The ORCA quantum chemistry program package," *The Journal of Chemical Physics*, vol. 152, no. 22, p. 224108, 06 2020. [Online]. Available: https://doi.org/10.1063/5.0004608

[12] L. A. Dobrzański, "Significance of materials science for the future development of societies," *Journal of Materials Processing Technology*, vol. 175, no. 1, pp. 133–148, 2006. [Online]. Available: https://www.sciencedirect.com/science/article/pii/S0924013605003857

[13] D. Shekhawat, A. Singh, A. Bhardwaj, and A. Patnaik, "A short review on polymer, metal and ceramic based implant materials," *IOP Conference Series: Materials Science and Engineering*, vol. 1017, no. 1, p. 012038, jan 2021. [Online]. Available: https://dx.doi.org/10.1088/1757-899X/1017/1/012038

[14] J. Jeevanandam, A. Barhoum, S. Chan, Yen San, A. Dufresne, and M. Danquah, "Review on nanoparticles and nanostructured materials: History, sources, toxicity, and regulations," *Beilstein Journal of Nanotechnology*, vol. 9, pp. 1050 – 1074, 03 2018.

[15] C. A. Baumann, R. J. Van Zee, S. V. Bhat, and J. Weltner, W., "ESR of Mn2 and Mn5 molecules in rare-gas matricesa)," *The Journal of Chemical Physics*, vol. 78, no. 1, pp. 190–199, 01 1983. [Online]. Available: https://doi.org/10.1063/1.444540

[16] M. Cheeseman, R. J. Van Zee, H. L. Flanagan, and J. Weltner, W., "Transition-metal diatomics: Mn2, Mn+2, CrMn," *The Journal of Chemical Physics*, vol. 92, no. 3, pp. 1553–1559, 02 1990. [Online]. Available: https://doi.org/10.1063/1.458086

[17] A. Ivanov, T. Ghosh, E. Jónsson, and H. Jonsson, "Mn dimer can be described accurately with density functional calculations when self-interaction correction is applied," *The journal of physical chemistry letters*, vol. 12, pp. 4240–4246, 04 2021.

[18] J. Mejía-López, A. H. Romero, M. E. Garcia, and J. L. Morán-López, "Understanding the elusive magnetic behavior of manganese clusters," *Phys. Rev. B*, vol. 78, p. 134405, Oct 2008. [Online]. Available: https://link.aps.org/doi/10.1103/PhysRevB.78.134405

[19] A. Kant, S. Lin, and B. Strauss, "Dissociation Energy of Mn2," *The Journal of Chemical Physics*, vol. 49, no. 4, pp. 1983–1985, 08 1968. [Online]. Available: https://doi.org/10.1063/1.1670350

[20] G. Ludwig, H. Woodbury, and R. Carlson, "Spin resonance of deep level impurities in germanium and silicon," *Journal of Physics and Chemistry of Solids*, vol. 8, p. 490, 1959. [Online]. Available: https://www.sciencedirect.com/science/article/pii/002236975990397X

[21] C. Huang, J. Zhou, K. Deng, E. Kan, and P. Jena, "Effect of coulomb correlation on the magnetic properties of mn clusters," *The Journal of Physical Chemistry A*, vol. 122, no. 17, pp. 4350–4356, 2018, pMID: 29668279. [Online]. Available: https://doi.org/10.1021/acs.jpca.8b00540

[22] M. B. Knickelbein, "Magnetic ordering in manganese clusters," *Phys. Rev. B*, vol. 70, p. 014424, Jul 2004. [Online]. Available: https://link.aps.org/doi/10.1103/PhysRevB.70.014424

[23] B. Cullity and C. Graham, *Introduction to magnetic materials*, 2nd ed. IEE Press Editorial Board and Wiley, 2009.

[24] D. J. Griffiths, *Introduction to Quantum Mechanics*, 1st ed. Prentice Hall, Inc., 1995.

[25] P. Ruiz-Díaz, J. L. Ricardo-Chávez, J. Dorantes-Dávila, and G. M. Pastor, "Magnetism of small cr clusters: Interplay between structure, magnetic order, and electron correlations," *Phys. Rev. B*, vol. 81, p. 224431, Jun 2010. [Online]. Available: https://link.aps.org/doi/10.1103/PhysRevB.81.224431

[26] W. Koch and M. Holthausen, *A Chemist's Guide to Density Functional Theory*, 2nd ed. Wiley-VCH, 2000.

[27] G. Grosso and G. Parravicini, "Solid state physics," *Academic Press, Elsevier*, 2014.

[28] F. Giustino, *Materials modelling using density functional theory : properties and predictions*, 1st ed. Oxford University Press, 2014.

[29] A. Szabo and N. S. Ostlund, *Modern Quantum Chemestry: Introduction to Advanced Electronic Structure Theory*, 1st ed. Dover Publications, Inc., 1982.

[30] I. N. Levine, *Quantum Chemistry*, 7th ed. Pearson Education, New York, 2014.

[31] R. M. Martin, *Electronic Structure: Basic Theory and Practical Methods*, 2nd ed. Cambridge University Press, 2020.

[32] D. Feil, "The molecular electron density distribution. meeting place of x-ray diffraction and quantum chemistry intermediate between theory and experiment," *Journal of Molecular Structure: THEOCHEM*, vol. 255, pp. 221–239, 1992. [Online]. Available: https://www.sciencedirect.com/science/article/pii/016612809285012A

[33] T. van Mourik, M. Bühl, and M.-P. Gaigeot, "Density functional theory across chemistry, physics and biology," *Philosophical Transactions of the Royal Society A: Mathematical, Physical and Engineering Sciences*, vol. 372, no. 2011, p. 20120488, 2014. [Online]. Available: https://royalsocietypublishing.org/doi/abs/10.1098/rsta.2012.0488

[34] S. Hamel, P. Duffy, M. E. Casida, and D. R. Salahub, "Kohn–sham orbitals and orbital energies: fictitious constructs but good approximations all the same," *Journal of Electron Spectroscopy and Related Phenomena*, vol. 123, no. 2, pp. 345–363, 2002, determination of cross-sections and momentum profiles of atoms, molecules and condensed matter. [Online]. Available: https://www.sciencedirect.com/science/article/pii/S0368204802000324

[35] J. P. Perdew and K. Schmidt, "Jacob's ladder of density functional approximations for the exchange-correlation energy," *AIP Conference Proceedings*, vol. 577, no. 1, pp. 1–20, 07 2001. [Online]. Available: https://doi.org/10.1063/1.1390175

[36] J. Tao, J. P. Perdew, V. N. Staroverov, and G. E. Scuseria, "Climbing the density functional ladder: Nonempirical meta–generalized gradient approximation designed for molecules and solids," *Phys. Rev. Lett.*, vol. 91, p. 146401, Sep 2003. [Online]. Available: https://link.aps.org/doi/10.1103/PhysRevLett.91.146401

[37] J. P. Perdew, K. Burke, and M. Ernzerhof, "Generalized gradient approximation made simple," *Phys. Rev. Lett.*, vol. 77, pp. 3865–3868, Oct 1996. [Online]. Available: https://link.aps.org/doi/10.1103/PhysRevLett.77.3865

[38] S. Lehtola and M. A. L. Marques, "Meta-local density functionals: A new rung on jacob's ladder," *Journal of Chemical Theory and Computation*, vol. 17, no. 2, pp. 943–948, 2021, pMID: 33502183. [Online]. Available: https://doi.org/10.1021/acs.jctc.0c01147

[39] J. P. Perdew, S. Kurth, A. c. v. Zupan, and P. Blaha, "Accurate density functional with correct formal properties: A step beyond the generalized gradient approximation," *Phys. Rev. Lett.*, vol. 82, pp. 2544–2547, Mar 1999. [Online]. Available: https://link.aps.org/doi/10.1103/PhysRevLett.82.2544

[40] A. D. Becke, "A new mixing of Hartree–Fock and local density-functional theories," *The Journal of Chemical Physics*, vol. 98, no. 2, pp. 1372–1377, 01 1993. [Online]. Available: https://doi.org/10.1063/1.464304

[41] A. Becke, "Correlation energy of an inhomogeneous electron gas: A coordinate-space model," *The Journal of Chemical Physics*, vol. 88, no. 2, pp. 1053–1062, 01 1988. [Online]. Available: https://doi.org/10.1063/1.454274

[42] J. P. Perdew and Y. Wang, "Accurate and simple analytic representation of the electron-gas correlation energy," *Phys. Rev. B*, vol. 45, pp. 13 244–13 249, Jun 1992. [Online]. Available: https://link.aps.org/doi/10.1103/PhysRevB.45.13244

[43] I. Y. Zhang and X. Xu, "On the top rung of jacob's ladder of density functional theory: Toward resolving the dilemma of sie and nce," *WIREs Computational Molecular Science*, vol. 11, no. 1, p. e1490, 2021. [Online]. Available: https://wires.onlinelibrary.wiley.com/doi/abs/10.1002/wcms.1490

[44] G. Santra, R. Calinsky, and J. M. L. Martin, "Benefits of range-separated hybrid and double-hybrid functionals for a large and diverse data set of reaction energies and barrier heights," *The Journal of Physical Chemistry A*, vol. 126, no. 32, pp. 5492–5505, 2022, pMID: 35930677. [Online]. Available: https://doi.org/10.1021/acs.jpca.2c03922

[45] G. Sun, J. Kürti, P. Rajczy, M. Kertesz, J. Hafner, and G. Kresse, "Performance of the vienna ab initio simulation package (vasp) in chemical applications," *Journal of Molecular Structure: THEOCHEM*, vol. 624, no. 1, pp. 37–45, 2003. [Online]. Available: https://www.sciencedirect.com/science/article/pii/S0166128002007339

[46] J. Hafner and G. Kresse, "The vienna ab-initio simulation program vasp: An efficient and versatile tool for studying the structural, dynamic, and electronic properties of materials," 01 1997.

[47] T. C. Kirill Okhotnikov and S. Cadars, "Supercell program: a combinatorial structure-generation approach for the local-level modeling of atomic substitutions and partial occupancies in crystals," *Journal of Cheminformatics*, vol. 8, 03 2016. [Online]. Available: https://doi.org/10.1186/s13321-016-0129-3

[48] M. e. a. Kabir, "Structure, electronic properties, and magnetic transition in manganese clusters," *Phys. Rev. B*, vol. 73, p. 224439, Jun 2006. [Online]. Available: https://link.aps.org/doi/10.1103/PhysRevB.73.224439

[49] M. Gruber, G. Heimel, L. Romaner, J.-L. Brédas, and E. Zojer, "First-principles study of the geometric and electronic structure of au_{13} clusters: Importance of the prism motif," *Phys. Rev. B*, vol. 77, p. 165411, Apr 2008. [Online]. Available: https://link.aps.org/doi/10.1103/PhysRevB.77.165411

[50] P. E. Blöchl, "Projector augmented-wave method," *Phys. Rev. B*, vol. 50, pp. 17 953–17 979, Dec 1994. [Online]. Available: https://link.aps.org/doi/10.1103/PhysRevB.50.17953

[51] C. Rostgaard, "The projector augmented-wave method," Ph.D. dissertation, 2010.

[52] G. Henkelman, A. Arnaldsson, and H. Jónsson, "A fast and robust algorithm for bader decomposition of charge density," *Computational Materials Science*, vol. 36, no. 3, pp. 354–360, 2006. [Online]. Available: https://www.sciencedirect.com/science/article/pii/S0927025605001849

[53] G. M. Pastor, J. Dorantes-Dávila, and K. H. Bennemann, "Size and structural dependence of the magnetic properties of small 3d-transition-metal clusters," *Phys. Rev. B*, vol. 40, pp. 7642–7654, Oct 1989. [Online]. Available: https://link.aps.org/doi/10.1103/PhysRevB.40.7642

[54] C. Fonseca Guerra, J.-W. Handgraaf, E. J. Baerends, and F. M. Bickelhaupt, "Voronoi deformation density (vdd) charges: Assessment of the mulliken, bader, hirshfeld, weinhold, and vdd methods for charge analysis," *Journal of Computational Chemistry*, vol. 25, no. 2, pp. 189–210, 2004. [Online]. Available: https://onlinelibrary.wiley.com/doi/abs/10.1002/jcc.10351

[55] M. Dolg, "Effective core potential," *Modern Methods and Algoritms of Quantum Chemistry, Proceesings, Second Edition, J. Grotendorst*, vol. 3, pp. 507–540, 01 2000.

[56] C. Huang, J. Zhou, K. Deng, E. Kan, and P. Jena, "Effect of coulomb correlation on the magnetic properties of mn clusters," *The Journal of Physical Chemistry A*, vol. 122, no. 17, pp. 4350–4356, 2018, pMID: 29668279. [Online]. Available: https://doi.org/10.1021/acs.jpca.8b00540

[57] P. Bobadova-Parvanova, K. Jackson, S. Srinivas, and M. Horoi, "Structure, bonding, and magnetism in manganese clusters," *The Journal of chemical physics*, vol. 122, p. 14310, 02 2005.

[58] P. D. Mezei, G. I. Csonka, and M. Kállay, "Simple modifications of the scan meta-generalized gradient approximation functional," *Journal of Chemical Theory and Computation*, vol. 14, no. 5, pp. 2469–2479, 2018, pMID: 29565589. [Online]. Available: https://doi.org/10.1021/acs.jctc.8b00072

[59] S. Yamanaka, T. Ukai, K. Nakata, R. Takeda, M. Shoji, T. Kawakami, T. Takada, and K. Yamaguchi, "Density functional study of manganese dimer," *International Journal of Quantum Chemistry*, vol. 107, no. 15, pp. 3178–3190, 2007. [Online]. Available: https://onlinelibrary.wiley.com/doi/abs/10.1002/qua.21441

[60] T. J. Vydrov, 0. A. ; Van Voordhis, "The dft-nl dispersion correction," *Chem. Phys*, 2010.

[61] S. J. Hujo, W.; Grime, "The dft-nl dispersion correction," *Chem. Theory Comput.*, 2011.

[62] F. Weigned and R. Ahlrichs, "Basis df2-tzvpp," *Phys. Chem.*, 2005.

[63] F. Weigned, "Basis df2/j," *Phys. Chem.*, 2006.

[64] N. O. Jones, S. N. Khanna, T. Baruah, and M. R. Pederson, "Classical stern-gerlach profiles of mn_5 and mn_6 clusters," *Phys. Rev. B*, vol. 70, p. 045416, Jul 2004. [Online]. Available: https://link.aps.org/doi/10.1103/PhysRevB.70.045416

[65] T. Morisato, S. N. Khanna, and Y. Kawazoe, "First-principles study of the onset of noncollinearity in mn_n clusters: Magnetic arrangements in mn_5 and mn_6," *Phys. Rev. B*, vol. 72, p. 014435, Jul 2005. [Online]. Available: https://link.aps.org/doi/10.1103/PhysRevB.72.014435

[66] M. J. Han, H.-S. Kim, D. G. Kim, and J. Yu, "Collinear and noncollinear spin ground state of wurtzite coo," *Phys. Rev. B*, vol. 87, p. 184432, May 2013. [Online]. Available: https://link.aps.org/doi/10.1103/PhysRevB.87.184432

[67] R. Freitag and J. Conradie, "Understanding the jahn–teller effect in octahedral transition-metal complexes: A molecular orbital view of the mn(-diketonato)3 complex," *Journal of Chemical Education*, vol. 90, no. 12, pp. 1692–1696, 2013. [Online]. Available: https://doi.org/10.1021/ed400370p